PROPERTIES OF EVENTS CONTAINING A PHOTON AND SEVERAL JETS SEEN IN $\bar{p}p$ COLLISIONS AT $\sqrt{s} = 1.8$ TEV

by

PETER ALBERT MAAS

A thesis submitted in partial fulfillment of the

requirements for the degree of

DOCTOR OF PHILOSOPHY

(Physics)

at the

UNIVERSITY OF WISCONSIN - MADISON

1993

Abstract

The CDF detector is used to investigate the properties of events containing a photon and two jets. The rate of photon + 2 jet production is higher than the theoretical calculation, but the shape of the events agrees with QCD predictions.

Acknowledgements

I would like to the Lee Pondrom for his patience and his trust. I am appreciative of the knowledge he has passed on to me. Bob Blair taught me how to use the CDF detector to measure photons and I thank him for being my mentor. Thanks to Steve Kuhlmann for many useful discussions about using the detector to measure jets. I thank Aurore Savoy-Navarro for introducing me to the CDF detector.

I would also like to thank my friends on the CDF experiment. Colin Jessop, Steve Vejcik, Chris Boswell, and Bob Mattingly were all around during those late nights while the testbeam was running. Steve Hahn, whose twin I purport to be, taught me how how to keep RABBIT running. Melissa Franklin was extremely supportive of my work on the testbeam momentum measurement. Jaco Konigsberg kept the testbeam group organized and focussed.

I would also like to thank all my friends at the Charleston who have made my sojourn in Chicago enjoyable. Thanks Wendy and Scott for providing a top quality pool table. Thanks to everyone in the Sunday morning running group.

And yes Shari, I am a physicist.

I would like to thank my parents for their support, both emotional and financial which has enabled me to reach the end of this thesis. Thanks to Catherine's parents for their kindness. And lastly, thanks to Catherine for having the courage and the patience to endure my schedules, the willingness to not know where we were going to end up, and the patience to wait for me to finish.

This work was supported by the United States Department of Energy Contract DE-AC02-76ER00881.

Contents

List of Tables

List of Figures

Chapter 1

Introduction

In the seventeenth century, Newton explained the motion of the planets in terms of a mathematical model. He postulated an attractive force between two bodies proportional to the product of the masses, and inversely proportional to the square of the distance between them. This explained how the solar system is held together and the motion of the planets. It provided a means of calculating where celestial objects were expected to be.

Since that time, physicists have improved on our model of the world by explaining how other structures which we observe are held together in terms of forces. Since the invention of the microscope, our ability to observe has progressed from a rather limited distance scale ($\approx 10^{-6}m$) to a much smaller scale ($\approx 10^{-15}m$). Consequently, what was once considered to be an irreducible element has since come to be understood as a composite object.

As an example, consider our understanding of the once fundamental element, water. Chemistry led to the understanding of water as a molecule made up of two hydrogen atoms and one oxygen atom held together by the electric force. The hydrogen atom was then determined to be composed of smaller particles, an electron and a proton, also held together by the electric force. Experiments in the 1960s revealed the proton to be a composite object, made up of quarks and gluons held together by the strong force. Our current understanding of these fundamental constituents of matter and their interactions is contained in the Standard Model.

1.1 Particles in the Standard Model

Matter in the Standard Model is composed of fundamental particles which interact through force fields. All fundamental particles are fermions with spin $\frac{1}{2}$. Known particles come in two varieties, leptons which are colorless, and quarks which carry color. There are 6 leptons and 6 quarks which are thought to exist. These particles are listed, along with their properties in table 1.1. The masses of the leptons are unambiguous. The masses of the quarks are ambiguous in that the mass of an object composed of quarks is not the sum of the masses of the quarks. In table 1.1 the quark masses are the physical quark masses, not the masses determined from particles composed of quarks.

Quark	Charge	Mass (GeV/c^2)	Lepton	Charge	Mass (GeV/c^2)
up (u)	$+\frac{2}{3}$	0.005	e-neutrino (ν_e)	0	$< 1.8 \times 10^{-8}$
down (d)	$-\frac{1}{3}$	0.005	electron (e)	-1	5.11×10^{-4}
charm (c)	$+\frac{2}{3}$	1.5	μ-neutrino (ν_μ)	0	$< 2.5 \times 10^{-4}$
strange (s)	$-\frac{1}{3}$	0.150	muon (μ)	-1	0.106
top (t)	$+\frac{2}{3}$	> 92	τ-neutrino (ν_τ)	0	$< 7 \times 10^{-2}$
bottom (b)	$-\frac{1}{3}$	4.5	tau (τ)	-1	1.78

Table 1.1: The fundamental particles of the Standard Model

1.2 Interactions in the Standard Model

Interactions are the transfer of quanta between particles. The picture one has is of a quantum being emitted by one particle and absorbed by another. The transferred quanta are carried by bosons (particles of integral spin). Thus the four interactions: gravity, electromagnetism, the weak interaction, and the strong interaction are transmitted respectively by: the graviton, the photon, the W and Z bosons, and the gluon. Gravity, as stated earlier, describes the interaction of two masses. Electromagnetism describes the interaction of charged particles. The weak force couples to all fermions. The strong force describes the interaction of color. The strength of the interaction is described by the coupling of the gauge boson to the interacting particles. The properties of the gauge bosons are summarized in table 1.2.

Interaction	Gauge Boson	Mass	Charge	Spin
Gravity	Graviton	0	0	2
Electromagnetic	Photon (γ)	0	0	1
Weak	W	80.0	± 1	1
	Z_0	91.1	0	1
Strong	gluon (g)	0	0	1

Table 1.2: Properties of the gauge bosons

1.2.1 The Strength of an Interaction

The strength of the electromagnetic force is denoted by the coupling constant α. However the following problem arises. To calculate a cross section, the matrix element is expanded in orders of α. Leading order calculations keep only terms proportional to α^2. Naive calculations to higher order in α diverge. The divergences vanish if the following assumption is made: that the bare charge (that is the charge of a particle at the surface of the particle) is infinite. This infinite charge induces a cloud of virtual photons and virtual electron-positron pairs which act to reduce the charge actually observed in the physical world. Calculating the effect gives the following expression for α:

$$\alpha(Q^2) = \frac{\alpha(m^2)}{[1 - (\frac{\alpha(m^2)}{3\pi})\log(\frac{Q^2}{m^2})]} \tag{1.1}$$

$$\alpha(m^2) = \frac{1}{137} \text{ at } m = m_e = 0.51\text{Mev}/c^2 \tag{1.2}$$

This expression relates the strength at a small distance to the strength at large distances. Note that α barely changes over the range of Q^2 which is probed at the moment.

This process of absorbing divergences through a redefinition of the charge is known as renormalization. To quote Aitchison and Hey[1], "a renormalisable theory is one which is insensitive to ignorance about its behavior at very short distances."

In general, coupling constants are given as a function of the momentum transfer. Note that large momentum transfer implies a probe of small distance. Similarly, large momentum transfer implies a small time scale. Long time scales and large distance scales imply small values of Q^2.

1.3 The Strong Interaction

Experiments in the 1950s and 1960s led to the understanding that protons and neutrons were composite objects. However the structure of the composition was rather vague until a new quantity color was proposed. This quantity explains how three fermions could form states like the $\Delta^{++} = (uuu)$ and $\Omega^- = (sss)$. This view led to the theoretical description know as Quantum Chromodynamics (QCD). The coupling constant of QCD is represented by the symbol, α_s.

QCD is also renormalizable[2, 3]. The coupling strength, α_s, is expressed as

a function of the coupling strength at some momentum scale, μ^2, as:

$$\alpha_s(Q^2) = \frac{\alpha_s(\mu^2)}{1 + \frac{\alpha_s(\mu^2)}{12\pi}(33 - 2n_f)\log\frac{Q^2}{\mu^2}} \tag{1.3}$$

This expression is similar to equation 1.1 with the exception that the correction term is positive for $n_f < 16$ where n_f is the number of quark flavors ($n_f = 5$). This means that the strength of the strong interaction decreases with increasing momentum transfer. At large distance scales and/or long time scales, α_s is large, and quarks and gluons are said to be confined. As one goes to smaller distance scales and shorter time scales, the value of α_s decreases. Quarks and gluons appear less confined, and perturbative calculations apply. This property is known as asymptotic freedom. QCD is different from QED in that we are ignorant about the behavior of quarks and gluons at large distance scales and long time scales.

It is customary to define Λ by

$$\log\Lambda^2 = \log\mu^2 - \frac{12\pi}{(33 - 2n_f)\alpha_s(\mu^2)} \tag{1.4}$$

Equation 1.3 becomes

$$\alpha_s(Q^2) = \frac{12\pi}{(33 - 2n_f)\log(\frac{Q^2}{\Lambda^2})} \tag{1.5}$$

The information of the scale at which α_s is determined is contained in the value of $\Lambda(= 0.125$ GeV). The value of Λ depends on the number of flavors accessible at the scale μ^2. Here the value of Λ is given for $\mu > m_b = 5$GeV. Figure 1.1 shows the value of α_s as a function of Q.

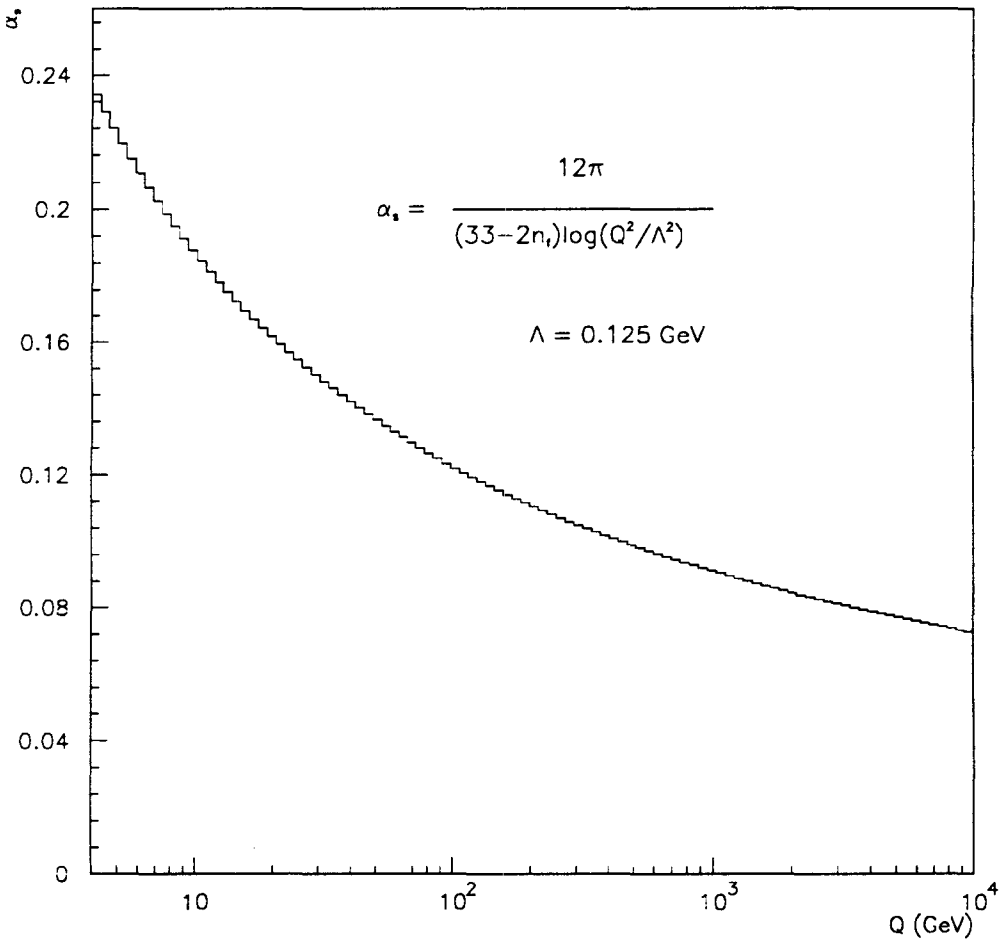

Figure 1.1: α_s plotted as a function of Q. Note that α_s is changing rather rapidly in the range 10 to 100 GeV.

1.3.1 Proton–Anti-proton interactions as a probe of QCD

High energy proton–anti-proton collisions provide a good enviroment to test QCD. First, if the proton and anti-proton have equal, but opposite momentum, the final state particles will be symmetric in the laboratory and the available center of mass energy will be twice the energy of the proton. Secondly, the amount of energy measured transverse to the beam implies a momentum transfer of at least that order. If this energy is much greater than Λ, α_s is small and perturbative calculations are reliable.

Photon production in proton–anti-proton collisions is useful because it isolates particular constituents of the proton and anti-proton. Large momentum transfer implies that the constituents of both the proton and anti-proton are free. The picture one has is of a proton being composed of one component which interacts, and numerous components which carry the remainder of the proton's momentum (spectators). These components are called partons. QCD Compton scattering is when a quark absorbs a gluon and emits a photon. Figure 1.2 illustrates the model of proton–anti-proton interactions. The Feynman diagram for this process is shown in figure 1.3. On a longer time scale, the scattered partons will induce the creation of quark–antiquark pairs from the vacuum so as to confine all quarks in colorless hadron states. This process is called fragmentation and results in a stream of particles (jet) traveling in the same direction as the parent parton (see figure 1.2). The photon, being colorless, does not fragment.

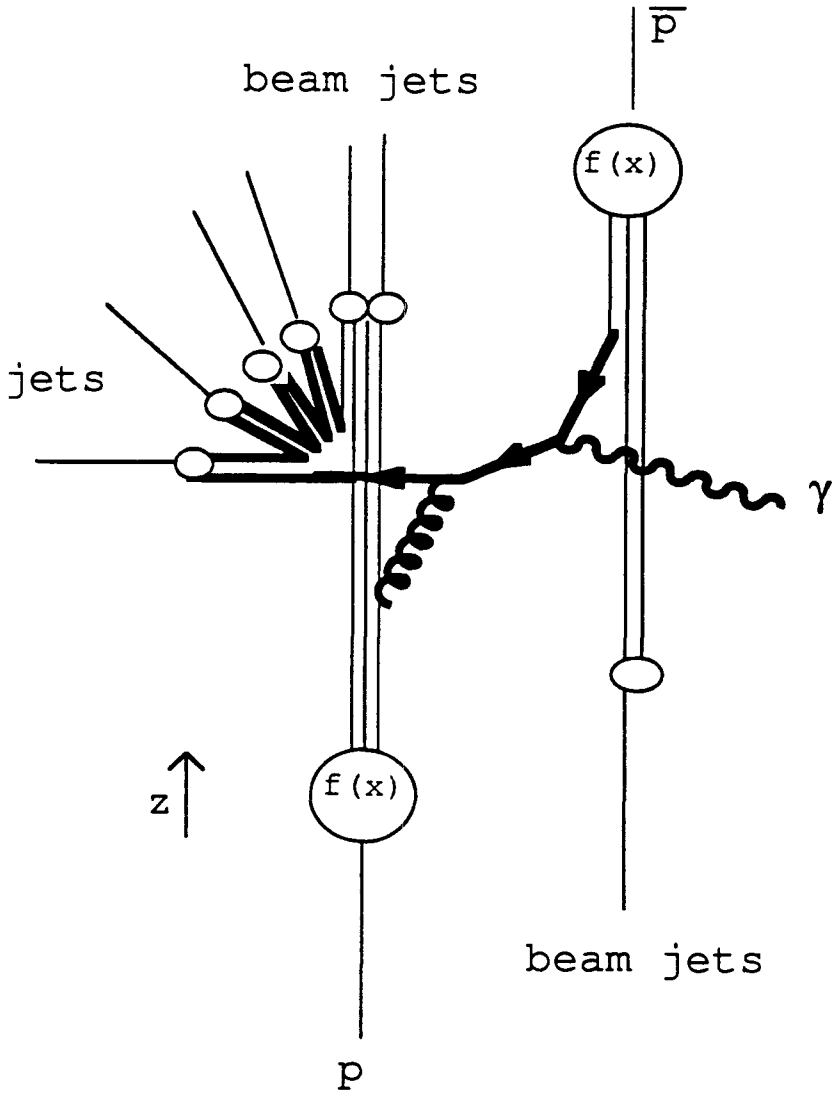

Figure 1.2: Illustration of the parton model for QCD Compton scattering in $\bar{p}p$ collisions. The functions, f, are the parton distribution functions which will be described later. The bold lines denote the hard interaction. Circles denote hadronic final states.

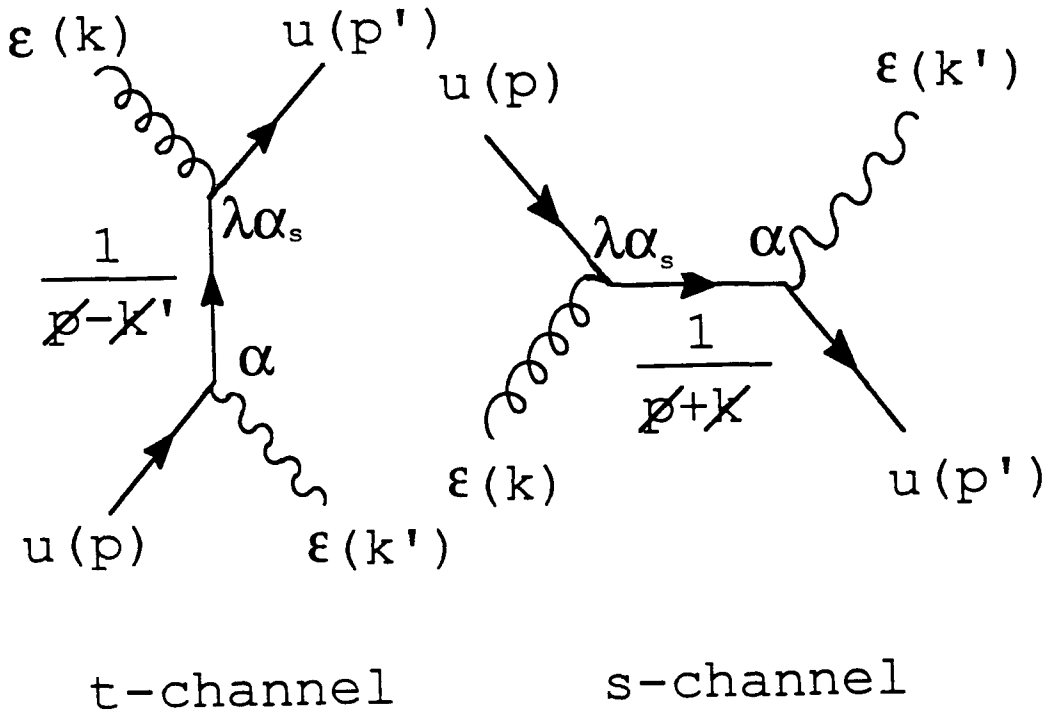

Figure 1.3: Leading order Feynman diagrams for QCD Compton scattering. The first diagram illustrates the assignment of factors which give the matrix element.

The other leading order process is quark–antiquark annihilation. The diagram for this process involves exchanging the incoming gluon and the outgoing quark in the first diagram. However because gluons are more plentiful in protons than quarks, QCD Compton scattering should dominate photon production processes.

The AFS experiment at the CERN ISR used these facts to extract the gluon distribution in the proton[4]. The experiment measured the rate of photon + jet production in proton-proton collisions at $\sqrt{s} = 63$ GeV where both the jet and the photon were at 90° to the beam axis. Because of this condition, the cross section can be expressed as

$$\left.\frac{d^3\sigma}{dp_T^\gamma d\eta^\gamma d\eta^{\rm jet}}\right|_{\eta^\gamma=\eta^{jet}=0} = \frac{5}{3} K \alpha \alpha_s \frac{1}{x^2} \frac{1}{s^{3/2}} G(x) F_2(x) \tag{1.6}$$

where $x = \frac{2p_T}{\sqrt{s}}$. K is a factor introduced to correct for the non-inclusion of higher order processes in the calculation. The AFS experiment used $K = 2.7$ to account for the contribution of photon events where the photon is due to Bremsstrahlung from a final state quark.

More recently the UA2 experiment at the CERN $S\bar{p}pS$ Collider extracted the gluon distribution from isolated single photon production [5]. The UA2 analysis made use of a next-to-leading logarithm QCD calculation and then expressed the cross section for photon + jet production as a sum of terms where each term isolates a different initial state. Their analysis required no second jet with $E_T > 6$ GeV to remove the contribution from Bremsstrahlung. In the UA2 analysis, there is no K-factor because the higher order contributions to the $2 \rightarrow 2$ process are

included.

The CDF experiment at Fermilab has started a similar analysis. The first step has been the measurement of the inclusive cross-section for the production of an isolated single photon as a function of p_T. The measured cross sections from both UA2 and CDF are shown in figure 1.4[6, 7]. In both cases, the measured cross sections are compared to a next-to-leading logarithm QCD calculation.

In all three cases, there is good agreement between theory and experiment. However none of these experiments has checked the accuracy of the higher order calculation beyond the measurement of the cross section. Figure 1.5 shows that the higher order corrections represent 50% of the calculated cross section. To check the validity of the higher order calculations requires an investigation of the $2 \rightarrow 3$ processes which give a photon in the final state.

This analysis is an attempt to verify the hypothesis that QCD processes explain photon + 2 jet production at CDF. It begins with an overview of the theoretical calculation of photon + 2 jet production. It continues with a description of how the CDF experiment measured direct photon production. The experimental results are compared to phenomenological expectations with the result that the topology of the events is explained by QCD calculations, but the rate of photon + 2 jet production is not.

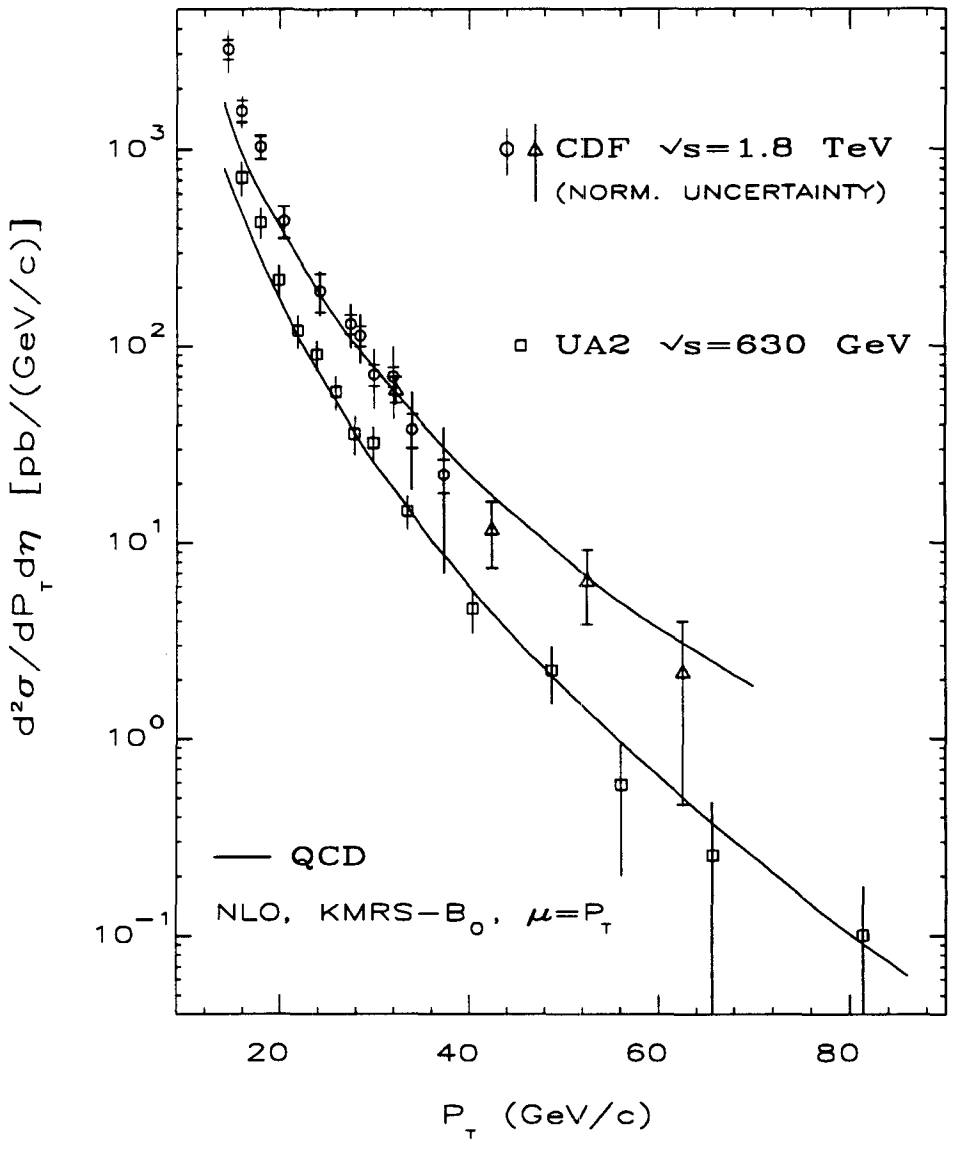

Figure 1.4: The inclusive isolated single photon cross section as measured by both CDF and UA2 compared to the next-to-leading logarithm QCD calculation.

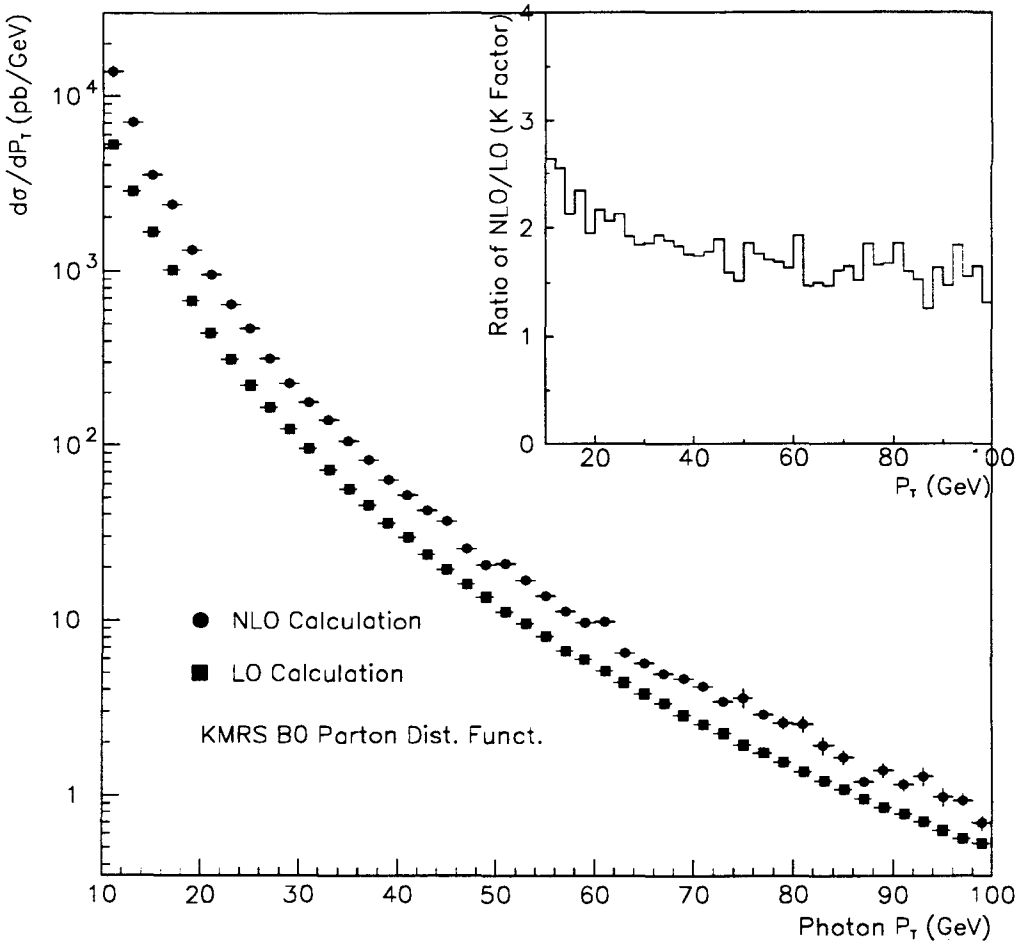

Figure 1.5: Comparison of the next-to-leading logarithm and leading logarithm calculation of inclusive single photon production. The photon is required to have $40° < \theta < 140°$.

Chapter 2

Calculation of Photon Production in Proton–Anti-Proton Collisions

In the parton model, the differential cross section for a $2 \rightarrow 3$ process giving a photon and two jets in the final state may be written

$$d\sigma = \sum_{a,b} \int_0^1 dx_a \int_0^1 dx_b \, f_{a/p}(x_a) \, f_{b/\bar{p}}(x_b) \\ |\mathcal{M}^2| \, \delta^4(p_a + p_b - p_\gamma - p_d - p_e) \frac{d^3p_\gamma}{2E_\gamma} \frac{d^3p_d}{2E_d} \frac{d^3p_e}{2E_e} \tag{2.1}$$

where the sum over a and b is over all initial state partons which lead to the final state γ,d, and e. The functions, $f_{y/Y}(x)$, are the parton distribution functions

which give the probability of finding a parton of type, y, in hadron Y carrying a fraction, x, of the hadron's momentum. These functions cannot be calculated. However particular combinations are measured in deep inelastic lepton scattering experiments. The gluon distribution is not directly measured. It is constrained by measurements of photon production and measurements of lepton pair production (Drell Yan). Higher order corrections to deep inelastic lepton scattering are also sensitive to the gluon distribution. The normalization is constrained by the fact that the sum over the momenta of all partons in the proton must give the proton momentum. The product of the parton distribution functions can be thought of as the parton-parton luminosity. This analysis uses the CTEQ1L parton distribution functions determined by the CTEQ collaboration[8]. The parameterized version of the distribution functions are given in Appendix A[9]. Figure 2.1 shows the total parton-parton luminosity summed over all types of partons. Figure 2.2 shows the fraction of the parton-parton luminosity generated by quark-quark initial states, gluon-gluon initial states and gluon-quark initial states. Note that quark-gluon initial states dominate.

$|\mathcal{M}^2|$ is the matrix element which describes the dynamics of the reaction $ab \rightarrow \gamma de$. It is calculated by summing all relevant Feynman diagrams. It depends on x_a, x_b, and the momenta and energies of the final state particles. Some of the included diagrams are shown in figure 2.3.

Because this is a leading order calculation the choice of the μ^2 scale is not obvious. In all calculations the scale is taken to be the transverse momentum of

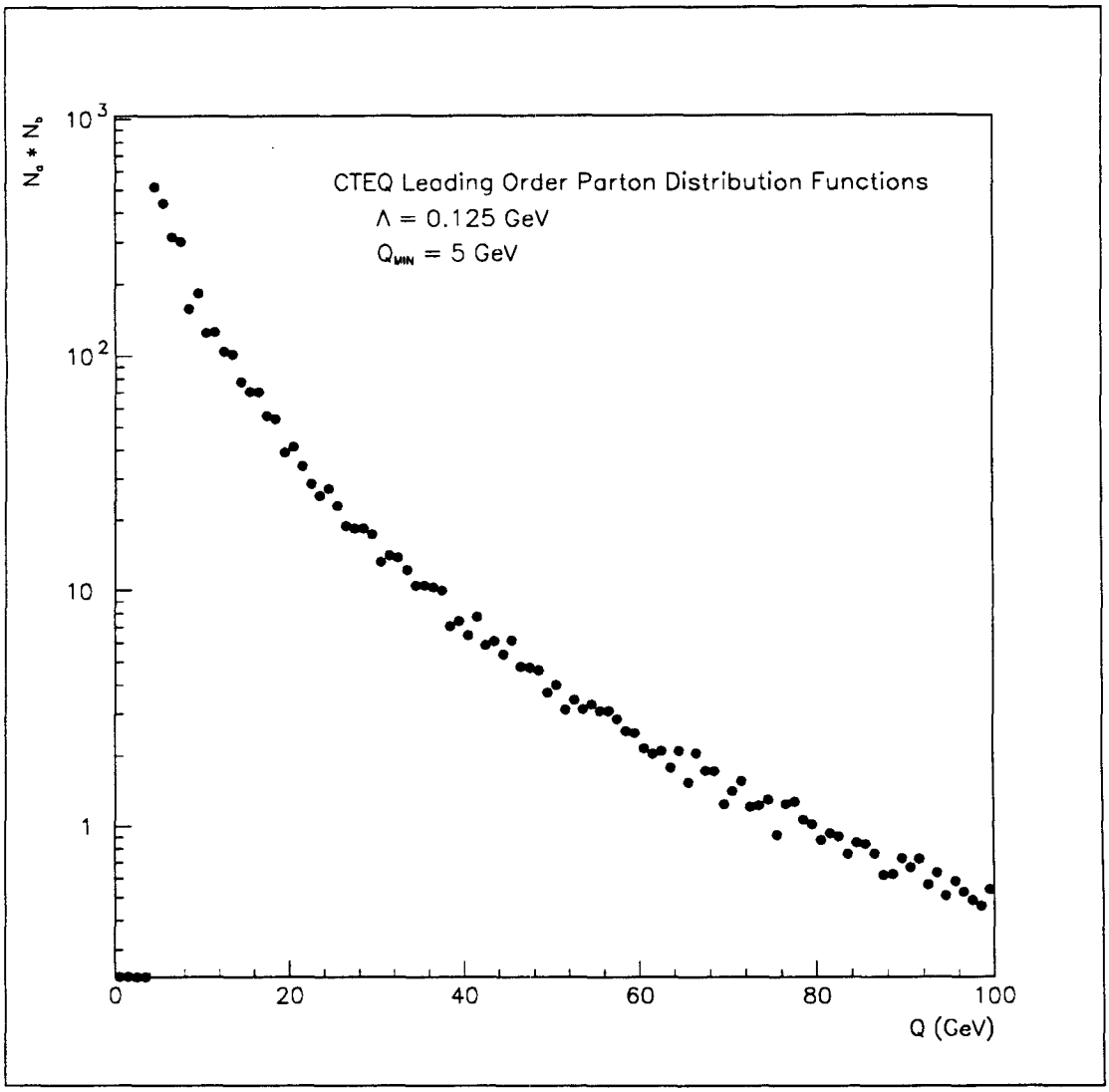

Figure 2.1: The parton-parton luminosity plotted as a function of the momentum transfer, Q. $N_a(N_b)$ refer to the number of partons present in the proton (anti-proton).

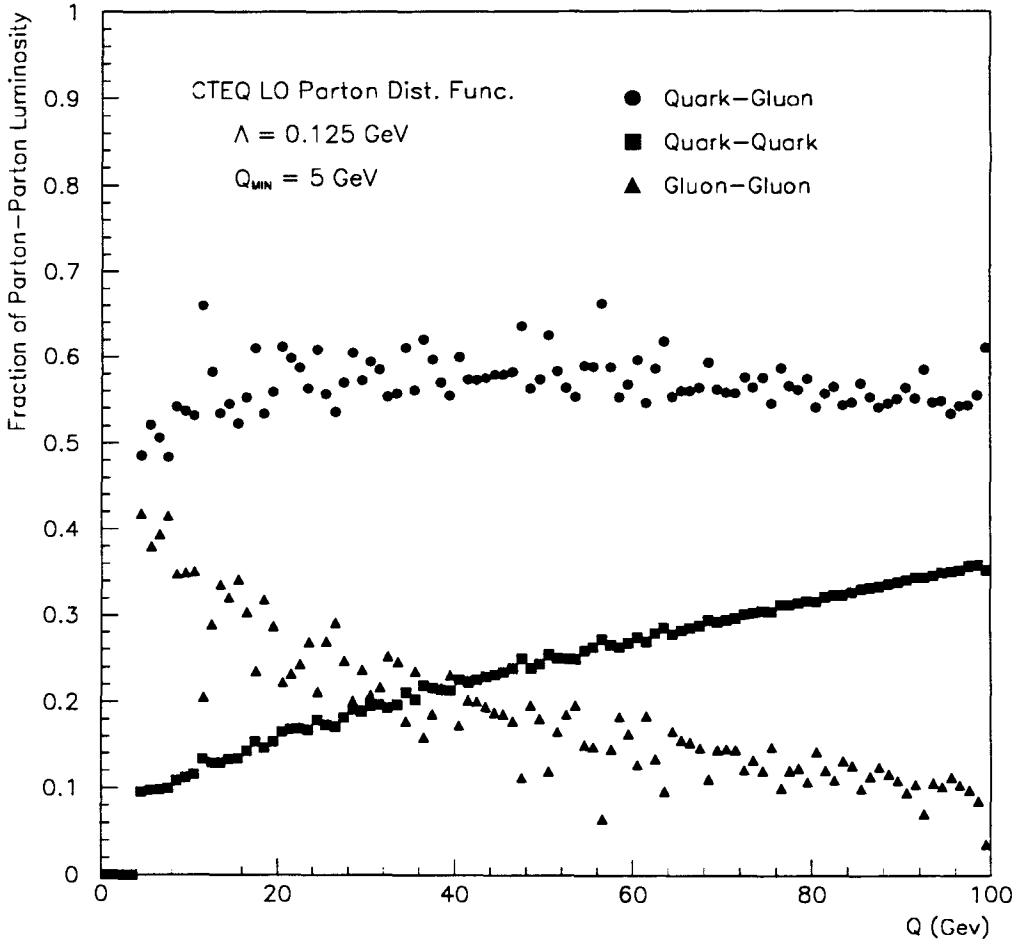

Figure 2.2: The fraction of the parton-parton luminosity due to different parton initial states summed over all parton initial states plotted as a function of Q.

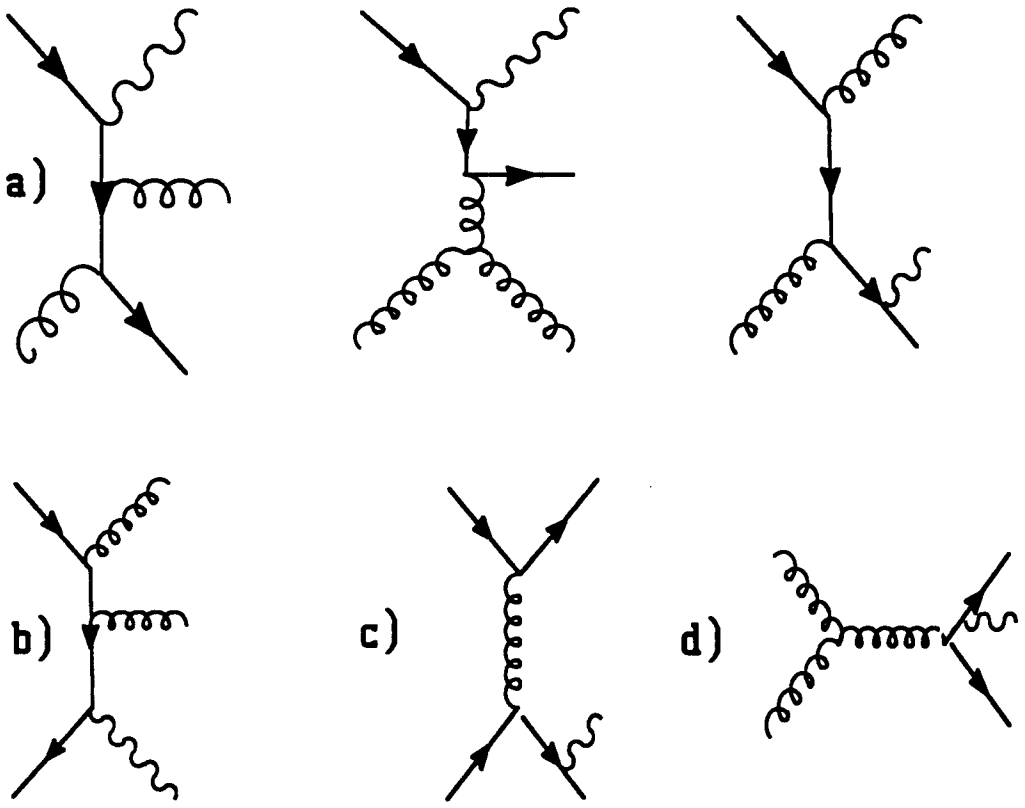

Figure 2.3: Higher order diagrams for photon production. Diagrams labeled (a) show corrections to the QCD Compton process. (b) shows an example of $q\bar{q}$ annihilation, (c) shows a typical qq contribution with a radiated photon, and (d) is one of the gg diagrams which contributes. There are $\approx$ 30 diagrams which need to be calculated.

the photon. However this introduces an uncertainty. Consider the case of internal Bremsstrahlung. The photon p_T is less than the momentum transfer in the $2 \rightarrow 2$ process which gives the quark and another parton in the final state. The opposite case is when a gluon is radiated from an initial or final state parton. However choosing the μ^2 scale to be the photon p_T^2 averages over these two cases. Varying the μ^2 scale between $\frac{p_T^2}{4}$ and $4p_T^2$ gives a 40% variation on the cross section.

The function, $\delta^4()$ is the Dirac delta function and guarantees conservation of momentum and energy. Integrating over the delta function removes 4 degrees of freedom which leaves the following expression:

$$d\sigma = \sum_{a,b} \int_0^1 dx_a \int_0^1 dx_b \, f_{a/p}(x_a) \, f_{b/\bar{p}}(x_b) |\mathcal{M}^2| \\ p_\gamma dp_\gamma d\phi_\gamma d\cos\theta_\gamma d\phi_d d\cos\theta_d \tag{2.2}$$

The matrix elements for the process

$$ab \rightarrow \gamma + c + d \tag{2.3}$$

were calculated by Aurenche et al. [10].

The matrix elements are expressed in terms of various combinations of the incoming and outgoing momentum. Define

$$T_{ij} = (E_i - E_j)^2 - (\vec{p}_i - \vec{p}_j)^2 \tag{2.4}$$

$$S_{ij} = (E_i + E_j)^2 - (\vec{p}_i + \vec{p}_j)^2 \tag{2.5}$$

where E is the energy, $\vec{p}$ is the momentum, and indices i and j refer to the interacting partons. Then the matrix elements are given by:

$$
\begin{aligned}
&|\mathcal{M}^2|(qq' \to \gamma qq') = \\
&\quad \frac{4\pi^3}{9}\alpha_s^2\alpha \\
&\quad \frac{S_{ab}^2 + T_{bd}^2 + T_{ae}^2 + S_{ae}^2}{T_{be}T_{ad}} \\
&\quad \left[e_q e_{q'} \left(-\frac{S_{ab}}{T_{a\gamma}T_{b\gamma}} + \frac{T_{bd}}{T_{b\gamma}S_{\gamma d}} + \frac{T_{ae}}{T_{a\gamma}S_{\gamma e}} - \frac{S_{de}}{S_{\gamma d}S_{\gamma e}} \right) + \right. \\
&\quad \left. e_q^2 \frac{T_{ad}}{T_{a\gamma}S_{\gamma d}} + e_{q'}^2 \frac{T_{be}}{T_{b\gamma}S_{\gamma e}} \right]
\end{aligned}
\tag{2.6}
$$

$$
\begin{aligned}
&|\mathcal{M}^2|(gq \to \gamma qg) = \\
&\quad \frac{\pi^3}{2}\alpha_s^2\alpha e_q^2 \\
&\quad \left(\frac{1}{9}T_{bd} - \frac{T_{ad}T_{be} - S_{ab}S_{de}}{T_{ae}} \right) \\
&\quad \left[\frac{S_{\gamma d}^2 + T_{b\gamma}^2}{T_{ad}S_{de}S_{ab}T_{be}} + \frac{T_{ad}^2 + S_{ab}^2}{S_{\gamma d}S_{de}T_{b\gamma}T_{be}} + \frac{S_{de}^2 + T_{be}^2}{S_{\gamma d}T_{ad}T_{be}S_{ab}} \right]
\end{aligned}
\tag{2.7}
$$

$$
\begin{aligned}
&|\mathcal{M}^2|(qq \to \gamma qq) = \\
&\quad \frac{2\pi^3}{9}\alpha_s^2\alpha e_q^2 \\
&\quad \left(-\frac{S_{ab}}{T_{a\gamma}T_{b\gamma}} + \frac{T_{bd}}{T_{b\gamma}S_{\gamma d}} + \frac{T_{be}}{T_{b\gamma}S_{\gamma e}} + \frac{T_{ae}}{T_{a\gamma}S_{\gamma e}} - \frac{S_{de}}{T_{\gamma e}T_{\gamma d}} + \frac{T_{ad}}{T_{a\gamma}S_{\gamma d}} \right) \\
&\quad \left[\frac{S_{ab}^2 + T_{bd}^2 + T_{ae}^2 + S_{de}^2}{T_{ad}T_{be}} + \frac{S_{ab}^2 + T_{ad}^2 + T_{be}^2 + S_{de}^2}{T_{bd}T_{ae}} - \right. \\
&\quad \left. \frac{1}{3}\left(S_{ab}^2 + S_{de}^2\right) \frac{S_{ab}S_{de} - T_{bd}T_{ae} - T_{be}T_{ad}}{T_{be}T_{be}T_{ad}T_{ae}} \right]
\end{aligned}
\tag{2.8}
$$

The above matrix elements suffice to calculate all $2 \rightarrow 3$ contributions to the photon + 2 jet final state. However care must be taken when summing over quarks and antiquarks.

Assuming massless partons, relations 2.4 and 2.5 reduce to

$$T_{aj} = -2E_a E_j(1 - \cos\theta_j) \tag{2.9}$$

$$T_{bj} = -2E_a E_j(1 + \cos\theta_j) \tag{2.10}$$

$$S_{ab} = S_{\gamma d} + S_{\gamma e} + S_{de} = E^2_{\rm COM} = x_a x_b s \tag{2.11}$$

where θ_j is the angle between the direction of parton, j, and the incoming proton and $\sqrt{s}$ is the center-of-mass energy of the colliding proton and anti-proton. The kinematics of the reaction are completely described by:

$$S_{ab}, T_{a\gamma}, T_{ad}, T_{ae}, T_{b\gamma}, T_{bd}, T_{be}, S_{\gamma d}, S_{\gamma e}, S_{de} \tag{2.12}$$

The incoming partons are assumed to have no momentum transverse to the beam. In the lab frame, the total momentum is given by

$$\vec{P}_{\rm LAB} = (x_a - x_b)\frac{\sqrt{s}}{2}\hat{z} \tag{2.13}$$

defining the direction of the protons as the $+z$ direction. The transformation from the center-of-mass to the lab is defined by the incoming parton momentum fractions.

The cross section is obtained using a Monte Carlo integration technique [11]. The integration is over 7 variables: the incoming parton momentum fractions, the momentum and direction of the photon, and the direction of one of the final

state partons (each direction is specified by two angles). A particular element of this space is chosen at random. The contribution for each combination of partons a and b is calculated by multiplying the parton luminosity factor and the squared matrix element. The cross section for this element is the sum over all possible combinations of a,b,d, and e. This is repeated a large number of times (typically 10^7) to guarantee that the space is uniformly sampled. The differential cross-section with respect to any particular variable is calculated by binning the cross section with respect to that particular variable.

A second calculation similar to the first is performed with the exception that the angular factors due to the matrix elements are not included. This is an integration over the available three body phase space. A diagram of the phase space is given in figure 2.4. A soft jet or photon has nearly zero energy. A collinear pair is a pair of particles which have a very small opening angle. The Mercedes Benz configuration is when the photon and the jets have equal energies, and the angle between any pair is 120°. If the matrix element was 1, the shaded region in figure 2.4 would be uniformly populated. As can be seen in figure 2.5, the matrix elements become large when the second jet becomes collinear with either the photon or the leading jet. The purpose of the phase space calculation will be to verify that the properties of the measured events are not due to biases in the selection procedure.

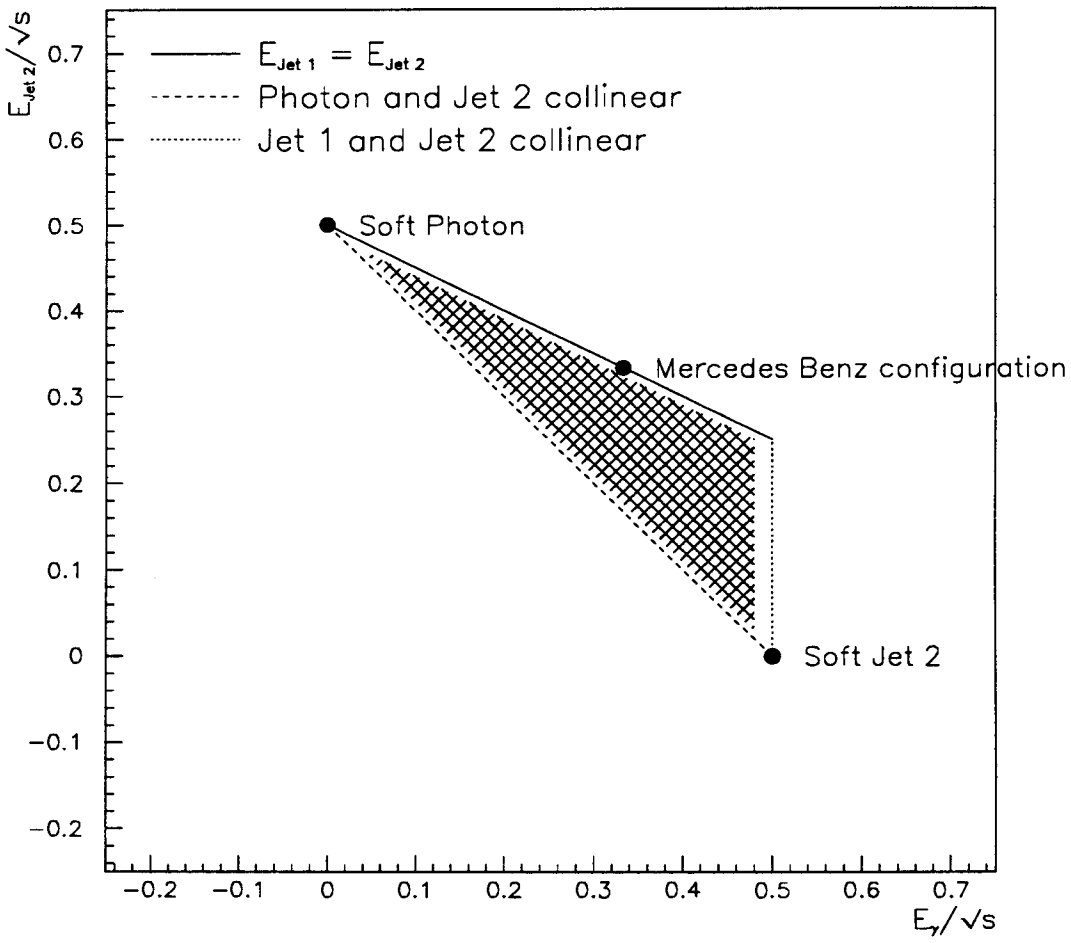

Figure 2.4: Schematic diagram of the available phase space.

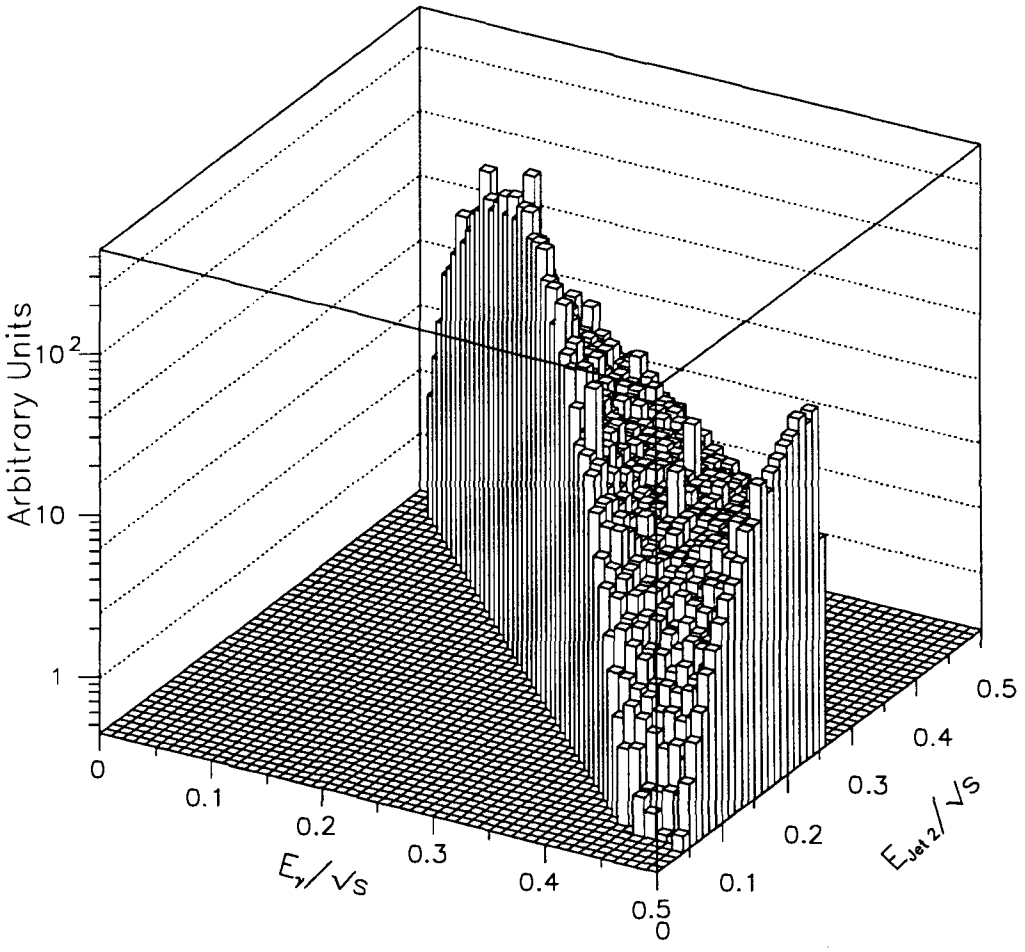

Figure 2.5: Illustration that the matrix elements diverge when the second jet is collinear with either the photon or the leading jet. The soft divergences do not appear because of E_T requirements on the photon and the two jets.

Chapter 3

Experimental Apparatus

3.1 The Tevatron

The Tevatron at Fermilab produces proton–anti-proton collisions with a center of mass energy of 1.8 TeV. The procedure for making and accelerating protons and anti-protons has been described in great detail elsewhere [12, 13, 14, 15]. The parameters of the accelerator relevant to this analysis are those factors related to the luminosity and the size of the luminous region at the collision point.

The luminosity is defined by

$$\mathcal{L} = \frac{N_p N_{\bar{p}} f}{4\pi \sigma_x \sigma_y} \tag{3.1}$$

where $N_p(N_{\bar{p}})$ are the number of protons (anti-protons) in each bunch. f is the crossing frequency. $\sigma_x(\sigma_y)$ describe the width of the beam along the horizontal (vertical) axis in the plane transverse to the beam. For the data collected in the

period of September, 1988 through June, 1989 typical values were:

- $N_p = 7 \times 10^{10}$
- $N_{\bar{p}} = 3 \times 10^{10}$
- $f = 286$ kHz
- $\sigma_x = \sigma_y = 60\mu$m

These values give a luminosity of 1.3×10^{30} cm^2 s^{-1}.

The luminous region at the interaction point is well described by a gaussian distribution of width 32 cm.

3.2 The CDF Detector

The CDF detector is a general purpose detector which measures the energy flow and the particle content in events resulting from $p\bar{p}$ collisions. A schematic of the detector is shown in figure 3.1.

The center of the coordinate system is at the geometric center of the detector. The $+z$ axis is aligned with the direction of the incident protons. The $+y$ axis points up, and the x axis lies in the horizontal plane. However more use is made of the pseudorapidity, η, and azimuthal angle, ϕ, defined by:

$$\eta = -\frac{1}{2}\log\frac{E - p_z}{E + p_z} \tag{3.2}$$

$$\phi = \arctan\frac{y}{x} \tag{3.3}$$

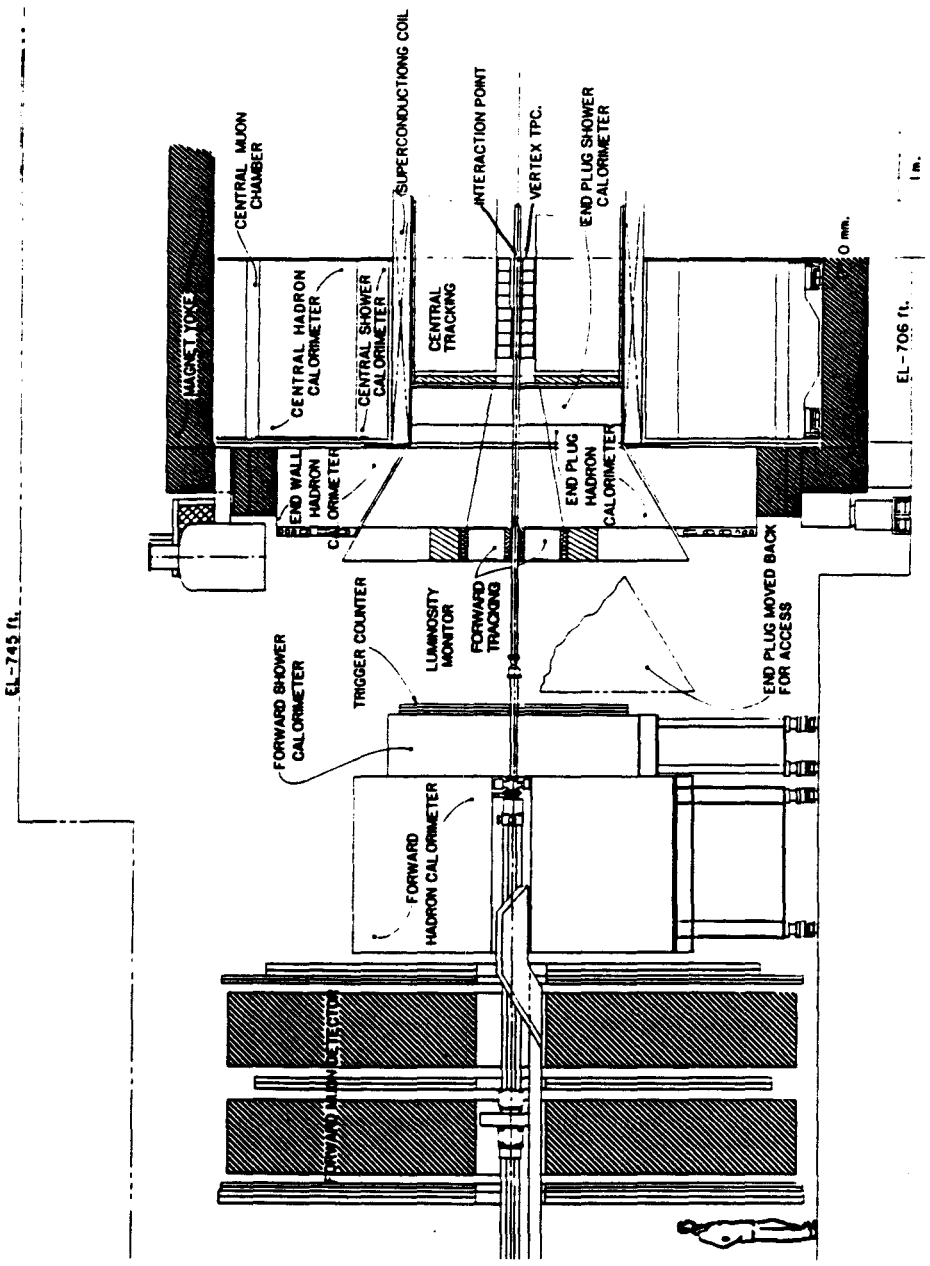

Figure 3.1: Cut-away view of the CDF detector showing the location of various elements. The detector is symmetric about the interaction point.

Note that η is related to the angle with respect to the z axis (θ) through the following relations:

$$\sin\theta = \frac{1}{\cosh\eta} \tag{3.4}$$

$$\cos\theta = \tanh\eta \tag{3.5}$$

$$\eta = -\log\tan\frac{\theta}{2} \tag{3.6}$$

The detector is composed of tracking detectors, calorimeters, and muon detectors. Tracking detectors are used to reconstruct the path of charged particles. The CDF tracking detectors are contained in a magnetic field so as to measure the momentum of particles through the relation

$$p_\perp = 0.3BR \tag{3.7}$$

where $p_\perp$ is the momentum perpendicular to the magnetic field direction in GeV, B is the magnetic field strength (= 1.4116 Tesla), and R is the radius of curvature of the path in the plane transverse to the magnetic field in meters. The magnetic field is aligned along the z axis, so the path of a charged particle is a circle in the $r-\phi$ plane and a helix in the $r-z$ plane. The calorimeters are sampling calorimeters. They consist of layers of dense absorber with a detecting medium sandwiched between each layer. The purpose of the absorber is to cause the particles to radiate energy in the form of more particles (or as the process is more commonly known, shower). The total absorber thickness is chosen so that showers are fully contained in the calorimeter. The energy of particles is then proportional

to the total number of charged particles traversing each layer. Hadronic particles are separated from electromagnetic particles by segmenting the calorimeter in depth and using lead (steel) absorber in the electromagnetic (hadronic) segment. The general form of the energy resolution is given by

$$\frac{\sigma}{E} = \frac{R}{\sqrt{E}} \oplus C \tag{3.8}$$

where

$$a \oplus b = \sqrt{a^2 + b^2} \tag{3.9}$$

R depends on sampling thickness and the absorber thickness and C is due to the uniformity of the calorimeter and other factors. Muon detectors detect particles which exit the calorimeter. In general, muons interact minimally in even the densest material. Thus any particle which exits the calorimeter with almost no energy deposition is considered a muon.

3.2.1 The CDF Tracking System

The CDF Tracking system consists of two detectors. The vertex time projection chamber surrounds the beam pipe. It is used to reconstruct the z vertex of the collision. The central tracking chamber surrounds the vertex time projection chamber. It extends to a radius 1.38 m.

3.2.1.1 The Vertex Time Projection Chamber (VTPC)

The mechanical structure of the VTPC is described in full detail elsewhere[16]. It measures the $r - z$ location of a charged particle's trajectory. The detector consists of eight octagonal chambers (shown in figure 3.2). Each chamber consists of a volume of gas with an electric field aligned along the z axis. At each end of the chamber is a wire plane. The location of the wire determines the r location, the travel time of the electrons liberated in the gas due to a charged particle determine the z location. Reconstructed lines in the $r - z$ plane determine the z vertex of the collision with an accuracy of 1 mm.

3.2.1.2 The Central Tracking Chamber (CTC)

The CTC [17] is used to reconstruct the full 3-dimensional path of charged particles with $|\eta| < 1.1$. It consists of 84 layers of wires organized in 9 superlayers. Five of the superlayers consist of wires strung parallel to the z axis. Each of these axial layers consist of 12 sense wires. The geometry of an axial superlayer is given in figure 3.3. The ϕ location is determined by the drift time; the r location is determined from the wire. Between each pair of axial superlayers is a superlayer consisting of six wires alternating at an angle of $\pm 3^0$ with respect to the z axis so as to measure the slope of the track in the $r - z$ plane.

The momentum resolution of the CTC is

$$\frac{\delta p_t}{p_t} = 0.0020 p_t \tag{3.10}$$

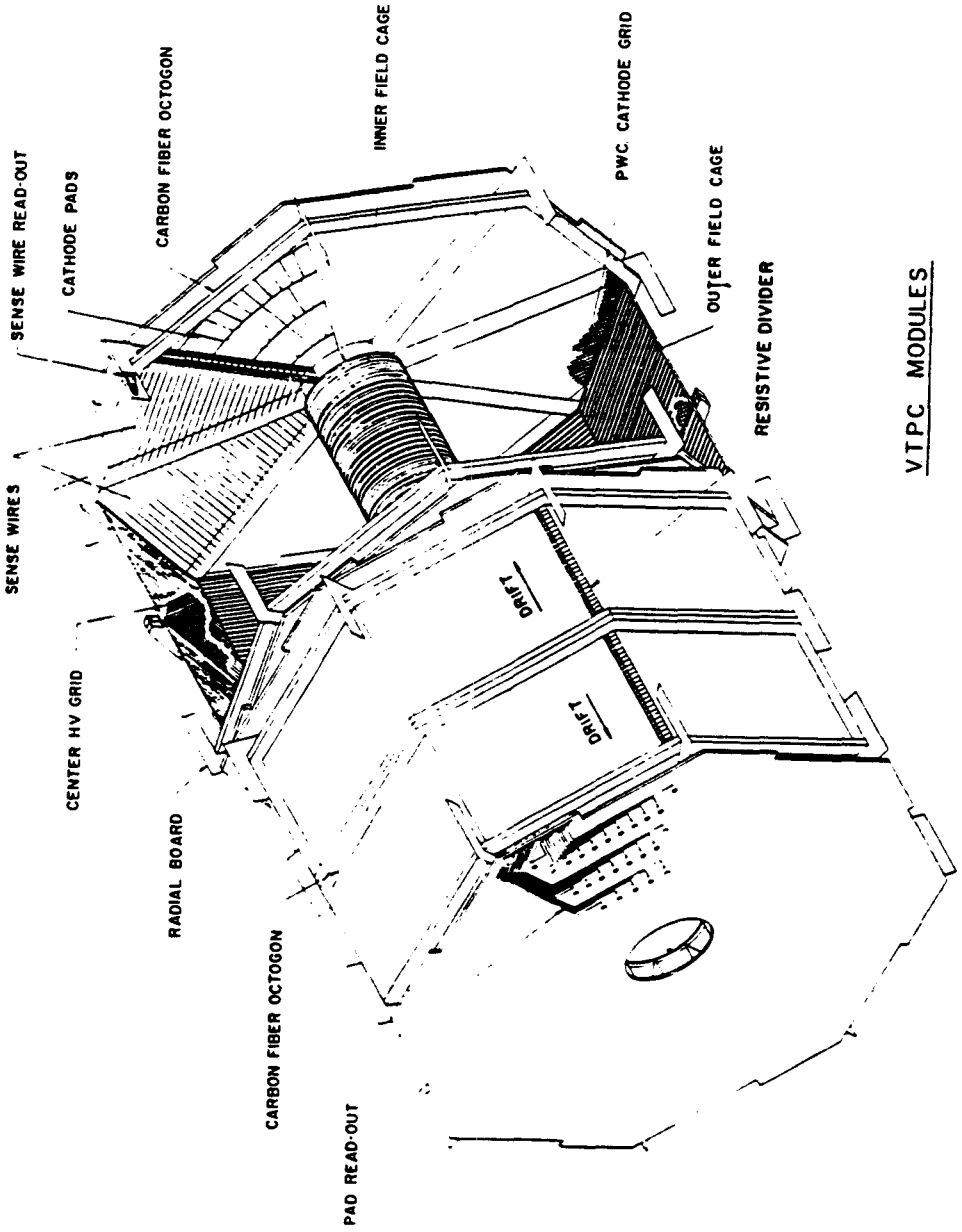

Figure 3.2: View of two chambers of the VTPC showing the geometry of the wires.

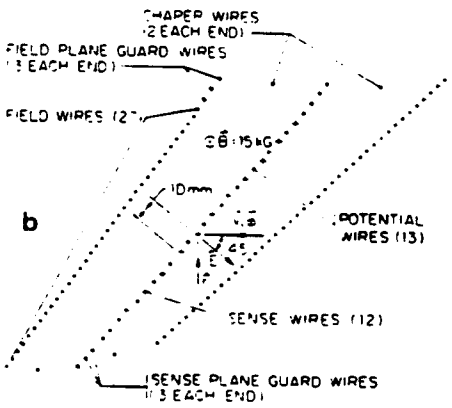

Figure 3.3: View of a axial drift cell in the CTC.

Constraining the particle to originate at the collision point, improves the resolution to

$$\frac{\delta p_t}{p_t} = 0.0011 p_t \tag{3.11}$$

The accuracy of equation 3.11 was checked by comparing the measured mass of both the J/ψ and the Υ using muon pairs to the world average obtained from the Particle Data Group [18](see figure 3.4). The results of the fit are given in table 3.1 [19]. The momentum scale is accurate to 0.1%.

3.2.2 Calorimetry

The CDF calorimeter is split into three pieces to facilitate construction and installation of the detector. The central and endwall calorimeter surround the

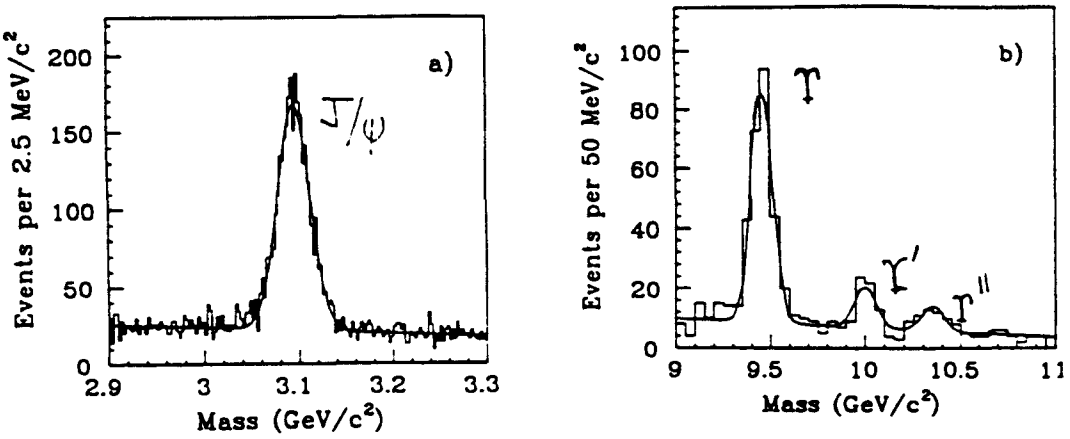

Figure 3.4: The invariant mass distribution of oppositely charged muon pairs showing the fit to the J/ψ mass (a) and the Υ mass (b). Also shown in (b) are the peaks due to the Υ' and the Υ".

Particle	Measured Mass	World Average
J/ψ	3.0963 ± 0.0005 GeV/c^2	3.0969 ± 0.0001 GeV/c^2
Υ	9.457 ± 0.005 GeV/c^2	9.4603 ± 0.0002 GeV/c^2

Table 3.1: Comparison of J/ψ and Υ masses measured by CDF to the world average.

CTC. The endplug calorimeter is located at both ends of the CTC in z. The forward calorimeters are separate structures which cover regions at small angles with respect to the beam axis.

The calorimeter is segmented into towers which project back onto the geometric center of the detector. The segmentation for each of the different pieces of the calorimeter is shown in figure 3.5.

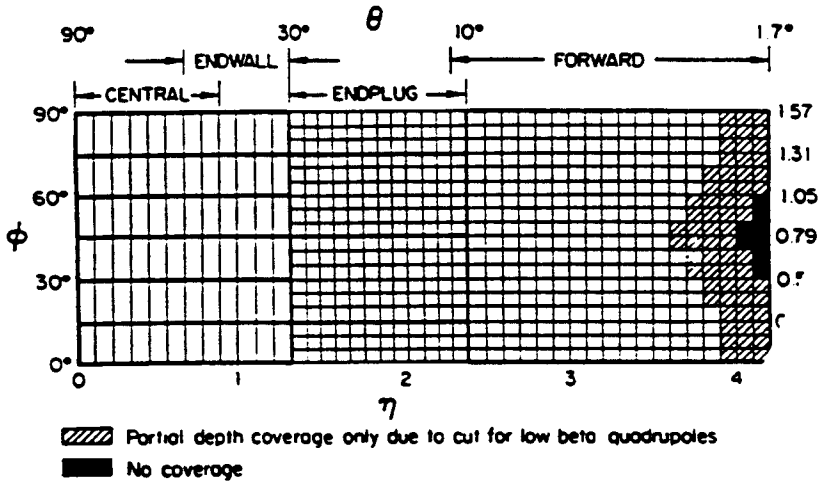

Figure 3.5: A schematic view of the angular coverage of each piece of the CDF calorimeter system. Also shown is the $\eta - \phi$ segmentation.

Tables 3.2 and 3.3 summarize the characteristics of the CDF calorimeters. The following text describes in more detail various pieces important for this study.

3.2.2.1 The Central Electromagnetic Calorimeter

The central electromagnetic calorimeter is comprised of 20-30 layers of lead and scintillator. The number of layers is varied to keep the total number of radiation

	CEM	CHA	WHA
$\eta - \phi$ seg	$0.1 \times 15°$	$0.1 \times 15°$	$0.1 \times 15°$
# of layers	31	32	15
Sampling Mat.	Scint.	Scint.	Scint.
Sampling Thick.	0.5 cm	1.0 cm	1.0 cm
Absorber	Pb	Fe	Fe
Single Absorber Thickness	0.32 cm	2.5 cm	5.1 cm
Total Rad. Length	18.0	45.5	43.5
Total Abs. Length	0.89	4.7	4.5
Resolution defined by $\frac{\sigma}{E} = \sqrt{\frac{R^2}{E_T} + C^2}$			
R (% $\sqrt{\text{GeV}}$)	13	60	60
C (%)	1	5	5

Table 3.2: Characteristics of the CDF Central Calorimeters

	PEM	PHA	FEM	FHA
$\eta - \phi$ seg	$0.1 \times 5^{\circ}$	$0.1 \times 5^{\circ}$	$0.1 \times 5^{\circ}$	$0.1 \times 5^{\circ}$
# of layers	34	20	30	27
Sampling Mat	Ar-Eth	Ar-Eth	Ar-Eth	Ar-Eth
Sampling Thick.	0.7 cm	1.2 cm	0.7 cm	1.0 cm
Absorber	Pb	Fe	Pb	Fe
Single Absorber Thickness	0.27 cm	5.1 cm	0.48 cm	5.1 cm
Total Rad. Length	18.2	58.0	25.5	78.2
Total Abs. Length	0.88	6.0	1.23	8.1
Resolution defined by $\frac{\sigma}{E} = \sqrt{\frac{R^2}{E_T} + C^2}$				
R	25	100	25	100
C	2	5	2	5

Table 3.3: Relevant parameters of the CDF endplug and forward calorimeter system

lengths constant as a function of η. The nominal depth of the calorimeter is $18X_0$ ($1X_0 = 1$ radiation length), including the superconducting coil in front of the calorimeter. At a depth of $6X_0$, there is a gas proportional chamber (CES) which is used to measure the profile of showers and their location. The resolution of the CEM calorimeter is

$$\frac{\sigma(E)}{E} = \frac{13.5\%}{\sqrt{E}} \tag{3.12}$$

(E in GeV) for electrons at normal incidence.

A schematic of the central electromagnetic calorimeter is given in figure 3.6. The light from each tower passes through a wave shifter, and a light guide which terminates in a phototube at the rear of the hadronic section.

The CES detector consists of orthogonal strips and wires. The strips measure the profile of the shower in z while the wires measure the profile in x where x is a local coordinate defined by the relation:

$$x = r\tan(\phi - \phi_0) \tag{3.13}$$

r is the distance of the center of the chamber from the z-axis, and ϕ_0 is the phi location of the center of the chamber. The energy deposited on each strip in z and on each pair of wires in x is recorded. The details of the chamber are given in table 3.4.

The x and z resolution for determining the shower centroid is 2 mm. The measurement of the shower profile is used to identify photon candidates, and

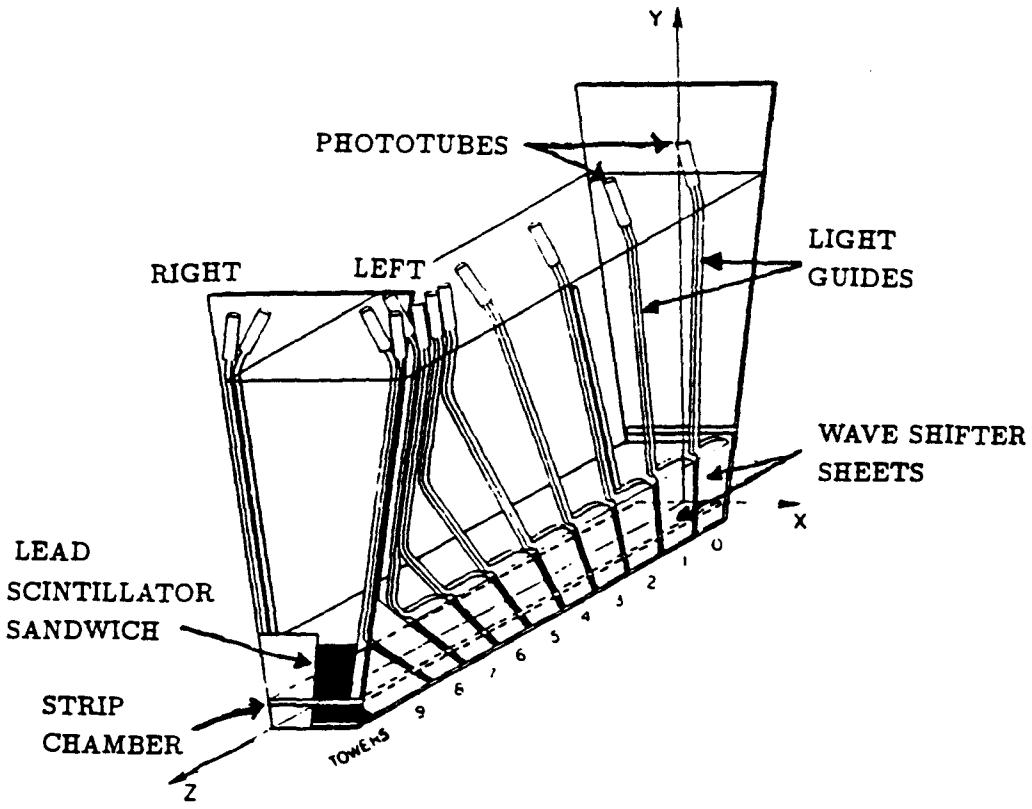

Figure 3.6: Schematic of the CEM calorimeter.

Perpendicular distance to beam line	184 cm
# Wire channels	64
Organization	
Split 121.2 cm from 90° edge	
Ganged in pairs except for edges (1.453 cm)	
# Strip channels	128
Organization	
6.2-121.2 cm from 90° edge	69 strips
121.2-239.6 cm from 90° edge	59 strips
Total thickness	0.75 in 0.069 radiation lengths 0.022 absorption lengths
Gas	95%/5% Ar/CO_2

Table 3.4: Properties of the CES chamber used to measure shower profiles in the central electromagnetic calorimeter

estimate the background to isolated single photons due to 2 photon decays of isolated neutral mesons.

3.2.2.2 The CEM Energy Scale

Much effort was put into the calibration of the CEM energy scale because of the importance of measuring the mass of the W boson. This calibration results in an accurate determination of the energy of photons. This section describes the corrections and calibrations applied to energies of electrons and photons measured using the CEM.

The CEM response to 50 GeV testbeam electrons was measured as a function of CES x and z over all ten towers for 5 wedges[20]. Figure 3.7 shows a typical response function over the face of a tower. These maps (one for each tower in η) were then used to correct the measured CEM energy.

Tower to tower variations were measured using inclusive electrons with $E_T >$ 12 GeV [21]. The mean $\frac{E}{p}$ is calculated for each of the 480 towers. Each tower is then corrected so that all towers have the same mean. The uncertainty in this correction is 1.7% due to poor statistics ($\approx$ 40 electrons / tower).

The final CEM energy scale was set by comparing the measured mean of the $\frac{E}{p}$ distribution for electrons from W decays to a Monte Carlo calculation of the expected mean. The modeling of the physics processes which govern energy loss before the electron reaches the calorimeter are well understood for high energy electrons. The momentum resolution of the CTC is 4.5 % for 40 GeV electrons.

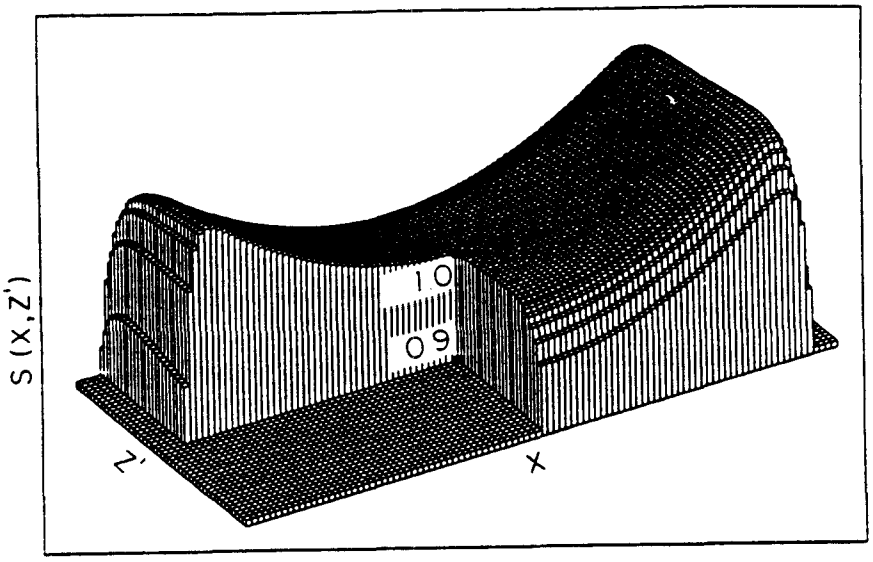

Figure 3.7: Response as a function of location in the tower normalized to the response at the center of the tower.

This factor dominates the statistical uncertainty in the measurement of $\frac{E}{p}$, which is 7%. This results in an uncertainty on the mean of 0.2%. Other uncertainties are due to the Monte Carlo calculation of the expected $\frac{E}{p}$ distribution and the simulation of the calorimeter. This procedure calibrated the energy scale to 0.5%.

3.2.2.3 Central Hadronic and Endwall Calorimeters

The central hadronic (endwall) calorimeter consists of 2.5 (5.1) cm steel absorber with scintillator sampling layers. The light from the scintillator is wave shifted, and then transported to phototubes at the rear of the calorimeter.

Including the coil and the electromagnetic portion gives a total depth of approximately 6 absorption lengths. The resolution, measured using testbeam pi-

ons, is $70\%\sqrt{E}$.

The energy scale of the calorimeter was obtained from the response of the calorimeter to testbeam pions. The calibration is maintained by monitoring the response of the calorimeter with ^{137}Cs sources. The measurement of the momentum of testbeam pions is accurate to 1% (see Appendix B for more details). The reproducibility of the source calibration gives an additional uncertainty of 4%.

3.2.2.4 The Plug and Forward Calorimeters

The endplug and forward calorimeters use gas sampling layers. The cell structure is described elsewhere [22, 23, 24]. Because the CTC efficiency is degraded for $|\eta| > 1.1$ it is difficult to separate showers due to neutral particles from showers due to charged particles. For this reason, the endplug calorimeter is only used to measure jets. The forward calorimeter does not add much acceptance for photon + two jet events, and furthermore the energy resolution for jets is worse due to noise. For this reason, it is only used in the calculation of the total transverse energy and the missing transverse energy.

The determination of the jet energy scale in the plug is accomplished by correlating it to the energy scale in the central calorimeter. This will be described in section 4.3.

Chapter 4

Selection of Photon and Two Jet Events

Figures 4.1 shows a lego display of a candidate photon + 2 jet event in the calorimeter. The height of the towers is proportional to the transverse energy (E_T) in the tower. Electromagnetic energy is shaded darker, hadronic energy is shaded lighter. Figure 4.2 shows the reconstructed tracks in the CTC. The two jets have numerous tracks pointing at the calorimeter clusters. The photon candidate has no tracks pointing at the calorimeter towers included in the cluster. Figure 4.3 shows the energy deposition and the measured profiles of the photon candidate in the wedge in which it is located.

This chapter describes how events are selected for this analysis. The dominant backgrounds are photons due to neutral meson decays. The method of measuring

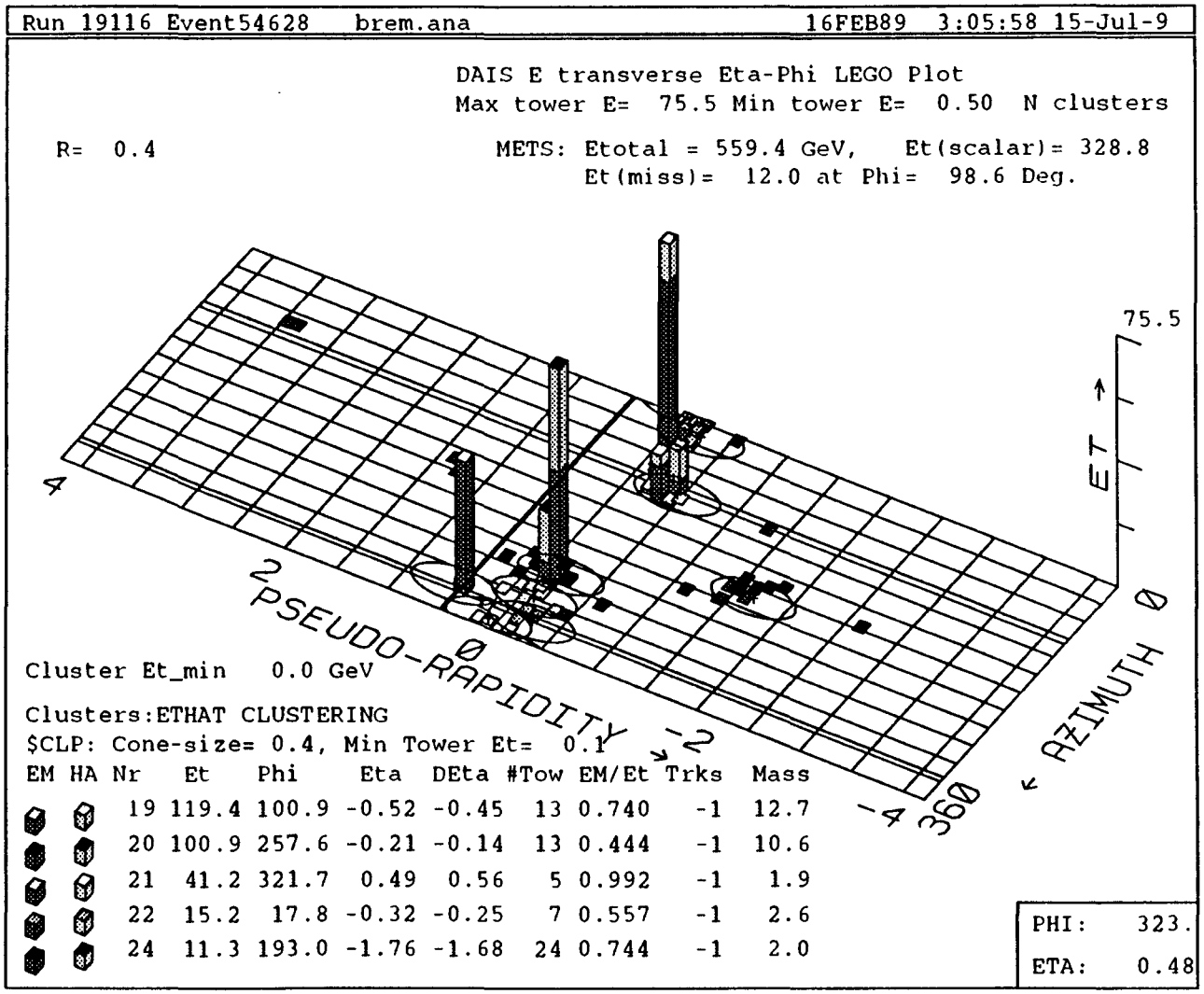

Figure 4.1: Lego display of a candidate photon + 2 jet event

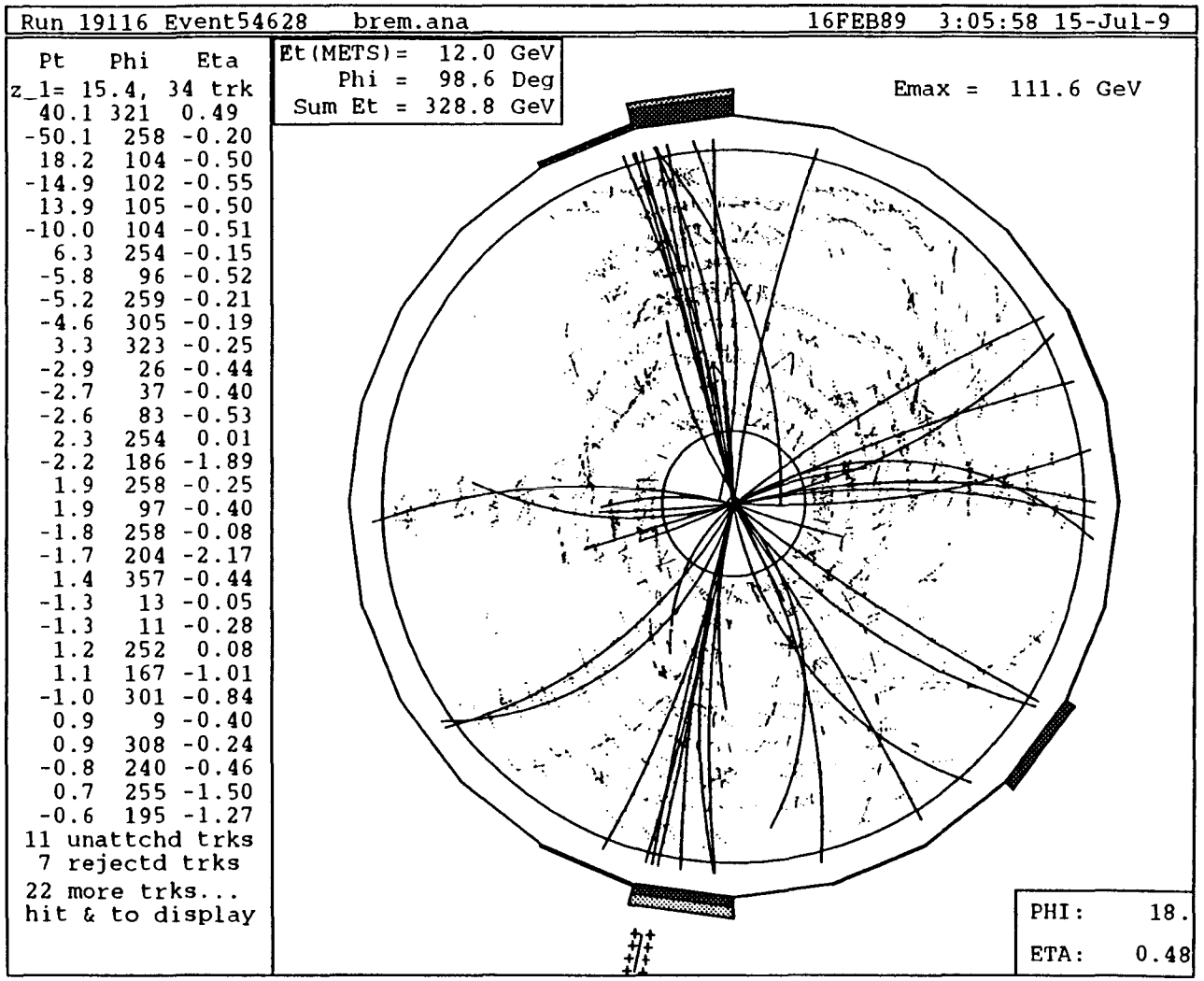

Figure 4.2: CTC display of a candidate photon + 2 jet event

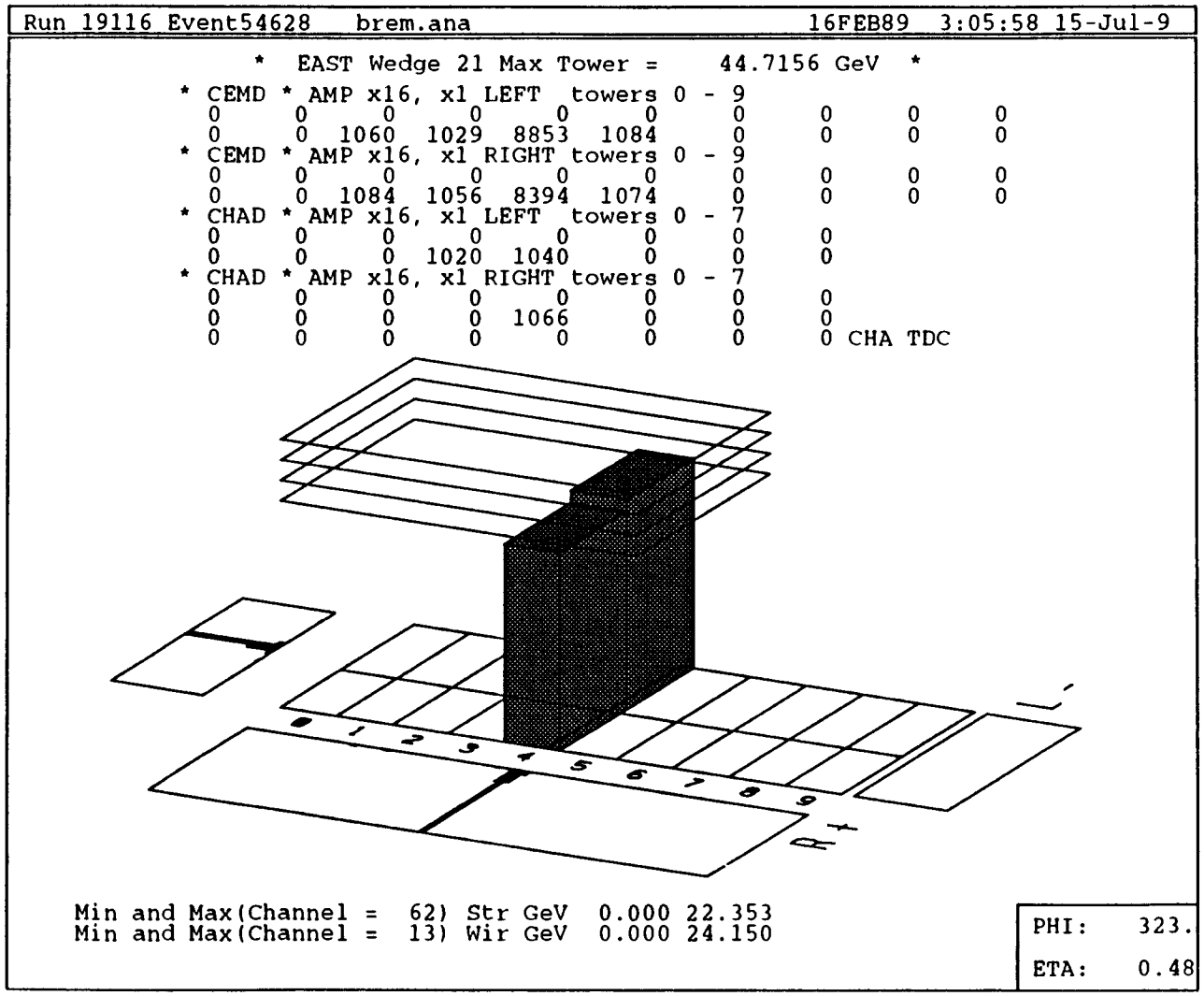

Figure 4.3: Wedge display of the candidate photon

photons at CDF is known as the energy dependent method. The method consists of trying to separate clusters due to two photons (π^0 and η^0 decays) from isolated single photons. Because of the low mass of the π^0 (134.97 MeV) and the somewhat low mass of the η^0 (547.45 MeV), the two photons have a very small opening angle if the meson energy is large ($\geq$ 5 GeV). Figure 4.4 shows the angular separation of the two photons as a function of the smaller energy of the two photons for different π^0 energies. If the energy is small or the separation is small, then the calorimeter sees a signal which is the same as that due to a single photon. However if the separation and the energy are large enough, then it is possible to distinguish clusters due to two photons from those due to single photons. This is only possible if the meson's energy falls in a particular range. (as is clear from figure 4.4). In CDF, the method is applied by fitting the shower profiles measured in the CES to the expected profile and using the quality of the fit to characterize the agreement with the hypothesis that the shower is due to single isolated photon (see figure 4.5)[6].

The data used in this analysis consists of $\approx$ 50000 photon triggers collected during the 1988-1989 Tevatron run at Fermilab. This section details how these 50000 triggers were selected, further criteria used to select isolated single photon candidates, and how the properties of jets were determined. The flow chart in figure 4.6 details the selection process and the criteria used in each step.

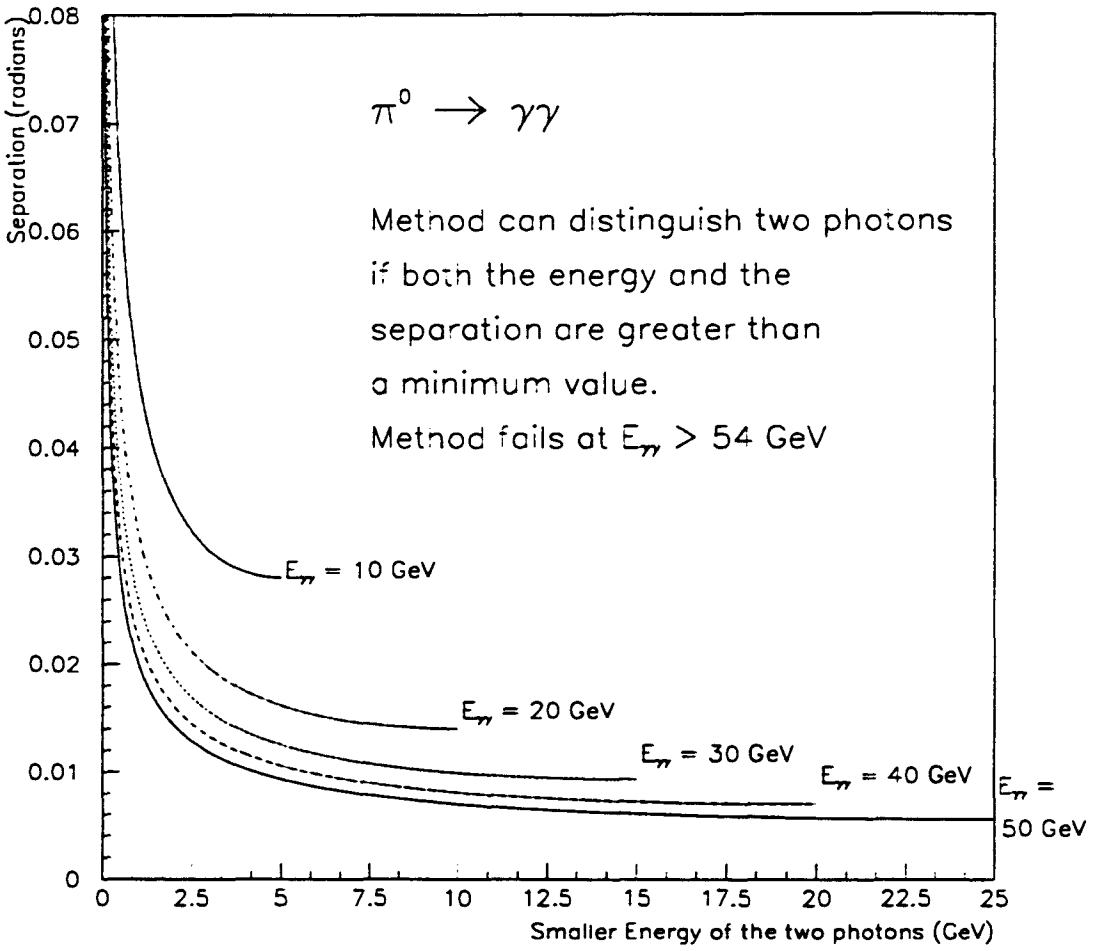

Figure 4.4: The angular separation of the two photons plotted as function of the lower energy of the two photons from π^0 decay. The different curves are for different energies of the parent π^0.

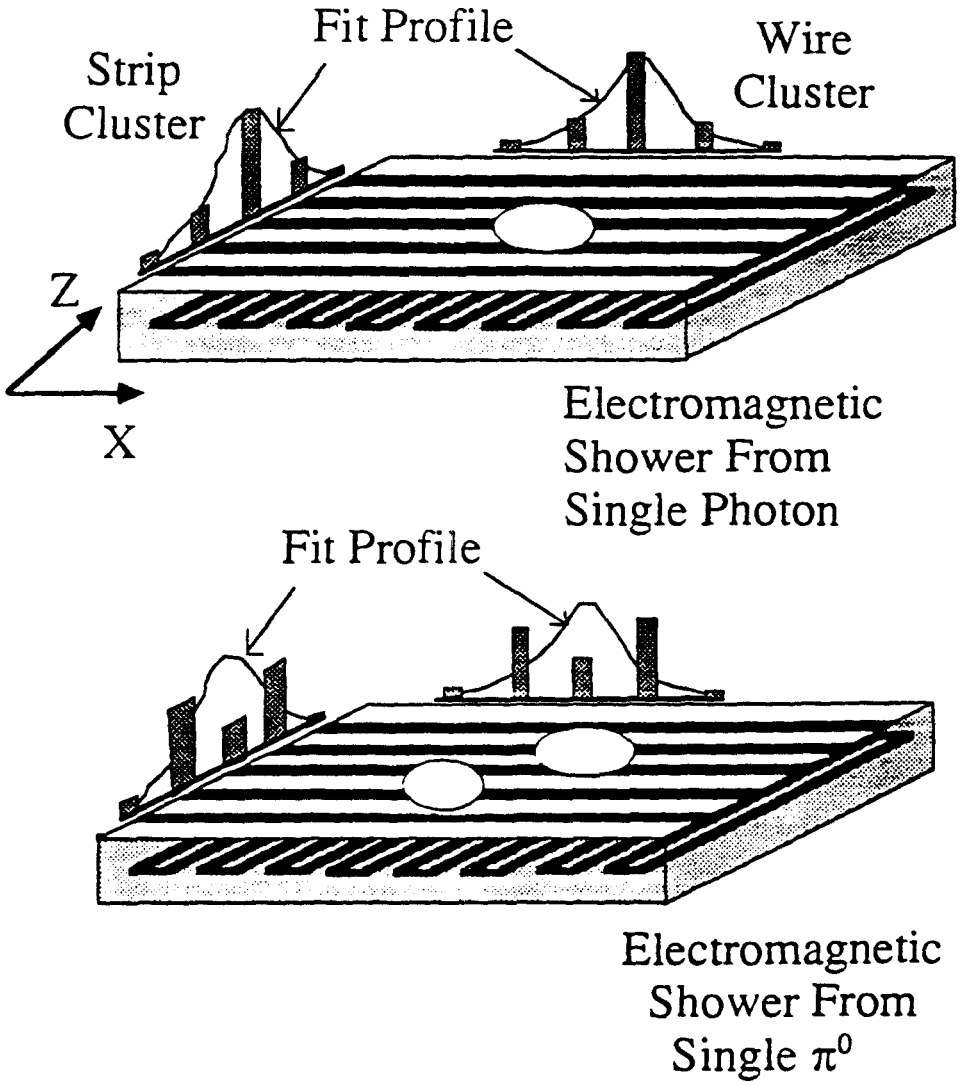

Figure 4.5: Schematic of a shower in the CES due to a single photon and of a shower due to a π^0. In both cases the resultant fit is the same due to the shower centroid and the total energy. However the χ^2 of the fit to the π^0 will be worse than that for the isolated single photon.

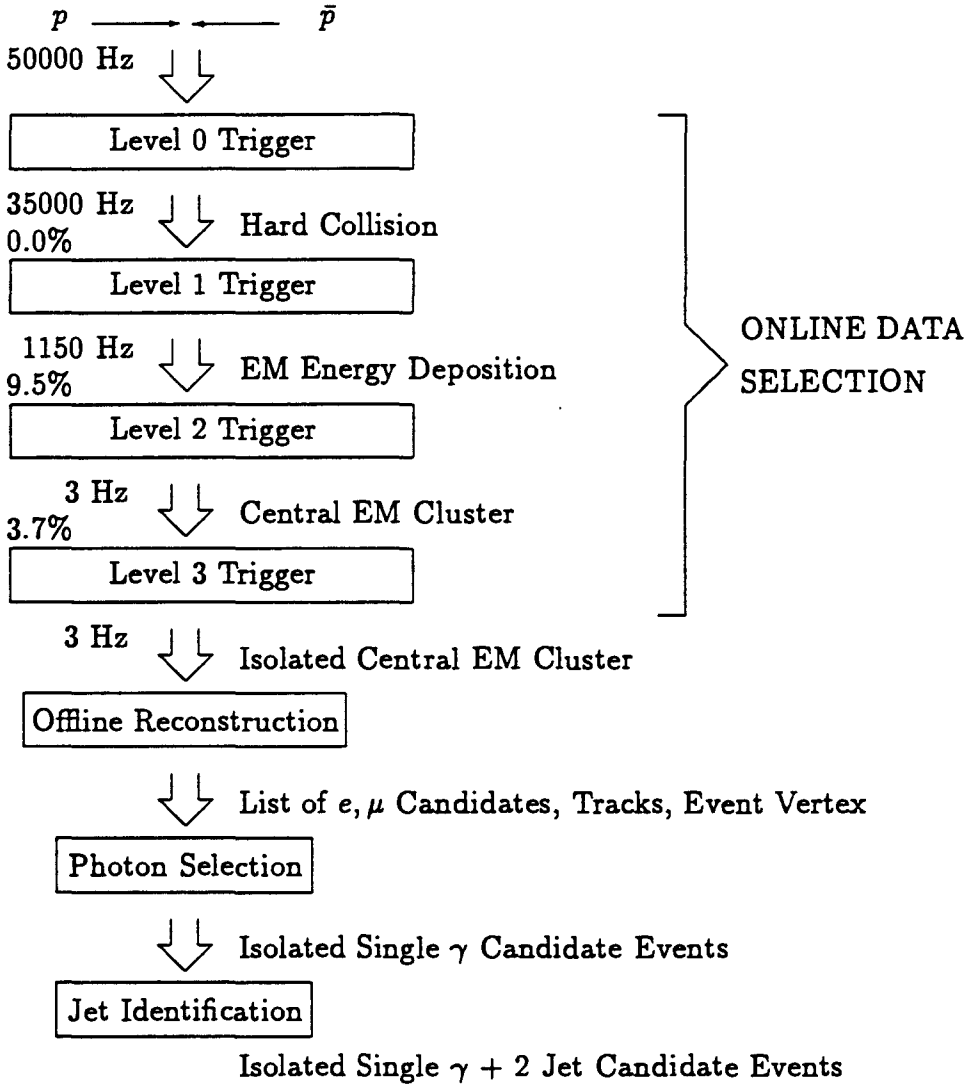

Figure 4.6: Details of the process of selecting photon + 2 jet events. The numbers (in Hz) above and below each trigger level give the input and output rate for a luminosity of 0.8×10^{30} cm^{-2} s^{-}1. Below each output rate is the deadtime in %. The data acquisition system incurs an additional deadtime of 7.2% after a Level 2 accept.

4.1 The CDF Trigger System

The following description of the trigger system focuses on the selection of photon candidates. Certain aspects of the trigger system are ignored because they are irrelevant to this analysis. The components of the trigger system which identify muons will not be mentioned, nor will there be any mention of the tracking information used by the trigger.

The trigger system consists of four parts or levels. Level 0 is used to determine whether an event might have occurred. The decision time is less than the time between beam crossings (= 3.5 μsec). Level 1 looks for large transverse energy deposition in the calorimeters. It requires two beam crossings to make a decision. Level 2 looks for clustered energy deposition. The Level 2 decision time is typically 20 μsec. After an event is accepted by Level 2, the data from the detector is read. This takes 5-6 msec. Lastly, Level 3 processes the events with an abbreviated version of the offline reconstruction code and further refines the selection based on information from the calorimeter. It does not reject very many events, but it aids in classifying the source of the events. The hardware implementation of the trigger is described elsewhere [25, 26, 27].

The Level 0 trigger consists of scintillator planes at both ends of the interaction region. Any hard collision will be accompanied by fragments traveling along the beam pipe. These scintillator planes detect the fragments of the colliding protons and anti-protons. The Level 0 trigger is also referred to as a minimum

bias trigger. A small fraction of events which passed the Level 0 trigger were written to tape and used to study acceptances.

At this point it is necessary to give a brief overview of how the data from the detector are read. Each phototube or pad connected to a calorimeter cell is connected to a charge integrating amplifier. The charge integration starts 600 ns before a beam crossing. The charge integration stops $\approx$ 1600ns after a beam crossing (though this time varies depending on the detector element). Until a candidate event is rejected, the amplifiers are not cleared of their contents. At a time which corresponds to 30% of the signal pulse being integrated, a signal proportional to the accumulated charge is loaded from each calorimeter cell into dedicated trigger electronics. Cells are grouped in trigger towers which measure $0.2(\eta) \times 15^0(\phi)$. The Level 1 trigger required 6 GeV in a single *trigger* tower of the central electromagnetic calorimeter.

The Level 2 trigger refined the calorimeter selection. The pattern of energy deposition in the trigger towers was clustered. Photon/electron candidates must have had a transverse energy of at least 23 GeV, and the hadronic energy must have been less than 12.5% of the electromagnetic energy.

The level 3 trigger system consisted of a farm of 60 processors. At this point, all the data from the event was available. A "fast" version of the reconstruction code was used to process the data from the calorimeters and muon detectors. No use was made of the tracking information because of time constraints. Each Level 3 node needed $\approx$ 2.1 seconds to process the calorimeter information. Re-

constructing the information from the tracking detectors would have added ≈ 60 seconds.

The isolation, I, was defined by

$$I = \frac{1}{E_T^\gamma}\left(\sum_{i:\Delta R^i<0.4} E_T^i\right) - 1 \tag{4.1}$$

where

$$\Delta R^i = \sqrt{(\phi^i - \phi^\gamma)^2 + (\eta^i - \eta^\gamma)^2} \tag{4.2}$$

Here ϕ^i and η^i are the coordinates of tower i. This definition is illustrated in figure 4.7. The trigger required $I < 0.15$.

The shower shape was characterized by

$$L_{\rm SHR} = 0.14 \sum_i \frac{E_i - T_i}{0.14 E_{\rm clus} \ominus \Delta T_i} \tag{4.3}$$

where i refers to the towers in the cluster, E_i is the energy of the i^{th} tower, T_i is the expected energy in the i^{th} tower from testbeam measurements, and ΔT_i is the uncertainty in T_i due to a 1 cm error in the z vertex. This variable characterizes the agreement between the measured shower shape and the expected shape as measured using testbeam electrons. Figure 4.8 shows the distribution of $L_{\rm SHR}$ for electrons from W decays. The Level 3 trigger required that $L_{\rm SHR} < 0.2$.

4.2 Identification of Photon Candidates

At this point the sample consisted of all events which contained an isolated deposition of electromagnetic energy in the central calorimeter. Besides single pho-

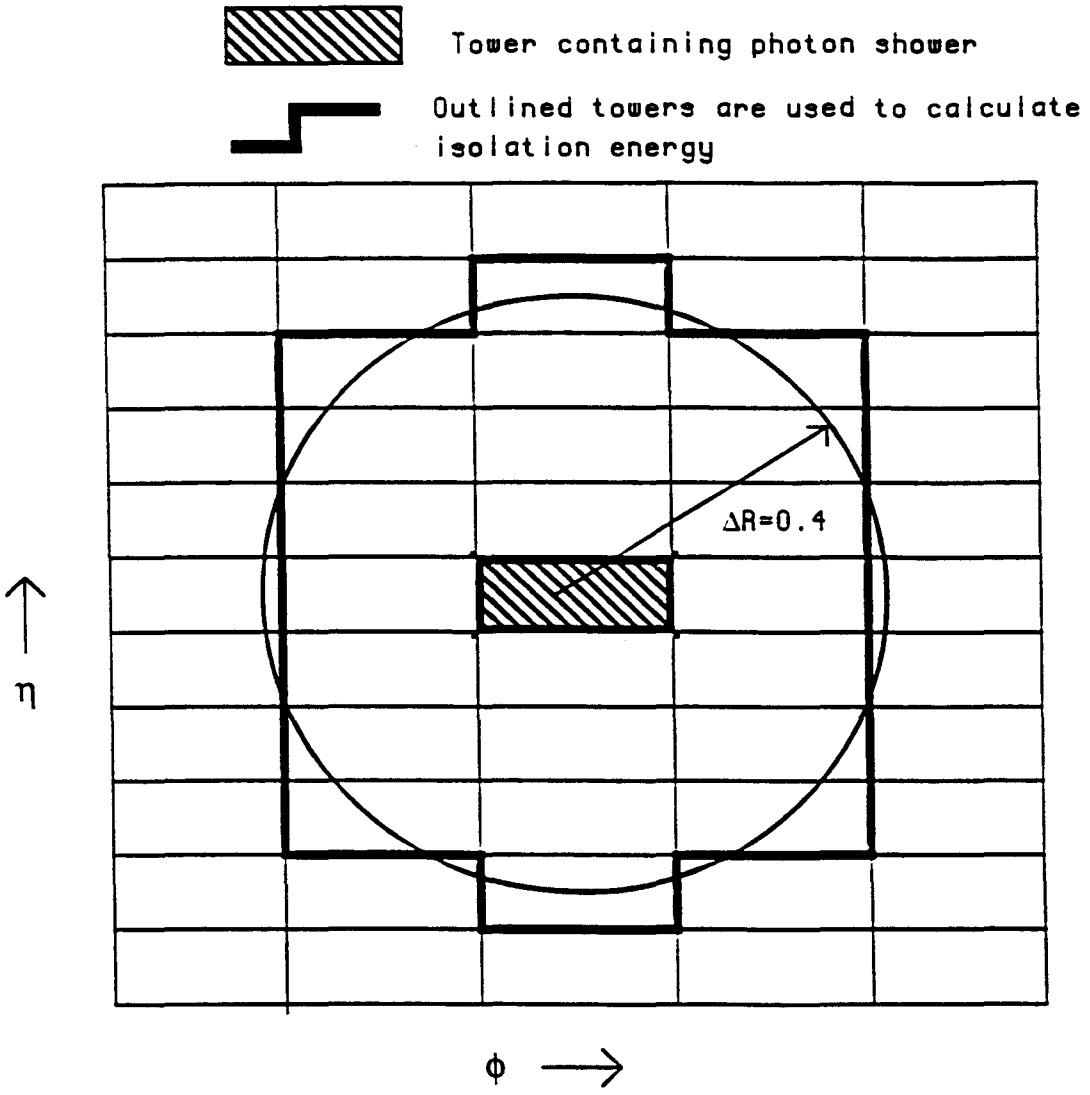

Figure 4.7: Schematic illustrating the definition of isolation cones in the central EM calorimeter.

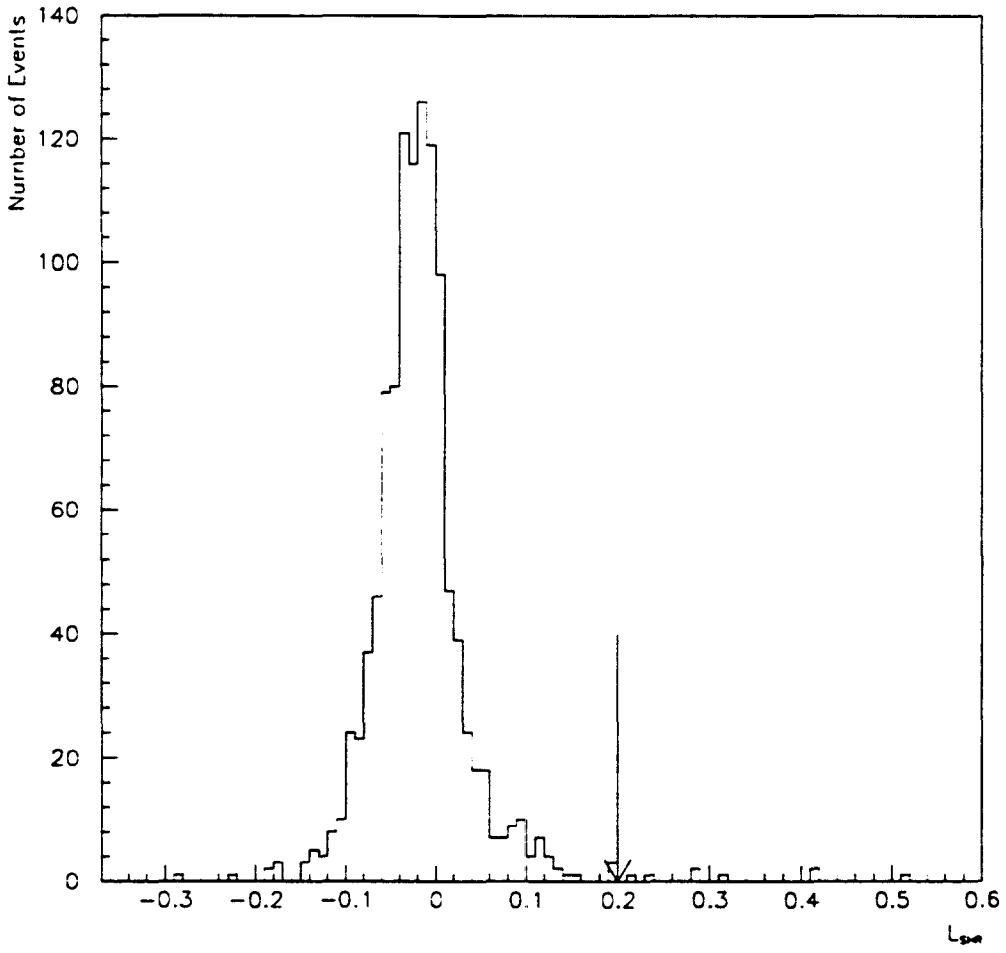

Figure 4.8: The L_{SHR} distribution for electron from W decays.

there were events due to isolated production of neutral mesons (π^0's and ηs), electrons, charged hadrons, and photons from cosmic rays.

In addition to events satisfying the $L_{\rm SHR}$ trigger, there were also events which satisfied a trigger which placed no requirements on $L_{\rm SHR}$, but increased the isolation cone for the calculation of I to a radius of 0.7. These events are not used in this analysis because they unnecessarily reduce the acceptance for photon + 2 jet events. They are included here as a check on the trigger efficiency as there is a 75 % overlap between the two triggers.

Charged particles were removed by requiring that no track point at any of the calorimeter towers included in the cluster. Photons due to cosmic rays were removed by requiring that the missing transverse energy ($\not\!\!E_T$) be consistent with no $\not\!\!E_T$. Momentum conservation implies

$$E_{Tx} = \sum_i E_i \sin\theta_i \cos\phi_i = 0 \tag{4.4}$$

$$E_{Ty} = \sum_i E_i \sin\theta_i \sin\phi_i = 0 \tag{4.5}$$

where the sum is over all towers in the calorimeter. $\not\!\!E_T$ is defined by

$$\not\!\!E_T = E_{Tx} \oplus E_{Ty} \tag{4.6}$$

The $\not\!\!E_T$ resolution is given by

$$\sigma_{\not\!\!E_T} = 100\%/\sum_i E_i \sin\theta_i \tag{4.7}$$

where again the sum is over all towers in the calorimeter. This analysis requires that

$$\not\!\!E_T < 3.0\sigma_{\not\!\!E_T} \tag{4.8}$$

The z vertex of the event was required to be within 60 cm of the geometric center of the detector to ensure that the event was well measured in the calorimeter (due to the projective towers). This rejects a small fraction of events on the tail of the z vertex distribution (see figure 4.9).

The remaining background is due to neutral meson decays. Since the method depends on the CES, the profiles must be in the fiducial region of both the strips and the wires. Hence

$$14.0 < z_{\text{strip}} < 217.0, \quad |x_{\text{wire}}| < 17.5 \tag{4.9}$$

where z_{strip} and x_{wire} are defined :

$$z_{\text{strip}} = \frac{\sum_{s=s_{\text{seed}}-5}^{s_{\text{seed}}+5} E_s z_s}{\sum_{s=s_{\text{seed}}-5}^{s_{\text{seed}}+5} E_s} \tag{4.10}$$

$$x_{\text{wire}} = \frac{\sum_{w=w_{\text{seed}}-5}^{w_{\text{seed}}+5} E_w x_w}{\sum_{w=w_{\text{seed}}-5}^{w_{\text{seed}}+5} E_w} \tag{4.11}$$

Here s (w) refers to the strips (wires). E_s (E_w) is the energy measured on a particular strip (wire). The seed strip is the strip with the highest energy contained in the cluster.

Photon candidates were required to have at least 1 cluster in both views. Obvious meson candidates were removed by requiring that there be no second cluster in either view with energy greater than 1 GeV as measured in the CES. This last requirement introduces an inefficiency which is measured using testbeam electrons (see figure 4.10).

The likelihood that a cluster is due to a single photon was determined by first estimating the true energy and the true centroid of the cluster using an

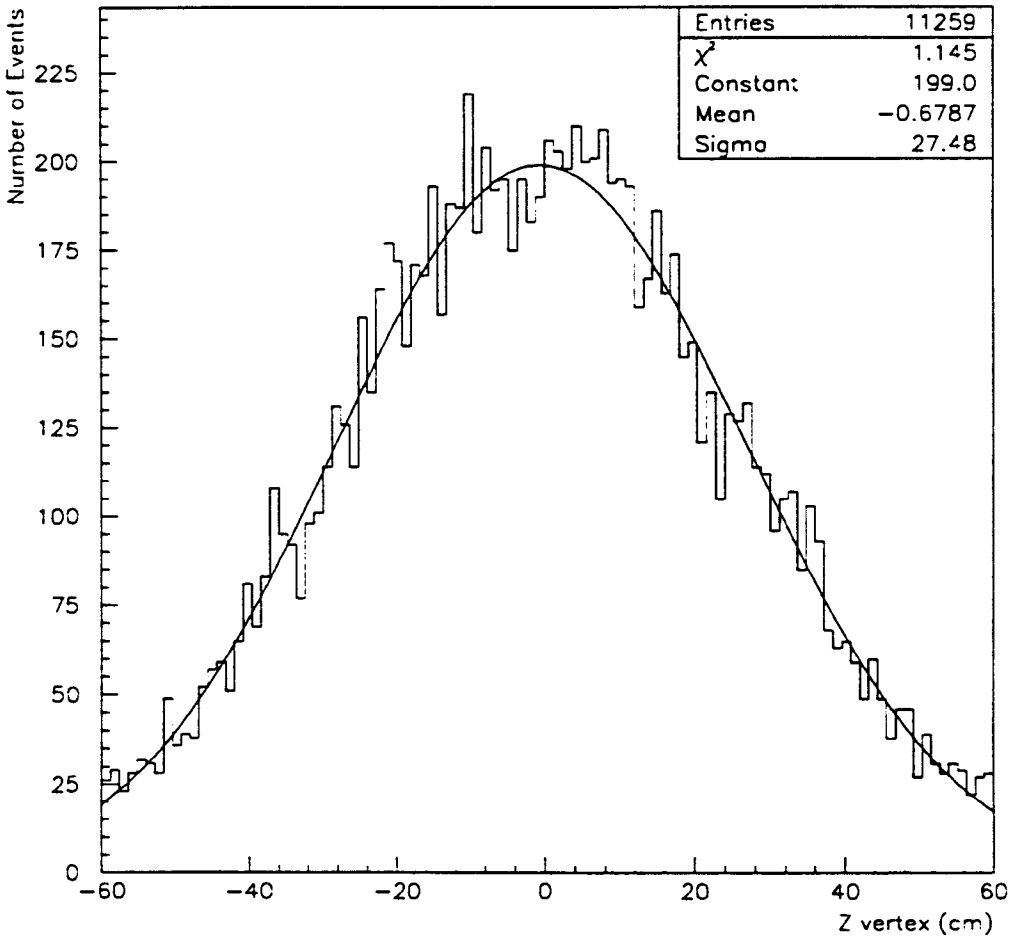

Figure 4.9: z vertex distribution of the inclusive single photon candidate event sample.

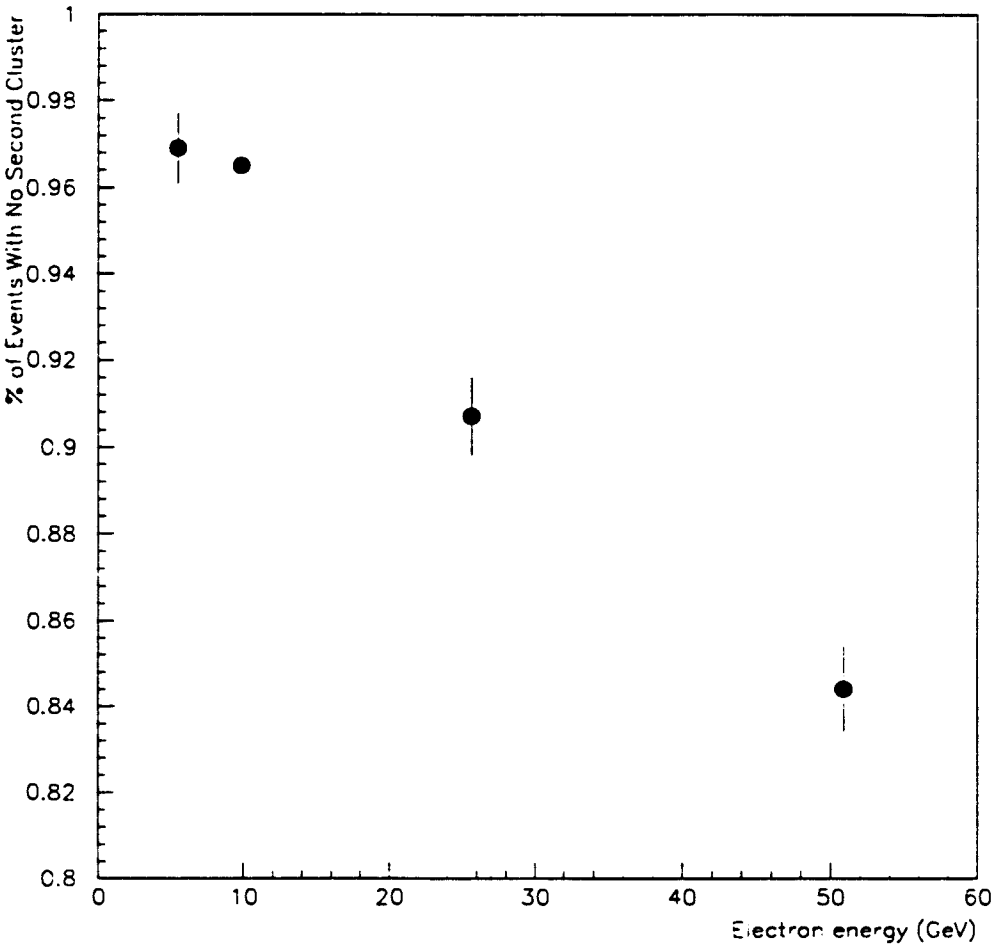

Figure 4.10: Acceptance of the no second cluster requirement determined from testbeam electrons.

iterative χ^2 fit (see Appendix C for a general discussion of fitting techniques). The resulting χ^2 for the strips is given by

$$\chi^2_s = \sum_{s=-5}^{5} \frac{(y_s - E_s)^2}{\sigma_s^2} \tag{4.12}$$

where y_s is the expected energy on strip, s, and E_s is the measured energy on strip, s, and σ_s is the uncertainty on the measured value. The resulting χ^2_s is a measure of how consistent the measured strip profile is with the expected strip profile due to an isolated electron. χ^2_w is defined in exactly the same manner.

The information from the strips and wires was combined by using the average of the χ^2 from the two views to characterize the shower profile. The following definition will be used hereafter:

$$\tilde{\chi}^2 = \frac{1}{2}(\chi^2_s + \chi^2_w) \tag{4.13}$$

To estimate the remaining background one compares the fraction of events which have $\tilde{\chi}^2 < 4$ to the number of events which have $\tilde{\chi}^2 < 20$ (see figure 4.11). This ratio is 80% for isolated single photons and rises from 45% to 65% for the background over the E_T range considered here (figure 4.12). Define ϵ_S (ϵ_B) to be the fraction of single isolated photons (photons due to meson decays) with $\tilde{\chi}^2 < 4$. Then one can write

$$\begin{pmatrix} N_{\tilde{\chi}^2<4} \\ N_{\tilde{\chi}^2>4} \end{pmatrix} = \begin{pmatrix} \epsilon_S & \epsilon_B \\ 1-\epsilon_S & 1-\epsilon_B \end{pmatrix} \begin{pmatrix} N_S \\ N_B \end{pmatrix} \tag{4.14}$$

where N_S and N_B are the number of single photons and the number of neutral meson decays respectively. Solving the equation gives

$$\begin{pmatrix} N_S \\ N_B \end{pmatrix} = \frac{1}{\epsilon_S - \epsilon_B} \begin{pmatrix} 1-\epsilon_B & -\epsilon_B \\ \epsilon_S - 1 & \epsilon_S \end{pmatrix} \begin{pmatrix} N_{\tilde{\chi}^2<4} \\ N_{\tilde{\chi}^2>4} \end{pmatrix} \tag{4.15}$$

Equation 4.15 defines a method for counting the number of photon events and the number of background events. Define weights as follows:

$$\left.\begin{array}{l} w_S = \frac{1-\epsilon_B}{\epsilon_S-\epsilon_B} \\ w_B = \frac{\epsilon_S-1}{\epsilon_S-\epsilon_B} \end{array}\right\} \tilde{\chi}^2 < 4, \qquad \left.\begin{array}{l} w_S = \frac{-\epsilon_B}{\epsilon_S-\epsilon_B} \\ w_B = \frac{\epsilon_S}{\epsilon_S-\epsilon_B} \end{array}\right\} \tilde{\chi}^2 > 4 \tag{4.16}$$

For each event, its contribution to the signal is given by w_S and its contribution to the background by w_B. ϵ_S and ϵ_B are functions of the candidate photon E_T. They are determined by correcting the measured profiles of testbeam electrons for differences between electron showers and photon showers and then performing a Monte Carlo integration using the measured showers as a basis for determining the $\tilde{\chi}^2$ distribution of simulated photon showers and the $\tilde{\chi}^2$ distribution of the neutral meson background.

Figure 4.13 shows the isolation distribution for the entire sample and also the distribution for the measured background using the weights determined from equation 4.15. The data beyond an I of 0.05 are consistent with being all background. This defines the final isolation cut.

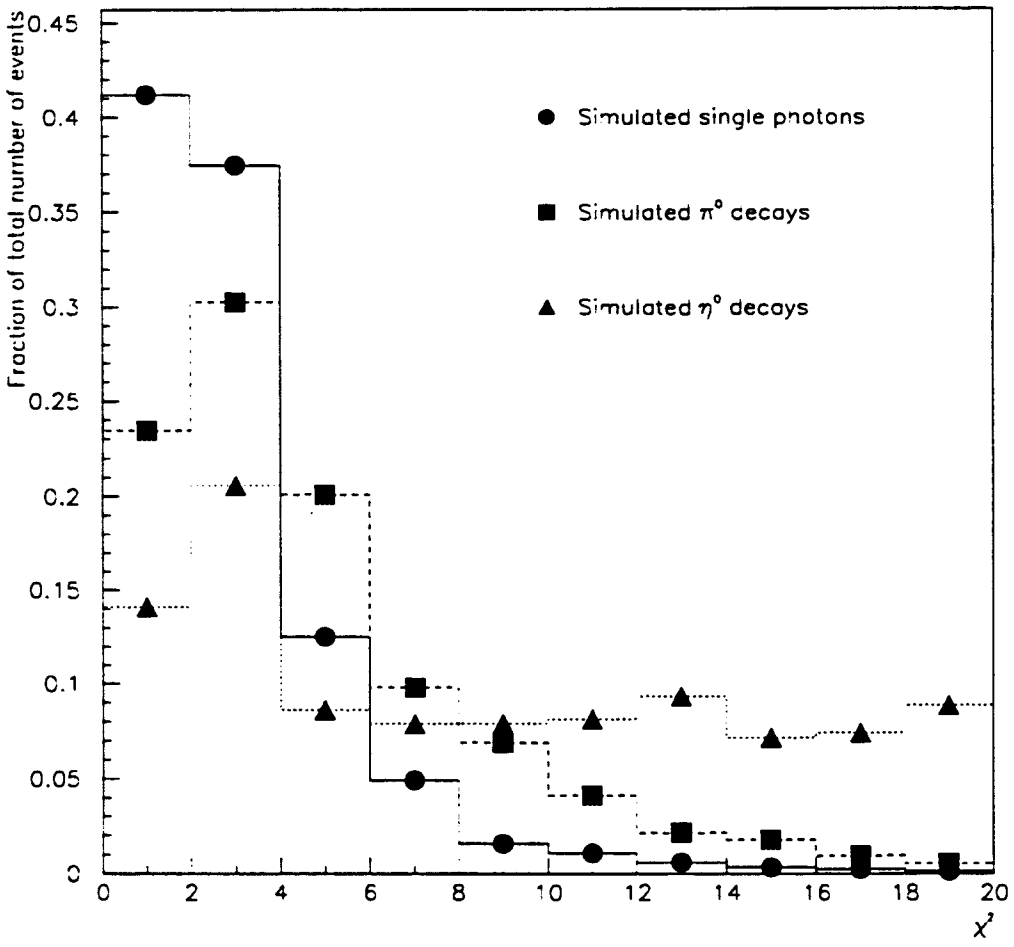

Figure 4.11: Simulated $\tilde{\chi}^2$ distribution for photon candidates with $28 < E_T < 32$ GeV. Shown are the distributions for single photons, photons due to π^0 decays, and photons due to η^0 decays.

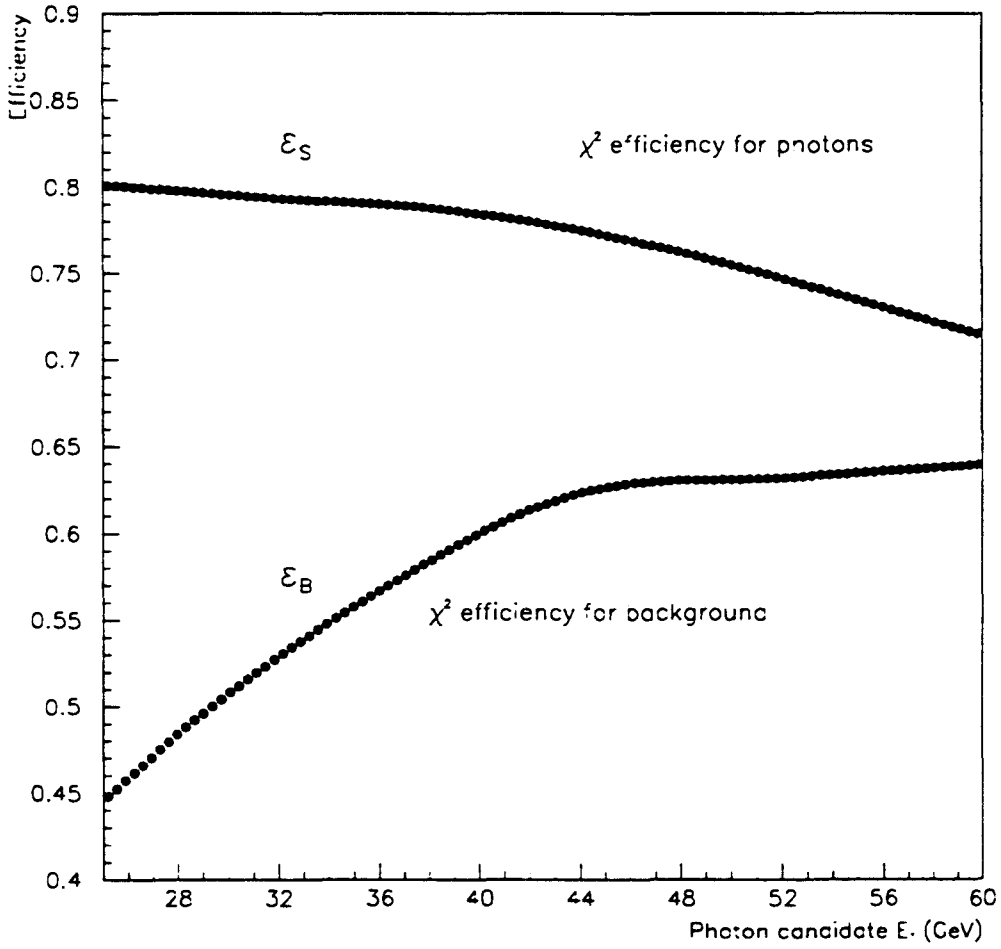

Figure 4.12: $N(\tilde{\chi}^2 < 4)/N(\tilde{\chi}^2 < 20)$ as a function of E_T. The efficiencies are extracted from a Monte Carlo simulation of photon showers.

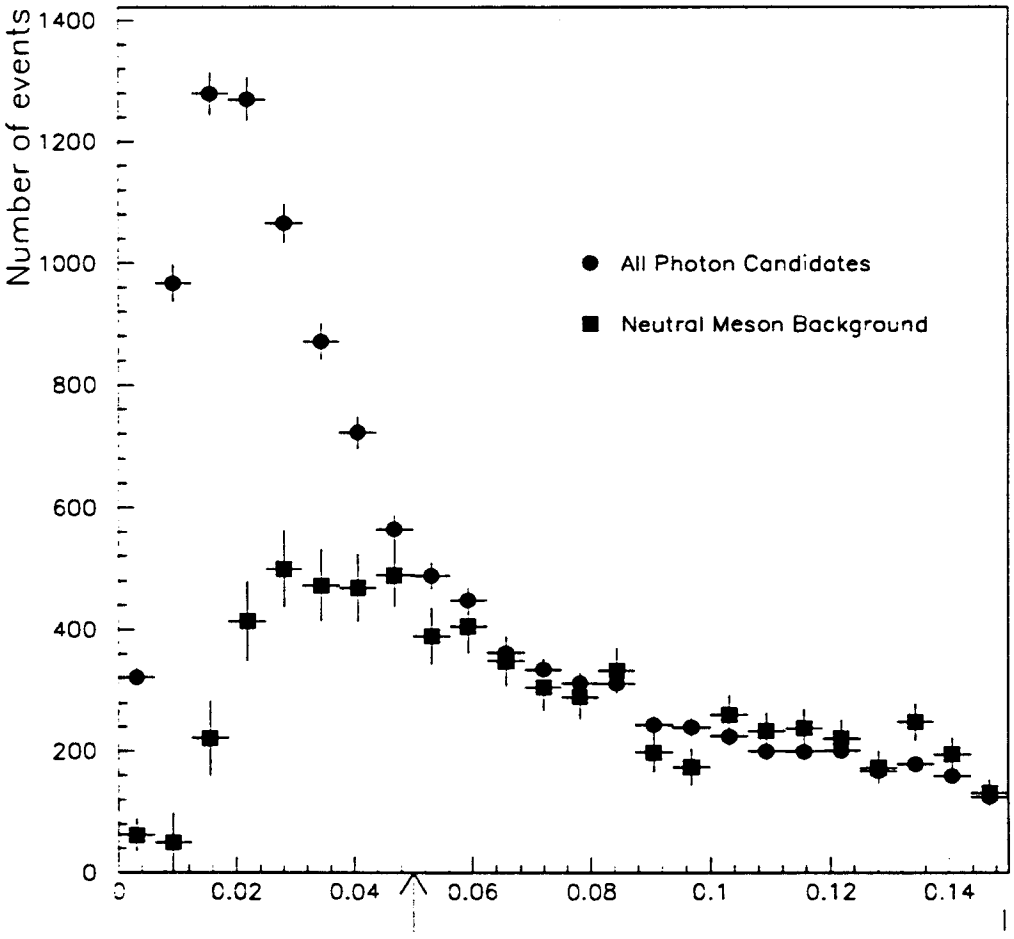

Figure 4.13: Isolation (as defined in the text) for the entire sample and for the measured background. The isolated photon signal has $I < 0.05$

4.2.1 Trigger Efficiency and Acceptance for Isolated Single Photons

4.2.1.1 Trigger Efficiency

The trigger made the following requirements:

- Level 2
  - E_T of candidate $> 23GeV$
  - Had. energy / EM energy < 0.125
- Level 3
  - $I_{\Delta R<0.4} < 0.15$
  - $L_{\rm SHR} < 0.2$

The efficiency of the trigger as a function of E_T [28] was measured using a trigger whose nominal threshold was 10 GeV. The fraction of events which passed the 23 GeV trigger is shown in figure 4.14. The data were corrected using the results of the fit.

Clusters due to isolated single photons should have little or no hadronic energy associated with the EM cluster. There is some leakage of energy into the hadronic calorimeter, but this is always smaller than 12.5% of the photon's E_T. The efficiency of the $L_{\rm SHR}$ requirement was measured using the $L_{\rm SHR}$ distribution of

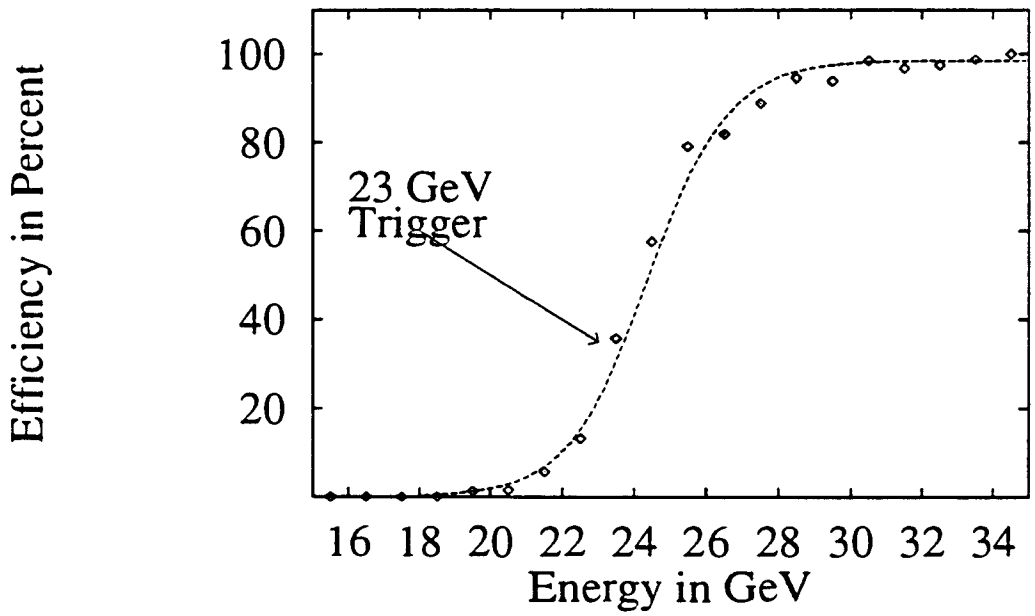

Figure 4.14: Efficiency of the Level 2 23 GeV Photon Trigger as a function of E_T.

electrons to be 99.2%. The final isolation requirement was stronger than that in the trigger.

4.2.1.2 Acceptance

The largest factor in the acceptance is due to the requirement that the CES cluster be within the fiducial region of the detector. This factor is 64%. The no second cluster requirement is measured using testbeam electrons. The acceptance of the isolation requirement was measured by asking how often in a random cone of radius 0.4 in a minimum bias event did one observe a transverse energy greater than a particular value (corresponding to 5% of the photon E_T). Figure 4.15 shows the resulting acceptance. The acceptance of the requirement that there be no track was measured using the track density in the CTC in minimum bias events. It is 96.5%. The z vertex distribution is well fit by a gaussian of width 32.4 cm. A cut of 60 cm excludes 5% of the data. The acceptance is summarized in table 4.1.

4.3 Jet Identification

Jets are defined as clusters of energy found in the calorimeter. The first step was clump clustering. All calorimeter towers with $E_T > 0.1$ GeV were ordered in transverse energy. If the first tower had less than 1 GeV then no clusters were formed. Otherwise the first tower became the first cluster. Subsequent towers in

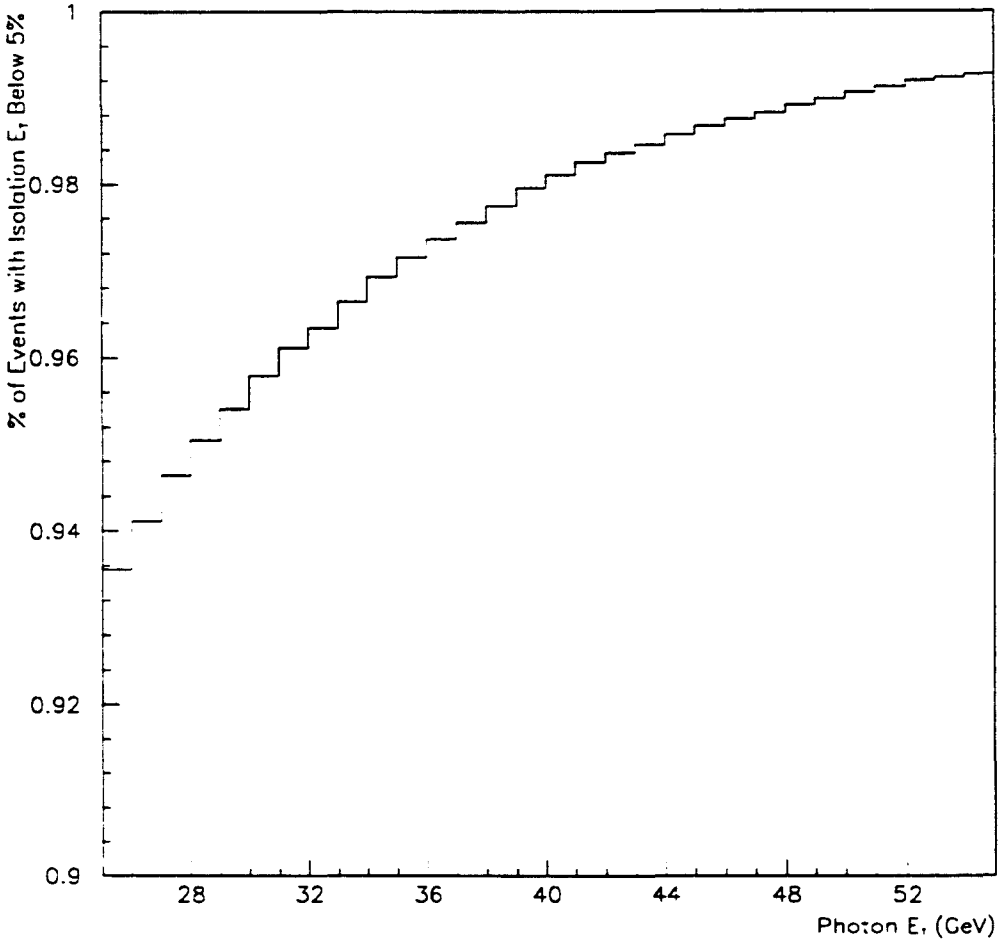

Figure 4.15: The acceptance of the isolation requirement calculated from the distribution of E_T in random cones as measured in minimum bias events.

Trigger	
Requirement	Efficiency
$E_T > 25$ GeV	[0.60-0.985]
HAD/EM < 0.125	1.00
$L_{\rm SHR} < 0.20$	0.992
Data Selection	
Requirement	Acceptance
No track	0.9650
crack in CES chambers (no cluster)	0.9700
$14.0 < \lvert Z^{\rm strip}\rvert < 217.0$	0.9165
$\lvert X^{\rm wire}\rvert < 17.5$	0.7228
$\lvert Z^{\rm vertex}\rvert < 60.0$ cm	0.9388
Extra CES cluster cut	[0.95-0.85]
Isolation	[0.93-0.99]

Table 4.1: Details of the trigger efficiency and the acceptance for isolated single photons. The total acceptance ranges between 0.4 and 0.5.

the list were added to a cluster if they were adjacent to any of the towers already contained in the cluster. If the tower was not adjacent to any of the already found clusters, and it had at least 1 GeV, then it was taken to be the first element of a new cluster. The result of the algorithm was a list of clusters where each cluster was a clump of energy deposition.

The next step was a fixed cone algorithm. The algorithm considered each cluster found by clump clustering in turn. The η and ϕ centroid of the cluster were determined. Then towers with more than 0.1 GeV and within a radius of 0.4 of the cluster centroid were added to the cluster. If the tower list did not change, then the algorithm proceeded to the next cluster. Otherwise the cluster centroid was recalculated and the procedure repeated until the list of towers remained the same or the algorithm had operated a 100 times. The limit of 100 protected the algorithm from situations where the cluster was stable, but several towers containing small amounts of energy caused the centroid to oscillate.

The last step was to resolve ambiguities resulting from the preceding step. First, any cluster which was fully contained in another cluster was deleted. Secondly, two clusters which shared more than 75% of the energy of either cluster were merged. Lastly, an iterative procedure split towers which were shared between two clusters whose overlap energy was less than 75% of the energy of either cluster. This procedure split the shared towers such that the tower was included in the nearest cluster. The centroids were recalculated, and the splitting recalculated. The procedure continued until the splitting was stable or a 100 iterations

had taken place.

The algorithm can be characterized by the resolving power for separating jets due to two distinct partons. This separation is a function of the E_T of both partons, and their separation. Figure 4.16 shows the number of jet pairs as a function of their separation. The data is from the direct photon sample. Both jets were required to have an E_T of at least 10 GeV. The sharp rise at $\Delta R = 0.5$ is due to the jet separation efficiency. The slow descent at larger separations is characteristic of gluon radiation, which forms a second jet near the primary one. The shape of the distribution is fit to the functional form

$$f(R) = \frac{A}{\Delta R^B} \times (1 + \tanh \alpha(\Delta R - \Delta R_0)) \tag{4.17}$$

where the first term describes the physics, and the second term describes the jet separation efficiency. ΔR_0 is the point at which the efficiency is 50%. The fit values are given in table 4.2.

The jets were corrected for variations in response in pseudorapidity. The correction function [29] is determined from dijet events where at least one jet had to be in the well understood region of the central calorimeter: $0.2 < |\eta| < 0.7$. This jet was referred to as the trigger jet, and the other jet was referred to as the probe jet. In cases where both jets were in trigger region, one jet was randomly chosen as the trigger jet. The correction function was

$$R(\eta^{probe}) = \frac{1+\beta}{1-\beta}$$

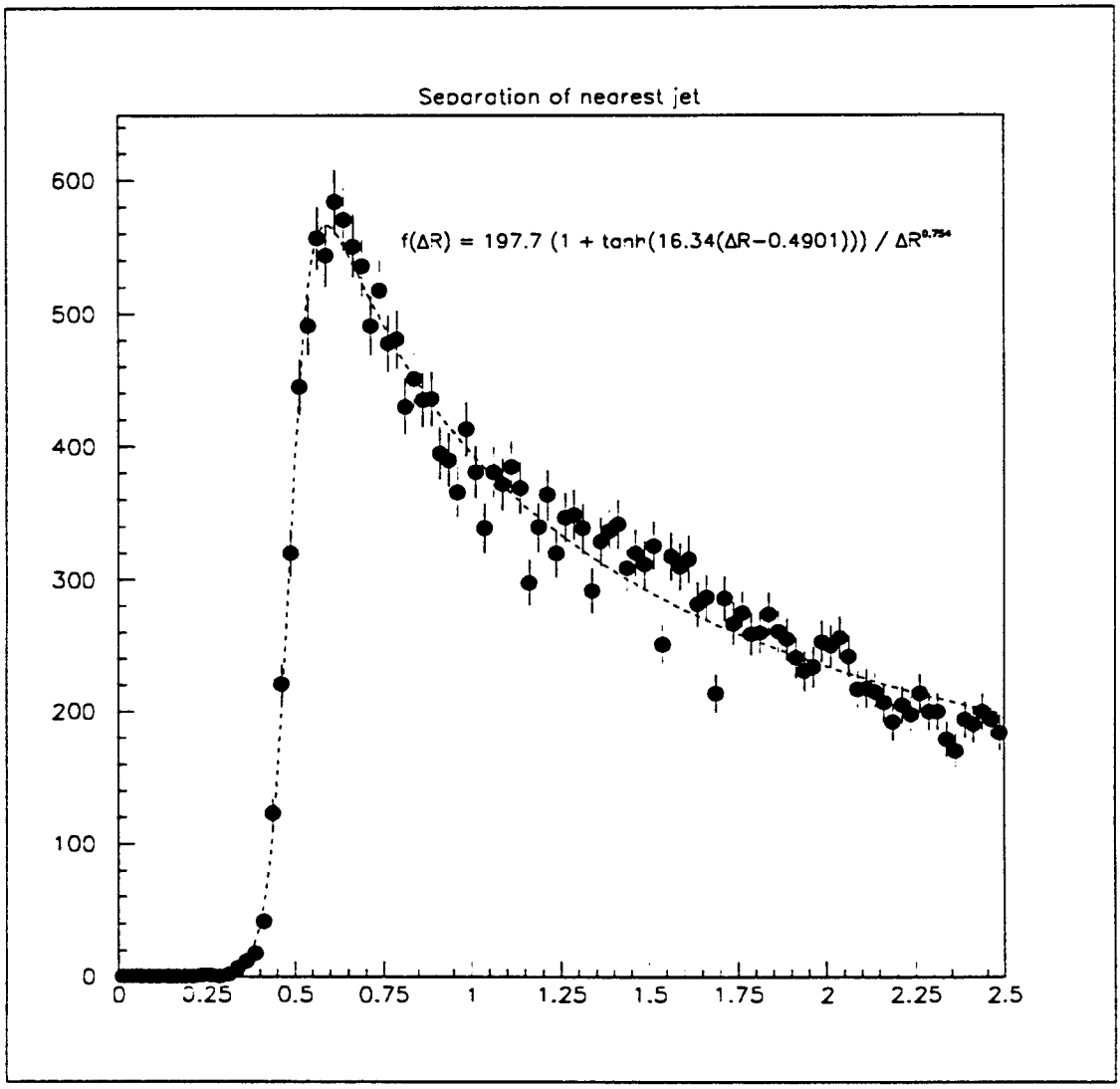

Figure 4.16: Separation of each jet from its nearest neighbor

Normalization	A	197.7
Power of ΔR	B	0.754
Slope of efficiency function	α	16.34
Point of 50% efficiency	ΔR_0	0.4901

Table 4.2: Parameters of the jet separation efficiency function for a cone clustering radius of 0.4.

where

$$\beta = \frac{\vec{\not{E}}_T \cdot \vec{p_T}^{\text{probe}}}{|\vec{p_T}^{\text{trigger}}| + |\vec{p_T}^{\text{probe}}|}$$

The reason for using the missing transverse energy projected along the probe jet was to avoid including effects other than those due to cracks in the calorimeter coverage or variations in the energy scale across calorimeters. R as a function of η is shown in figure 4.17.

The jets were now corrected for the non-linearity of the central calorimeter. This was necessary to be able to compare the properties of the events presented here to theoretical calculations. At some parton transverse energy, the efficiency for finding a jet due to a parton begins to drop. It is necessary to only consider jets above this point for a meaningful measurement. The advantage of this approach was that the corrected energy of the jet corresponded to the energy of the parent

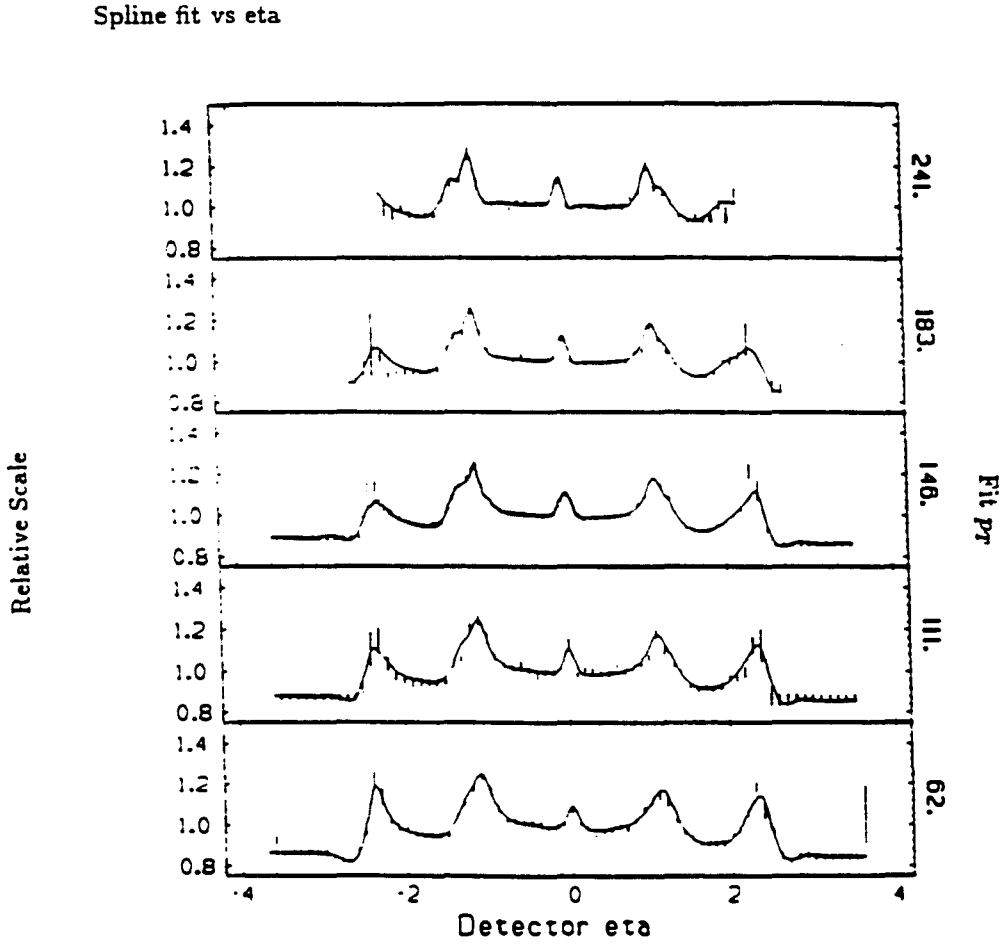

Figure 4.17: Correction function for cracks in the calorimeter coverage as determined using dijet balancing.

parton.

The probability of observing a single jet with a given measured E_T is

$$\text{PROB}(E_T^{\text{meas}}) = \int \text{PROB}(E_T^{\text{true}}) R(E_T^{\text{true}}, E_T^{\text{meas}}) dE_T^{\text{true}}$$

The function, R, is the jet response function which gives the probability that a jet of E_T^{true} is observed to have E_T^{meas}. The probability that a jet of E_T^{true} appears in the detector depends on the physics.

This analysis considers events with two jets. The above expression becomes impossible to solve due to the fact that to describe the events requires 6 variables. Trying to parameterize the probability of producing two jets as a function of 6 variables as a function of a limited number of parameters is not possible. The above expression is simplified by assuming a uniform distribution for $\text{PROB}(E_T^{\text{true}})$. Then the probability of observing a jet of E_T^{meas} due to a jet of E_T^{true} is given by the jet response function. Inverting this function gives the method of transforming measured E_T to parton E_T.

The jet response function is determined by simulating the response of the calorimeter to partons of a known E_T. The partons are first fragmented into jets. The model for parton fragmentation into jets is the ISAJET program [30]. The ISAJET program has been tuned to reproduce certain aspects of the CDF data [31].

The detector is simulated using a Monte Carlo technique. The measured single particle response functions are used to generate the calorimeter response

to the particles generated by the fragmentation model. The electron response is determined from the response of the calorimeter to testbeam electrons. The single pion response function at high energy is determined using testbeam pions. The single particle response is given as a distribution of E/p where p is the measured momentum of the testbeam particles (described in Appendix B). At low energy, the single π response is determined from the calorimeter response to isolated single tracks in minimum bias events. To try to ensure that there is only a single charged pion (and no energy due to neutral mesons) the data are selected to have no energy in any of the electromagnetic towers surrounding the tower pointed at by the track. Figure 4.18 shows the single pion response function. The uncertainty on the single particle response is 5%.

The results of the calculation are referred to as the jet response function. The ratio of the number of reconstructed jets to the number of generated partons is the efficiency (shown in figure 4.19). The distribution of measured E_T (for each value of parton E_T) was fit to a functional form which is the convolution of a gaussian with two exponentials (see Appendix C). The exponentials are added to fit the long non-gaussian tails of the measured jet E_T distribution (see figure 4.20). The fit mean is now not sensitive to asymmetric non-gaussian tails. The parton E_T was fitted to the mean of the measured jet E_T distribution using the method of cubic splines[32]. This function is then used to correct the measured E_T of the jets in the data to an assumed correct parton E_T (figure 4.21).

Figure 4.22 shows $\frac{\sigma}{E_T^{\text{meas}}}$ as a function of parton E_T. This is the jet energy

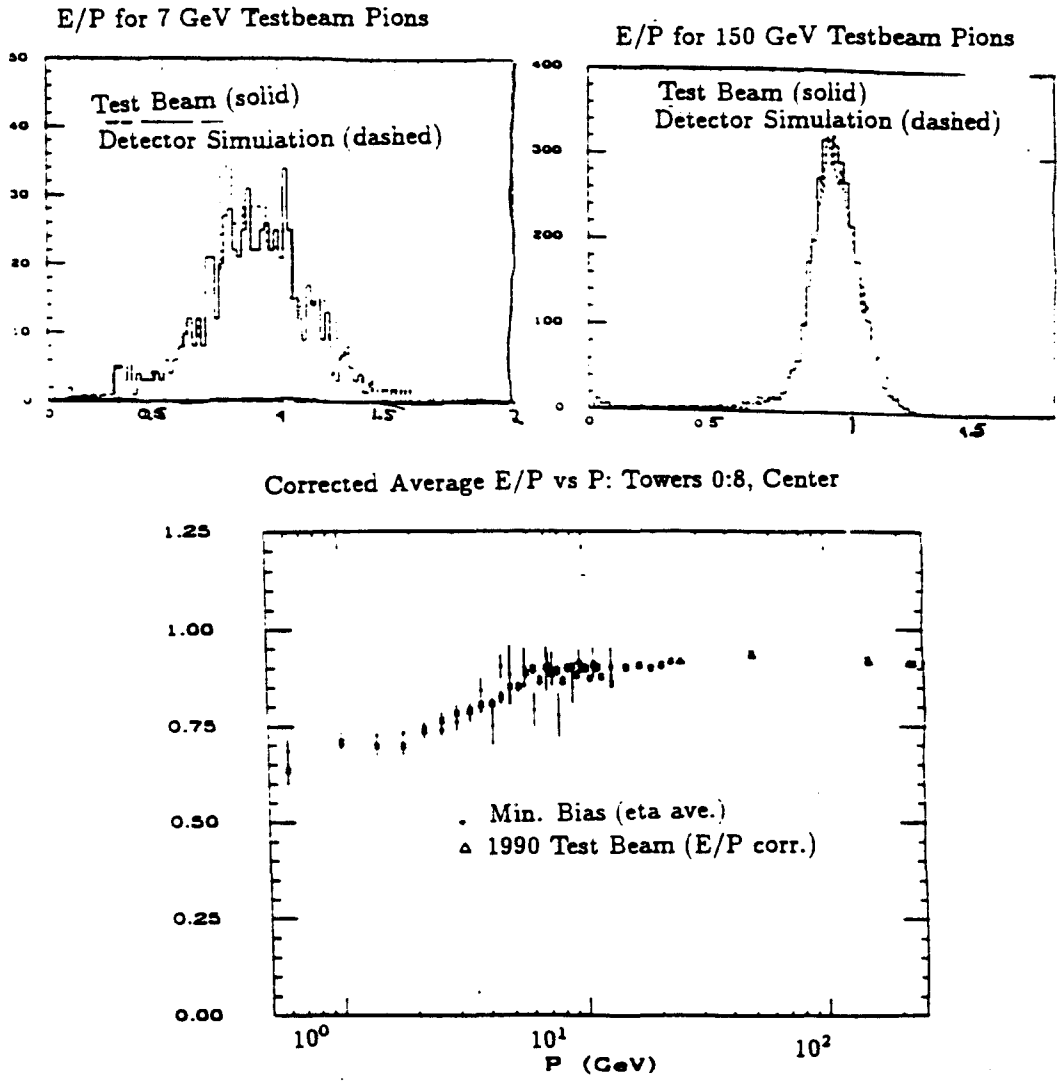

Figure 4.18: Single pion response function measured in using both testbeam pions and isolated single tracks in minimum bias events. QFL refers to the detector simulation program.

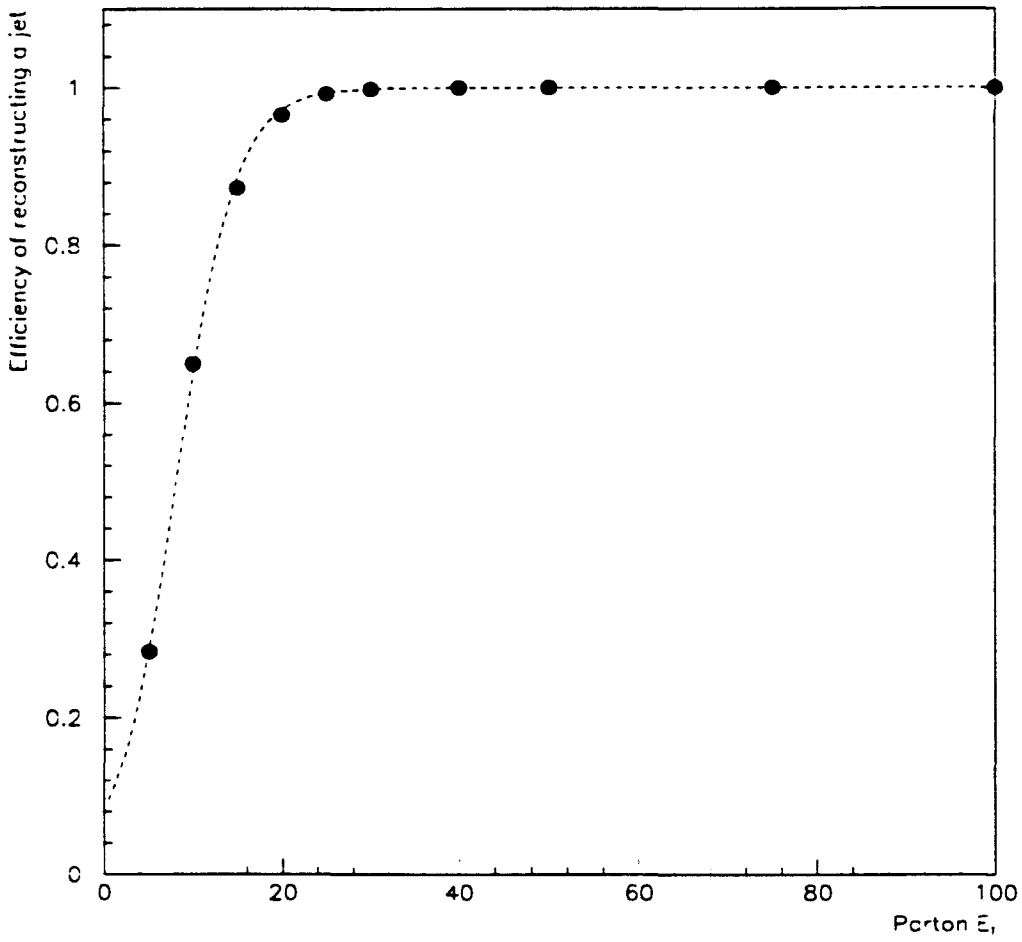

Figure 4.19: Efficiency of finding a jet due to a parton as a function of parton E_T.

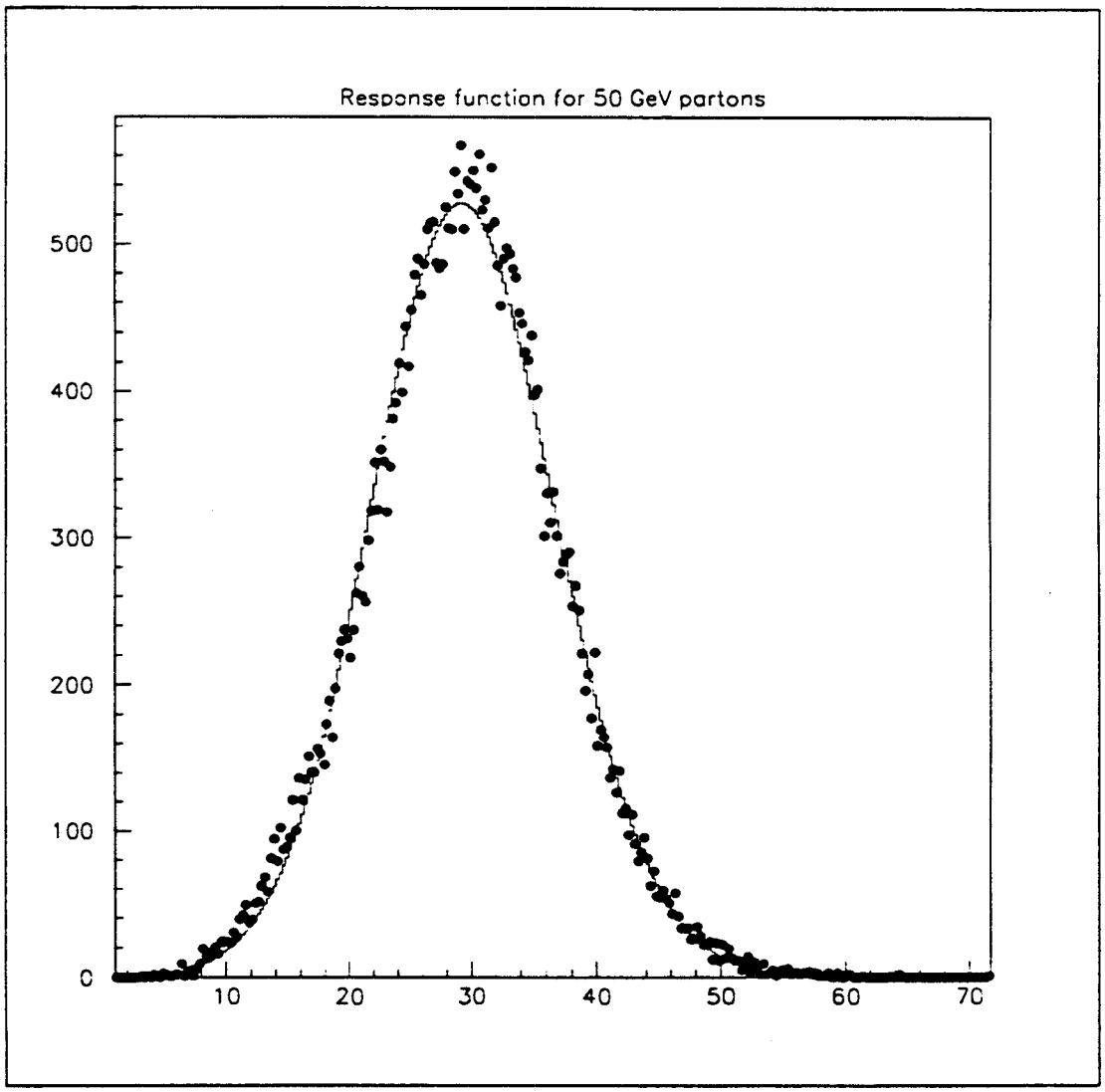

Figure 4.20: Response function for 50 GeV partons. The solid dots are the result of the calculation. The line is the result of the fit performed using a negative log-likelihood estimator (see Appendix C).

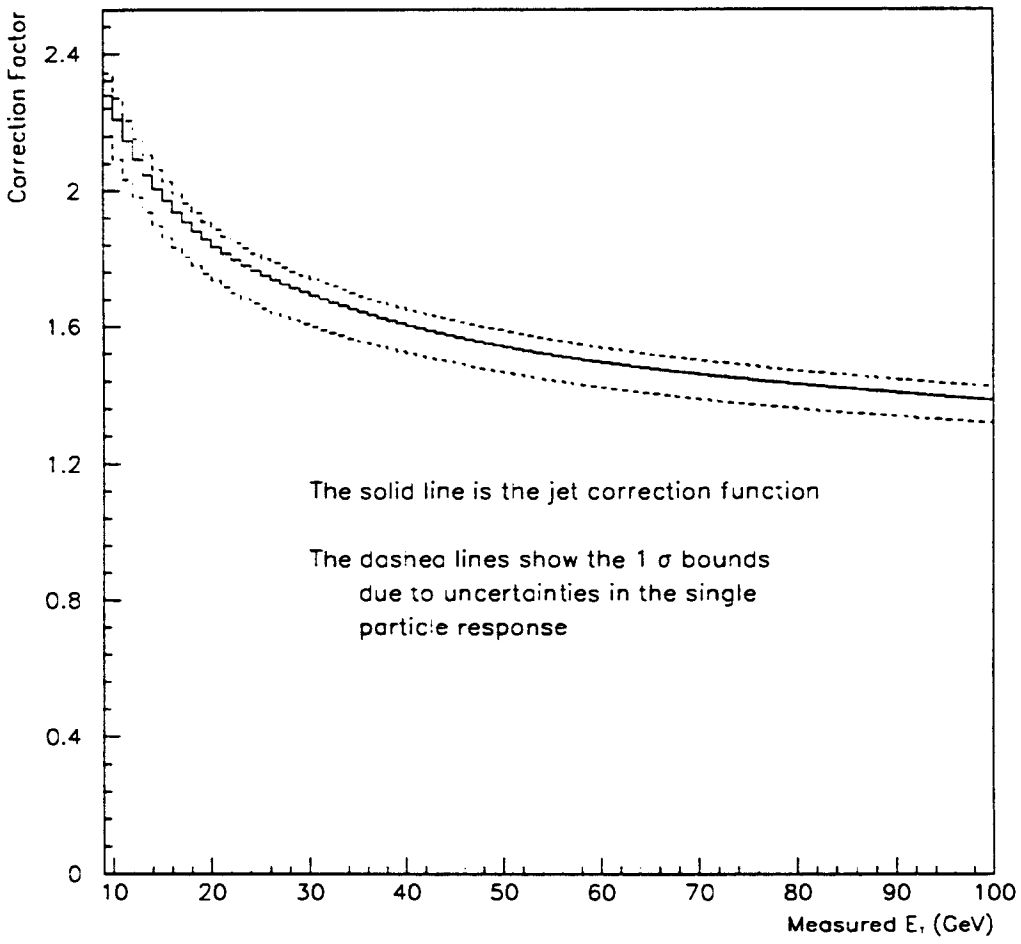

Figure 4.21: Ratio of parton E_T to the mean measured E_T plotted as a function of measured E_T.

resolution. Because the resolution is typically 30%, it is possible to misidentify which jet is the more energetic jet (Jet 1 or Leading Jet) and which jet is the less energetic jet (Jet 2 or Second Jet). To correct for effects due to misidentification, the jet response functions are implemented in a Monte Carlo procedure which smears the theoretical calculation. The distributions used to characterize the topology of the events will be corrected using the difference between the true theoretical distribution and the smeared theoretical distribution.

Both jets are required to have $|\eta| < 2.0$. This avoids the the crack between the plug and forward calorimeter which requires a large correction. Only those events where the second jet E_T is greater than 20 GeV are kept to guarantee that the jet finding algorithm is fully efficient. The final event sample consists of 799 events. Performing the background subtraction leaves 563 ± 60 single photons.

The results of the selection process are given in table 4.3. The numbers show the number of events remaining after each requirement is made.

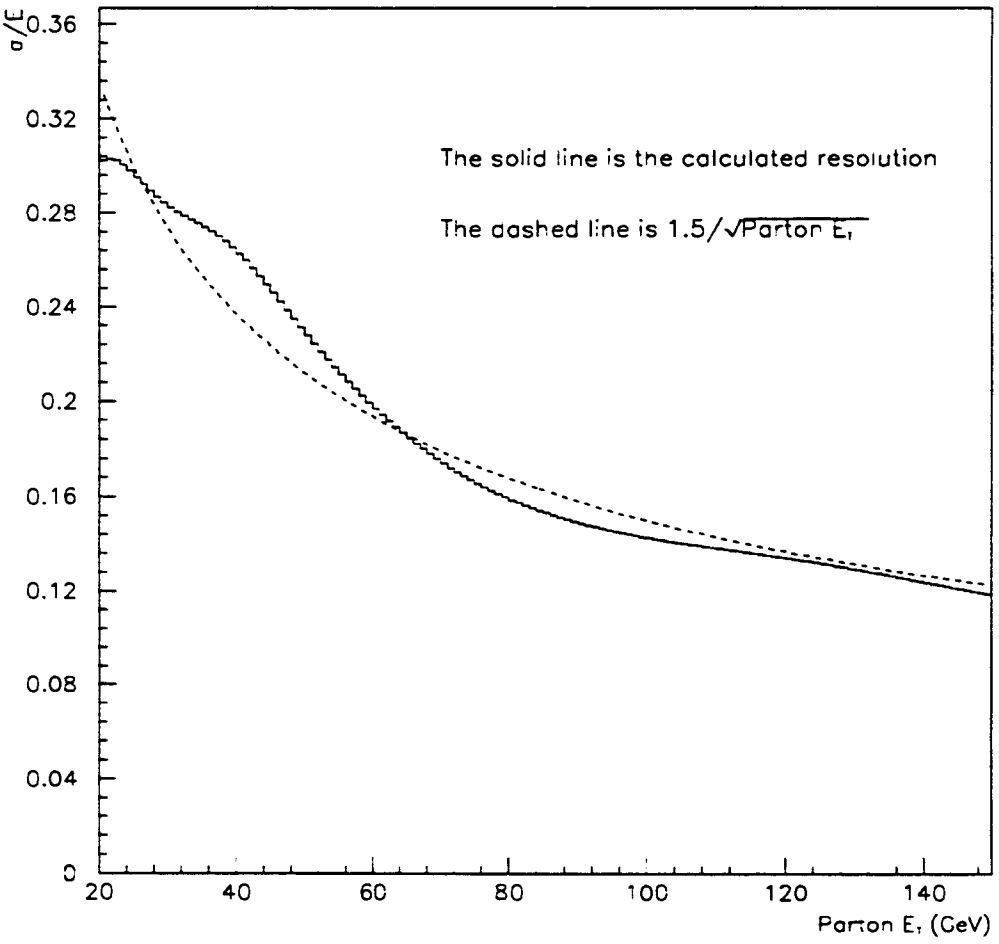

Figure 4.22: Jet energy resolution as a function of parton E_T determined by the jet response function calculation.

Details of Photon Candidate Selection	
Requirement	Number which passed this requirement
All photon 23 GeV Trigger with Photon candidates	
0 tracks	50876
≥ 1 Strip cluster	48065
≥ 1 Wire cluster	47986
Second Strip Cluster ≤ 1 GeV	34712
Second Wire Cluster ≤ 1 GeV	28229
$14.0 < \lvert Z^{\mathrm{strip}} \rvert < 217.0$	25261
$\lvert X^{\mathrm{wire}} \rvert < 17.5$	19403
$I < 0.15$ (in a cone of $\Delta R = 0.4$)	18020
$L_{\mathrm{share}} < 0.200$	17154
$\widetilde{\chi}^2 < 20.0$	16232
$25.0 < E_T^{\gamma} < 54.0$	11339
Number of events with a photon candidate	11334
$\not\!\!E_T < 3.0\sigma_{\not\!\!E_T}$	10754
$\lvert Z_{\mathrm{vertex}} \rvert < 60.0$	10315
$I < 0.05$	7090
Number of events with 2 jets with $E_T > 20.0$ and $\lvert\eta\rvert < 2.0$	799
Number of photons	**563**

Table 4.3: Details of the photon + 2 jet selection process. The criteria were applied in the sequence given.

Chapter 5

Analysis

The theoretical calculation of the cross-section contains several poles which are not observed in the final state. These coincide to regions where the $2 \rightarrow 3$ processes are observed as $2 \rightarrow 2$ processes. For the calculation of the inclusive direct photon cross section, these terms are absorbed into the two body final state. To restrict the calculation to the region of phase space where the calculation is finite, the invariant mass of the photon and leading jet is required to be less than 95% of the event invariant mass. This excludes the pole due to soft gluon radiation in both the initial and final state. The invariant mass of any pair of final state particles has to be greater than 0.1% of the event invariant mass to remove the poles due to collinear singularities. Lastly the momentum transfer between either of the initial state partons and any of the final state particles has to be greater than 0.1%. This is to remove the singularities when one of the final

state particles is collinear with the beam.

Each sampling of the three body phase space permits the calculation of the energy and momentum of the final state particles. The following requirements are made which mimic the requirements placed on the data:

- $25.0\text{GeV} < E_T^\gamma < 54.0$ GeV
- $|\eta^\gamma| < 0.9$
- $20.0\text{GeV} < E_T^{\text{parton}}$
- $|\eta^{\text{parton}}| < 2.0$
- minimum separation of any pair > 0.8

To illustrate the effect of the selection procedure on the available phase space, figure 5.1 shows the distribution of the generated events as a function of the fraction of the center of mass energy carried by the photon and the fraction of the center-of-mass energy carried by the second jet. To demonstrate that the data is not sensitive to the singular regions, figure 5.2 shows the phase space rejected by the final state collinearity cut, figure 5.3 shows the phase space rejected by the soft cut. Figure 5.4 shows the phase space distribution of events rejected by the beam collinearity cut. These events are uniform over the entire phase space. However figure 5.5 shows the distribution as a function of the photon pseudorapidity and the larger absolute pseudorapidity of the two jets. From figure 5.5 it is clear that these events are not observed.

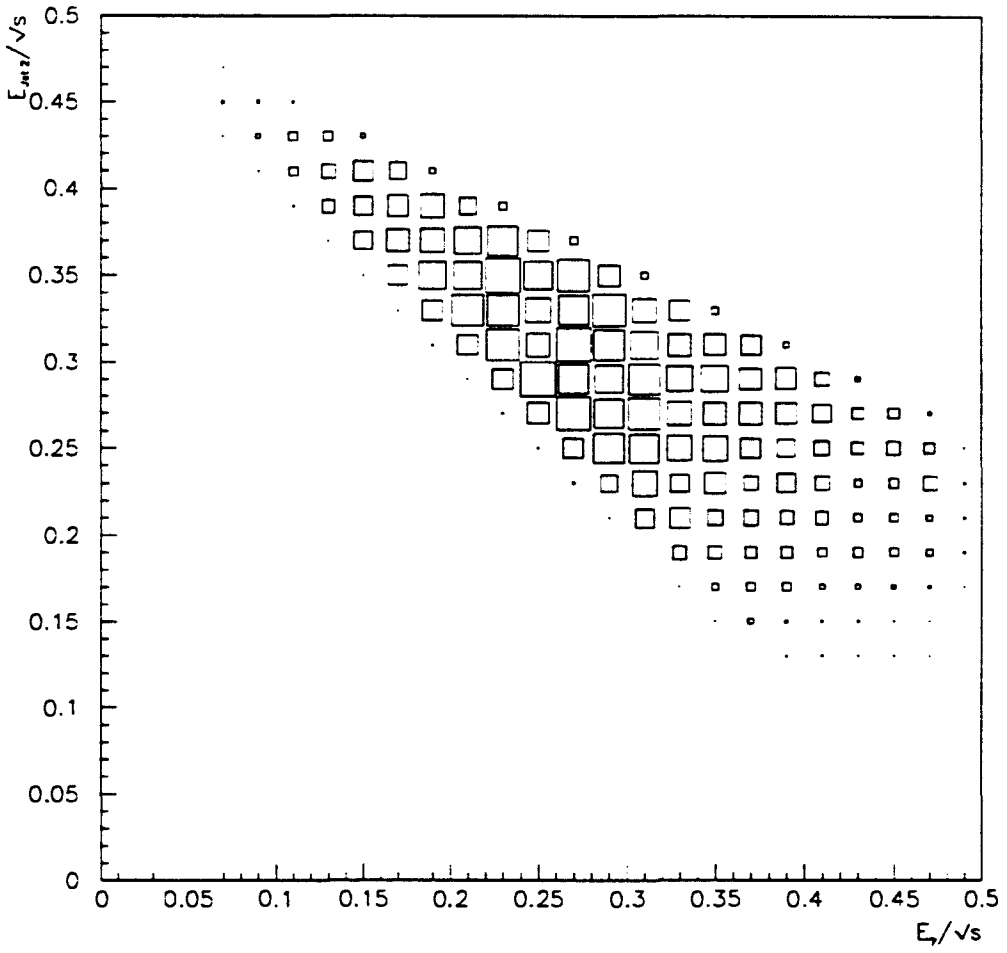

Figure 5.1: Phase space accepted by the requirements made on the data. The size of the boxes is proportional to the cross section for that element of phase space.

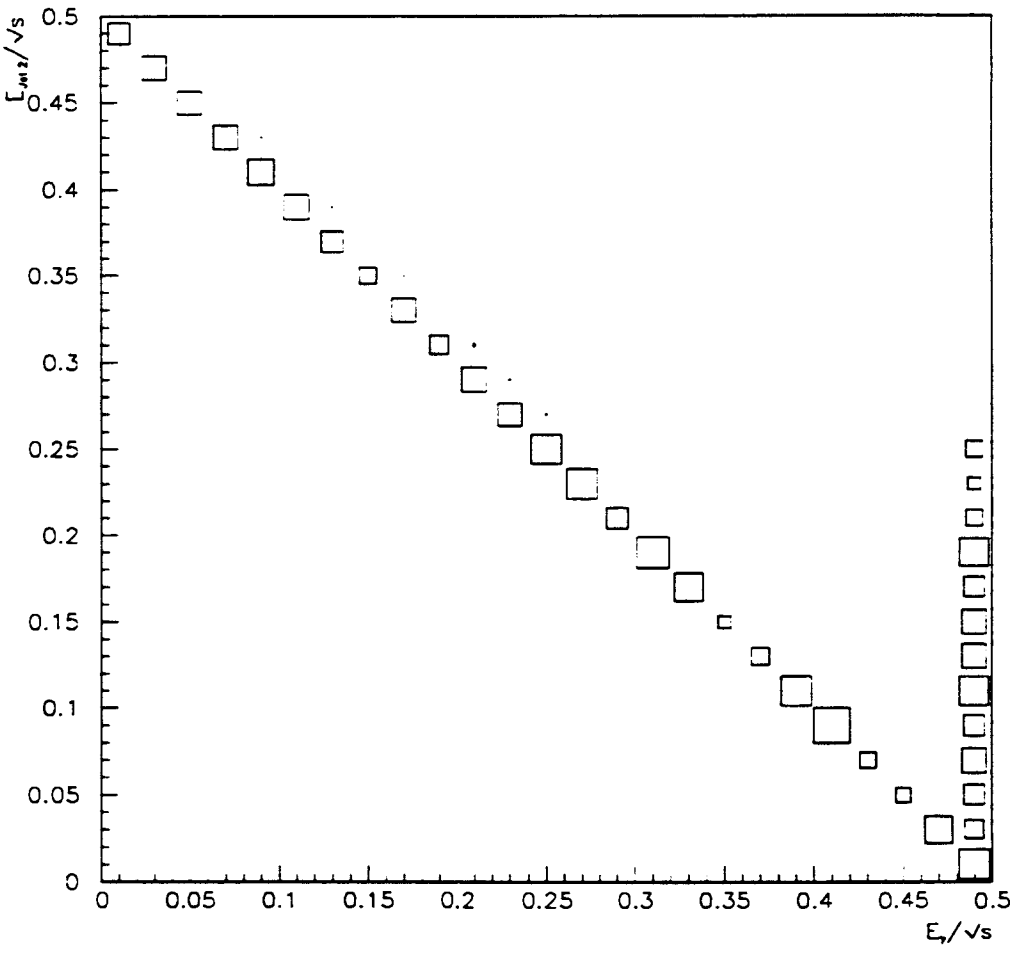

Figure 5.2: Phase space rejected by the requirement that none of the final state particles be collinear.

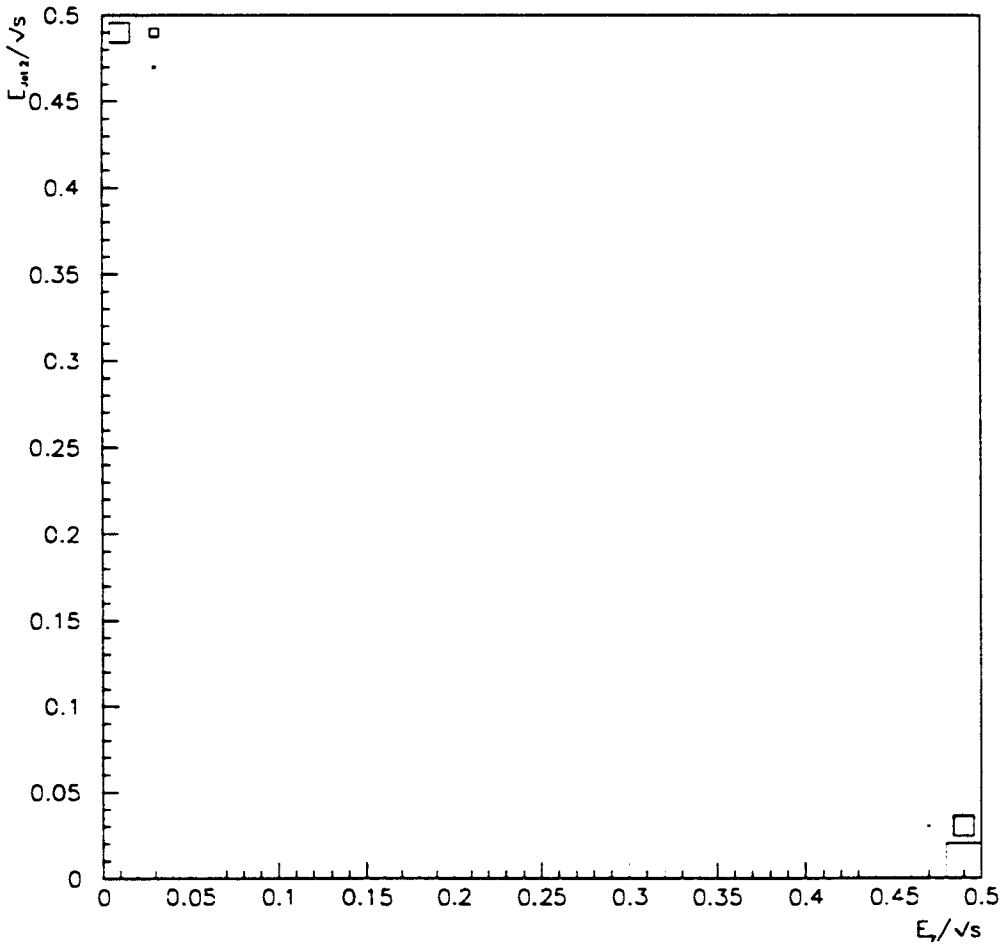

Figure 5.3: Phase space rejected by the requirement that none of the final state particles be soft.

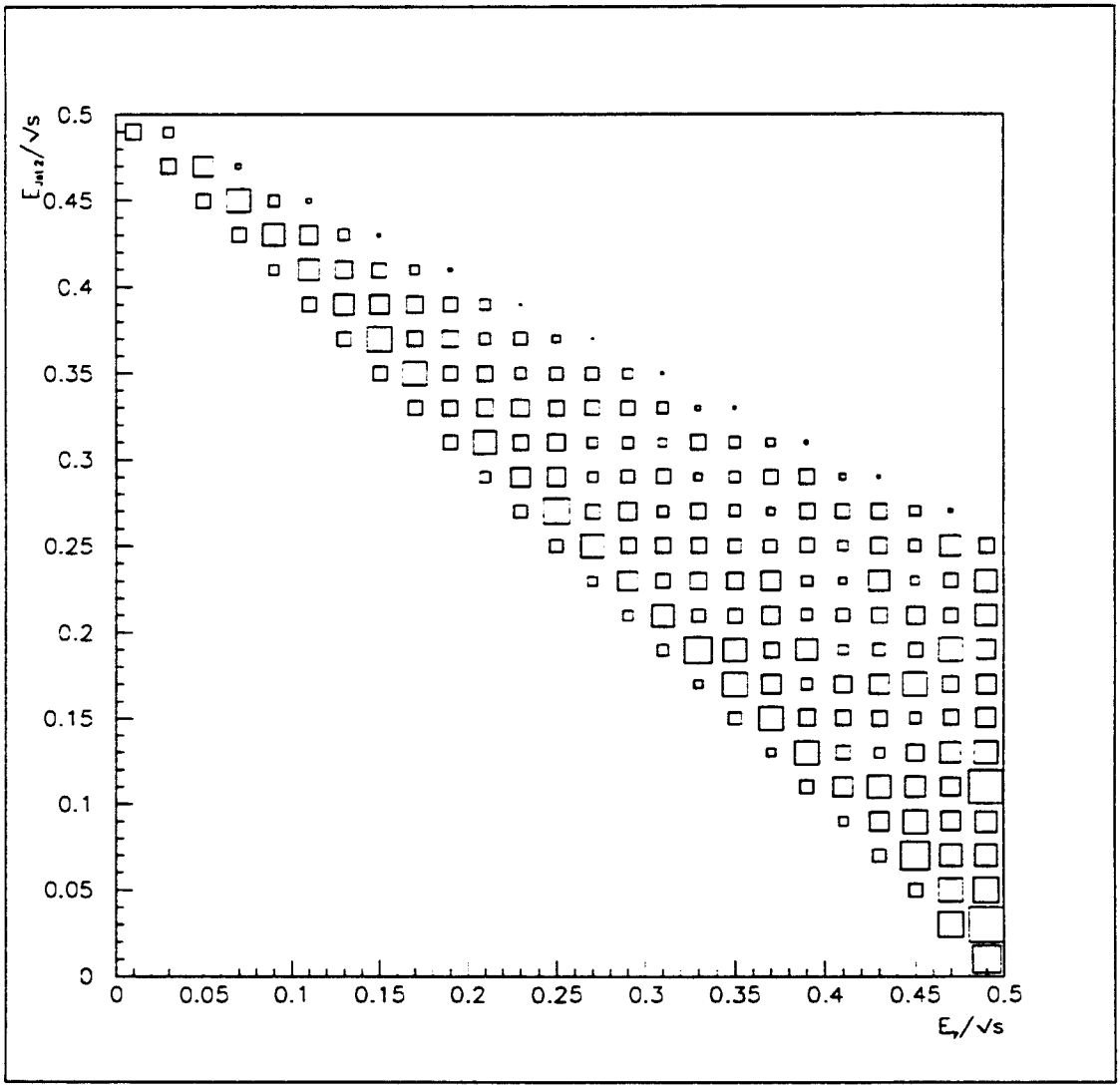

Figure 5.4: Phase space rejected by the requirement that none of the final state particles be collinear with the beam.

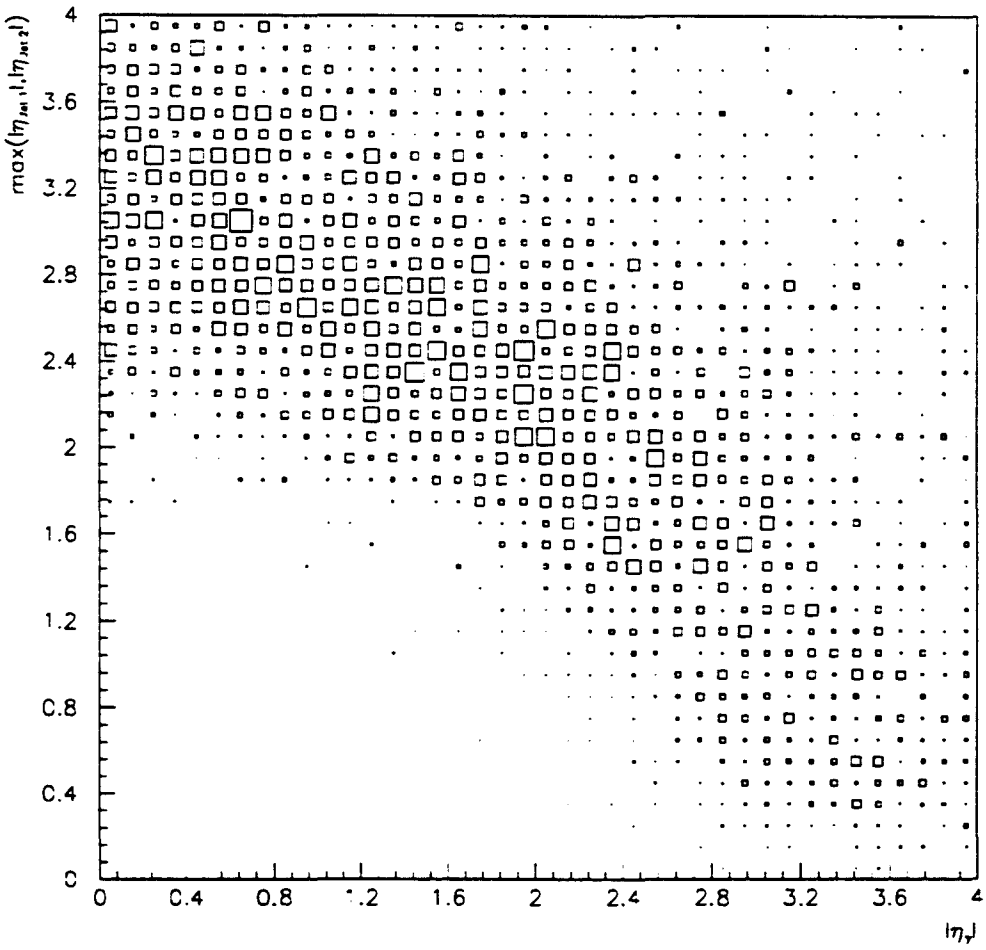

Figure 5.5: Phase space rejected by the requirement that none of the final state particles be collinear with the beam. This region is shown by plotting the number of events as a function of the pseudorapidity of the photon, and the larger absolute pseudorapidity of the two jets.

The ideal analysis would involve studying the topology of the events in the center-of-mass frame. This is not possible due to the limited statistics of the data, and the poor jet energy resolution. To circumvent this limitation, this analysis uses the separation of the photon and the jets in $\eta - \phi$ space defined by:

$$S = \Delta\eta \ominus \Delta\phi \tag{5.1}$$

This variable has the advantage that it is used explicitly in the definition of photon candidates and jets. It is also a Lorentz invariant if there is no net momentum transverse to the beam in the laboratory frame.

5.1 The Cross Section Measurement

To calculate the cross-section, one needs to know the number of events containing isolated prompt photons, the acceptance of the criteria used to select the events, and the integrated luminosity of the data sample. The trigger efficiency, and other acceptance factors were detailed in 4.2.1. Using these values, the cross section for producing a photon and two jets subject to the requirements given in Chapter 4 is given by

$$\sigma = \frac{1}{\int \mathcal{L}dt} \sum_{\gamma \text{ candidates}} \frac{w_S}{\alpha(E_T^\gamma)} \tag{5.2}$$

where $\int \mathcal{L}dt$ is the total integrated luminosity, w_S is the weight as determined by equation 4.15, and $\alpha(E_T^\gamma)$ is the product of the acceptances and efficiencies.

The total integrated luminosity is calculated from the following formulas:

$$\int \mathcal{L}dt = \frac{N_{\rm BBC}}{\sigma_{\rm BBC}} \tag{5.3}$$

$$\sigma_{\rm BBC} = (1 - \frac{\sigma_{el}}{\sigma_T})\sigma_T \epsilon_{DA} \tag{5.4}$$

where $\sigma_{\rm BBC}$ is the measured Level 0 cross section, $N_{\rm BBC}$ is the number of level 0 triggers recorded during the entire data collection period, σ_{el} is the elastic cross-section not seen by the trigger, σ_T is the total cross-section, and ϵ_{DA} is the geometric acceptance of the Level 0 trigger. The total integrated luminosity is 3623 $\rm nb^{-1}$ [33].

The product of the trigger efficiency and the various other acceptance factors is shown in figure 5.6. Summing over the entire sample results in

$$\sigma(p\bar{p} \rightarrow \gamma + 2\text{Jets}) = 369.2 \pm 42.1 \text{ picobarns} \tag{5.5}$$

where the uncertainty is statistical only.

The theoretical calculation gives:

$$\sigma(p\bar{p} \rightarrow \gamma + 2\text{Jets}) = 159.4 \text{ picobarns} \tag{5.6}$$

As stated in Chapter 2, varying the scale by a factor 2 results in a 40% uncertainty on the cross section.

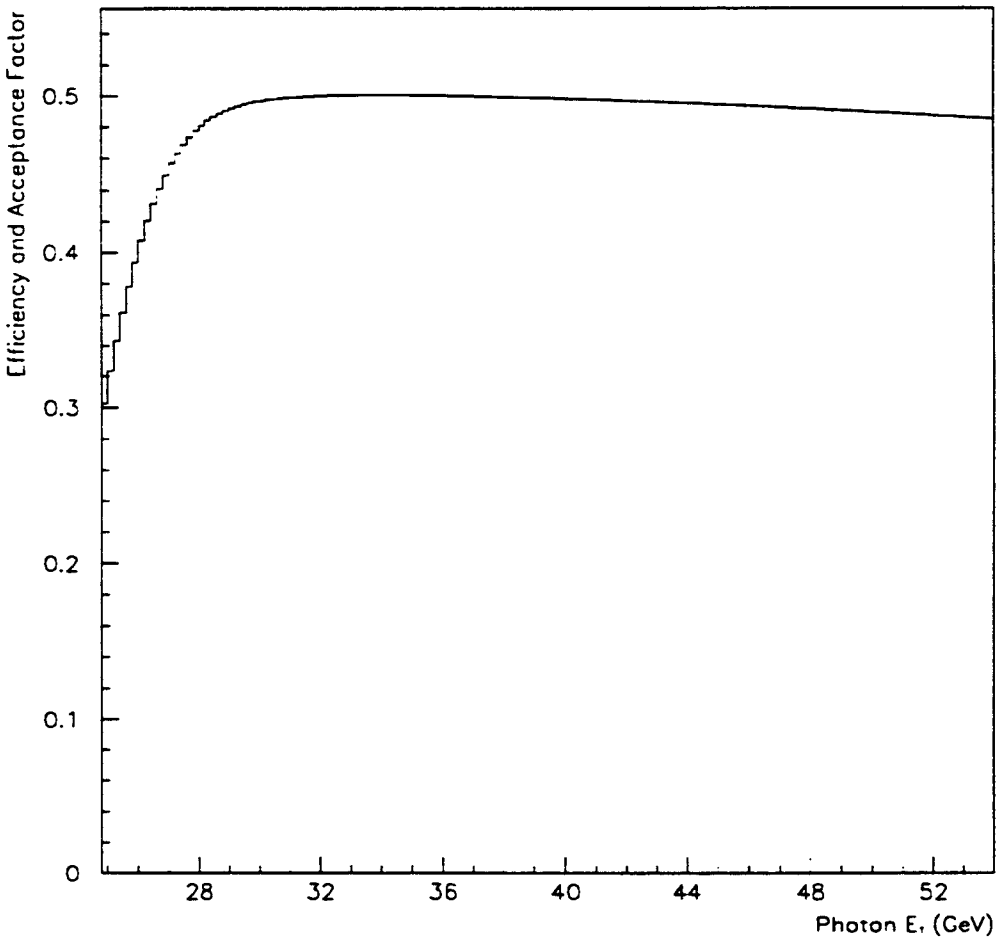

Figure 5.6: The product of various efficiencies and acceptances used to correct the data plotted as a function of photon E_T.

5.2 The E_T Spectra for the Photon and the Two Jets

The cross-section is also calculated as a function of the photon E_T, the leading jet E_T and the second jet E_T. The spectrum is determined by integrating over each bin and dividing by the bin width. The resulting distribution is not a true differential distribution but both the data and the theoretical calculation were handled in the same manner. The theoretical prediction was renormalized to give the same total cross-section as the data to facilitate comparisons of the shape of the distribution.

The photon E_T spectrum is given in figure 5.7. Shown for comparison are the results of the theoretical calculation and the results of the phase space calculation. The phase space calculation is harder (that is there are more photons with larger E_T) than both the data and the QCD calculation. The reason is that photon Bremsstrahlung from quark lines results in a softer photon E_T sepectrum. Figure 5.7 demonstrates the presence of Bremsstrahlung. The error bars on the data include both statistic and systematic uncertainties. The large statisitical uncertainties are due to the background subtraction. The systematic uncertainties will be described in Chapter 6.

Figure 5.8 gives the leading jet spectrum. The data agrees with both the QCD calculation and the phase space calculation. The reason is that by ordering the jets in energy biases the spectrum. Furthermore, the shape of the invariant

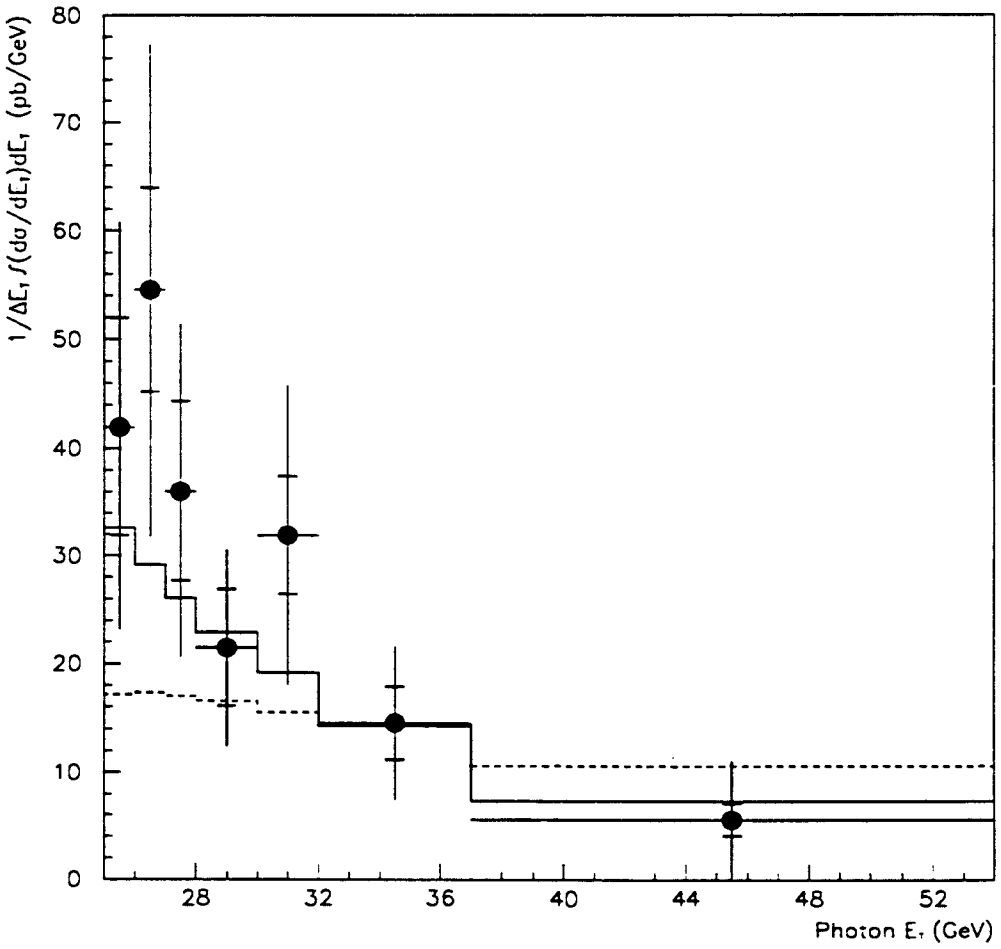

Figure 5.7: The measured photon E_T spectrum compared to the QCD calculation (solid line) and the phase space calculation (dashed line).

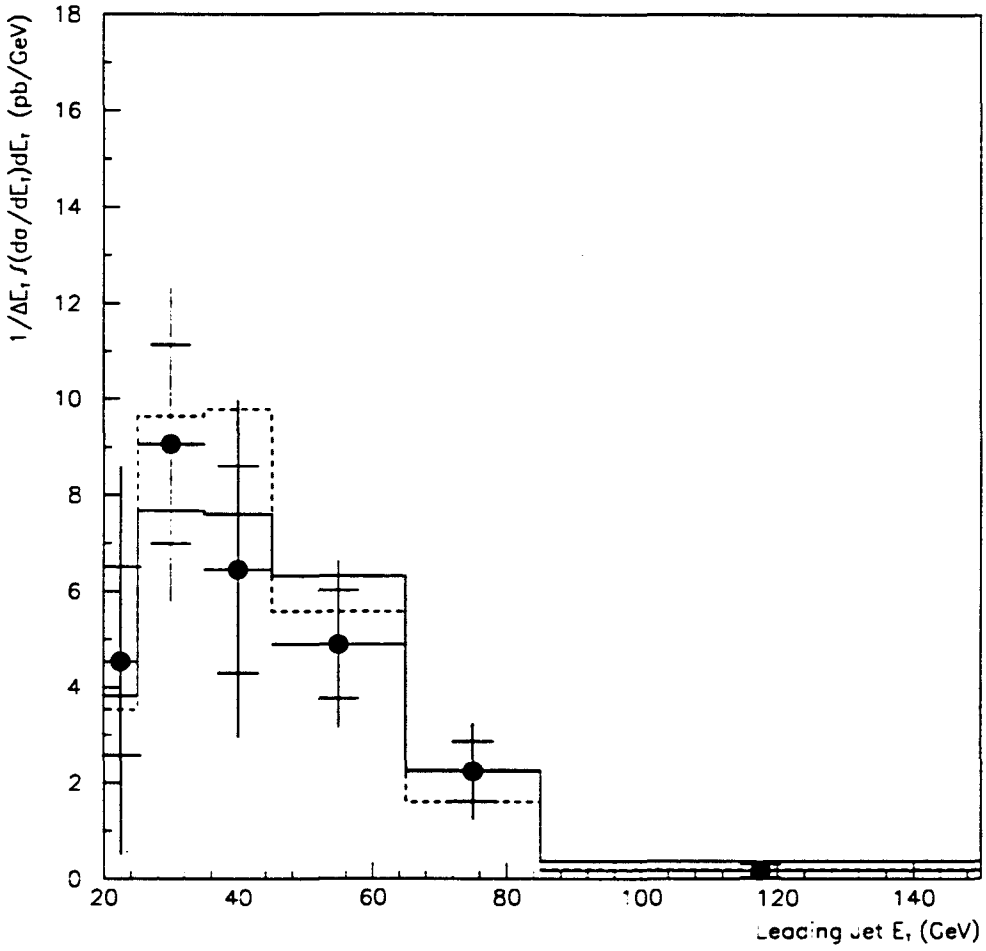

Figure 5.8: The measured leading jet E_T spectrum compared to the QCD calculation (solid line) and the phase space calculation (dashed line).

mass distribution is determined by the E_T requirements on the photon and the jets, and by the parton luminosity shown in figure 2.1. This distribution does probe our knowledge of the parton distribution functions, and is consistent with the current estimates.

Lastly, figure 5.9 shows the second jet E_T spectrum. This distribution is steeply falling as a function of E_T due to the energy ordering of the jets, and the parton luminosity. Because most of the events have second jet with an E_T close to 20 GeV, it is hard to accurately measure the spectrum. Again this spectrum is mostly a check of the parton luminosity.

Naively, one would expect the phase space calculation of the photon E_T to be steeply falling as a function of E_T for the same reason. This is not noticeable because the E_T requirements placed on the photon exclude the region where the photon E_T spectrum falls sharply due to the parton distribution functions.

5.3 Topology of the Events

The separation has been defined by equation 5.1. Figure 5.10 gives the separation distribution for the photon and the leading jet. Also shown are the results of the QCD calculation and the phase space calculation. All three distributions are biased by the energy ordering of the jets. This is visible in the data, the QCD calculation and the phase space calculation where there are no events with a separation less than 2.0. The phase space distribution peaks at a separation of

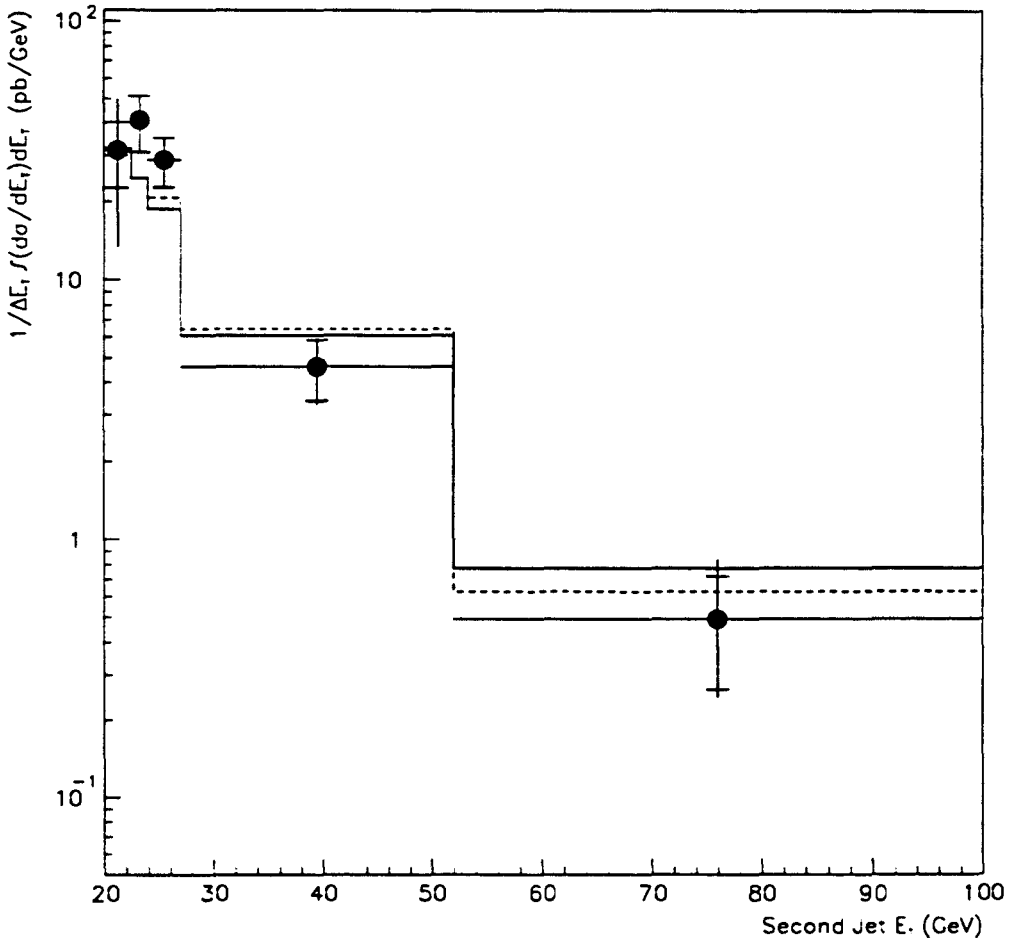

Figure 5.9: The measured second jet E_T spectrum compared to the QCD calculation (solid line) and the phase space calculation (dashed line).

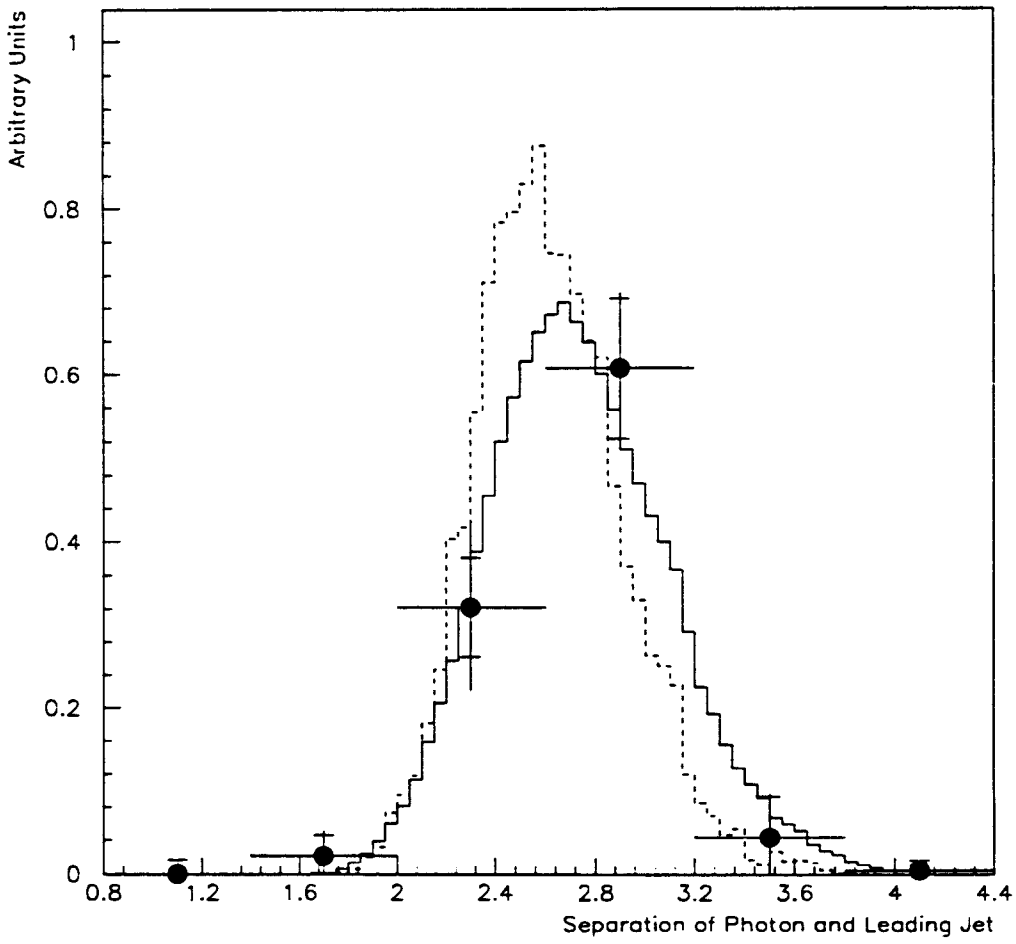

Figure 5.10: Separation of the photon and the leading jet compared to the QCD calculation (solid line) and the phase space calculation (dashed line).

2.5 because a uniform phase space distribution favors an equal partitioning of the energy, hence the mean separation is slightly above $\frac{2\pi}{3} = 2.1$. The QCD calculation peaks at a separation of 2.8. Consider a $2 \rightarrow 2$ process. The two bodies will have $\Delta\phi = \pi$ and $\Delta\eta$ will be determined by the production process. If one of the two particles radiates a third particle, $\Delta\phi$ will decrease, and $\Delta\eta$ will on average remain the same. In figure 5.10 the parton which forms the second jet radiates the photon. Since a radiative process will tend to cluster events at the minimum $\gamma -$ Jet2 separation, one would expect a mean separation of $\pi - 0.4 = 2.74$. Larger separations are due to events produced at small angles with respect to the beam.

Figure 5.11 shows the phase space distribution of the QCD events for each bin of separation. Beginning with the upper left hand plot, there are no events with which satisfy $0.8 < S(\gamma, \text{Jet1}) < 1.4$ because it is not possible to conserve energy with the photon parallel to the more energetic jet. As the angle between the photon and Jet 1 is increased, events first appear near the maximum Jet 2 energy, and then gradually fill up the available phase space, ending up in the lower right hand plot at the largest separation with the lowest Jet 2 energies. In this case the photon and Jet 2 are collinear.

The QCD calculation gives more events at large separation because the matrix elements include terms proportional to $\frac{1}{\sin^2\frac{\theta}{2}}$ and $\frac{1}{\sin^4\frac{\theta}{2}}$. Figure 5.12 shows the distribution in $\cos\theta$ for each bin of the separation of the photon and the leading jet.

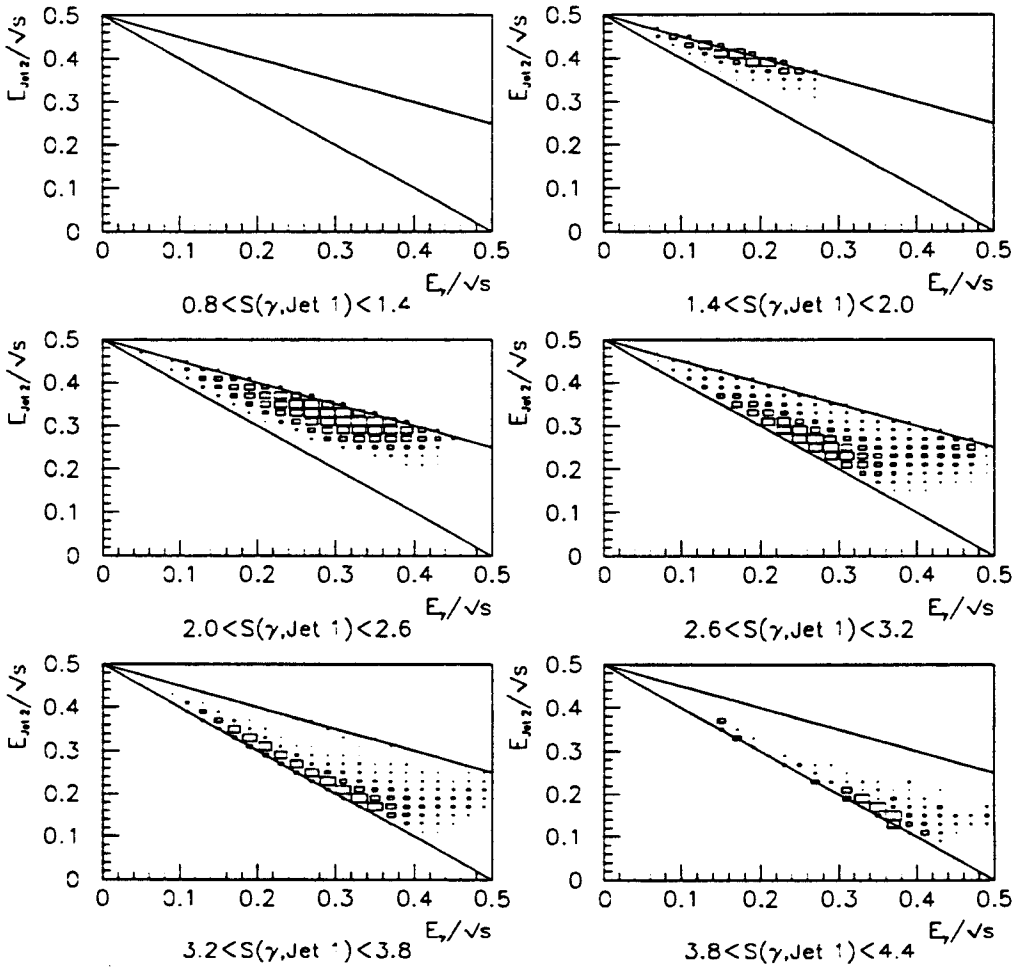

Figure 5.11: The phase space as defined in the text for each bin in separation (S) for the photon and the leading jet. The size of each box is proportional to the bin contents.

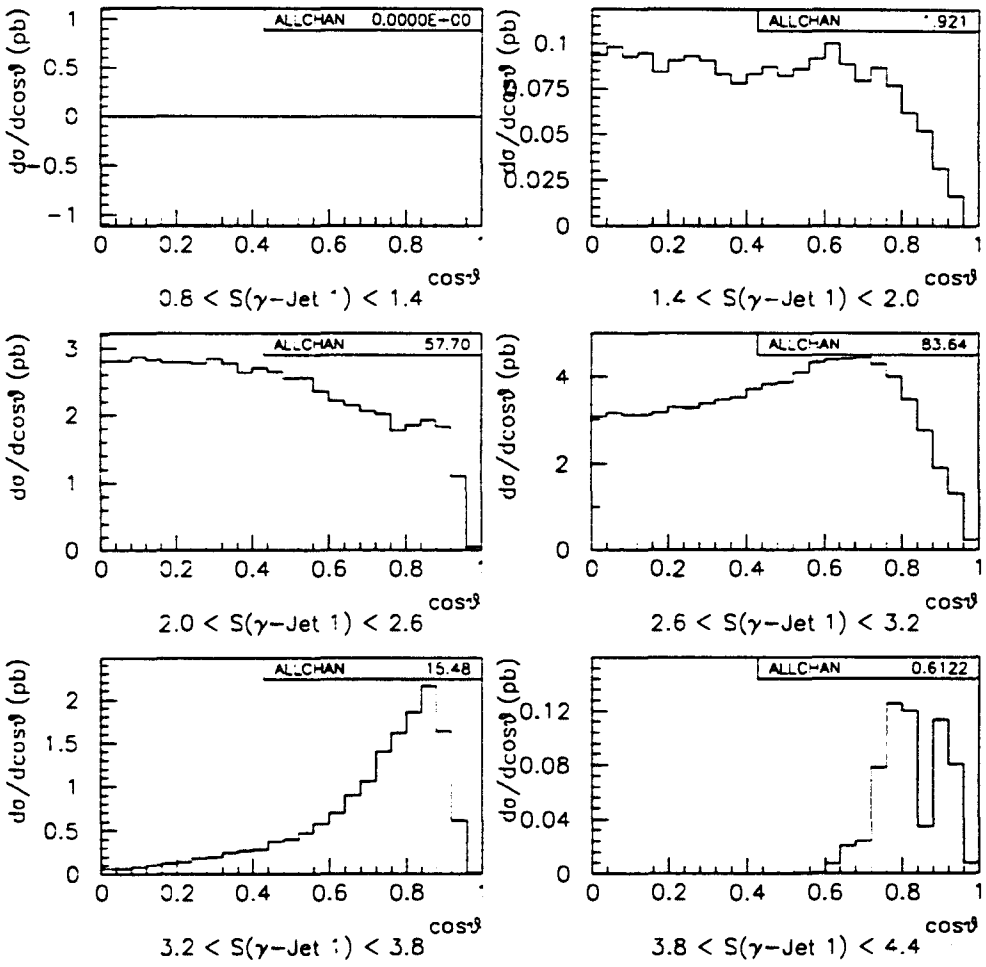

Figure 5.12: $\cos\theta$ distribution for different bins of the [g]-jet 1 separation. θ is the angle of the leading particle (either the photon or jet 1) with respect to the beam in the center-of-mass. The double peak in the last bin shows the effect of the extended η range for the jets.

The separation of the photon and the second jet is shown in figure 5.13. The QCD calculation peaks at small separation due to Bremsstrahlung from final state quarks. The peak at 2.1 is due to gluon radiation near Jet 1. The reason that the peak is at 2.1 and not at 2.74 is that Jet 2 is less energetic than Jet 1, hence it has to be at a smaller angle with respect to the photon to conserve momentum. The phase space calculation peaks at 2.2. The data is consistent with being flat over the range $0.8 - 3.2$ and hence appears more consistent with the QCD calculation than the phase space calculation.

The phase space distribution of the QCD calculation for each bin is shown in figure 5.14. All events in the upper left hand plot are events where the photon and Jet 2 are collinear. Progressing to larger separation, the events move away from this boundary. The middle left hand plot shows that events with $2.0 < S(\gamma, \mathrm{Jet2}) < 2.6$ are of the Mercedes Benz type. The last three bins of separation probe the region where the two jets are collinear with Jet 2 becoming softer with increasing separation between it and the photon. In this region the acceptance becomes small due to the lower limit on the jet E_T and the upper limit on the photon E_T.

The separation of the two jets is shown in figure 5.15. This distribution is similar to the separation of the photon and the second jet in that it probes the collinearity of the two jets. This is evident from figure 5.16. Each bin in separation successively further from the region where the two jets are collinear. Note that the degree of collinearity is 100% correlated to the fraction of the

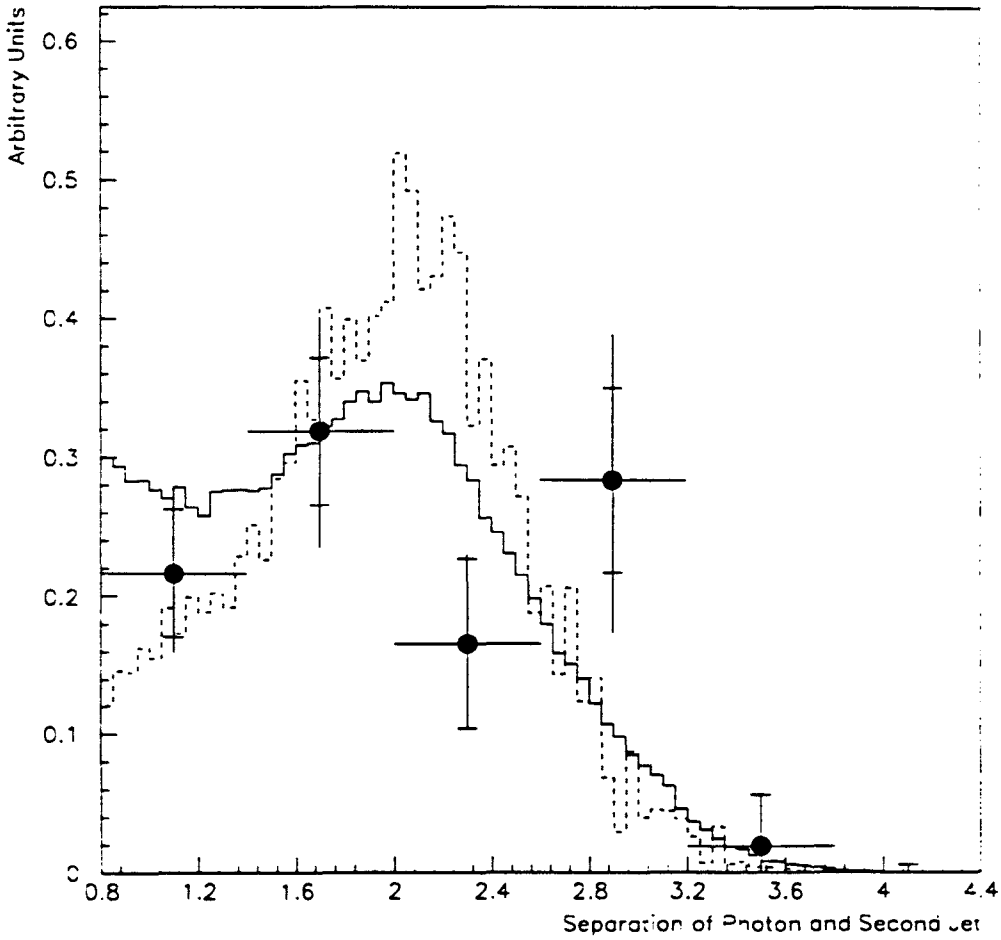

Figure 5.13: Separation of the photon and the second jet compared to the QCD calculation (solid line) and the phase space calculation (dashed line).

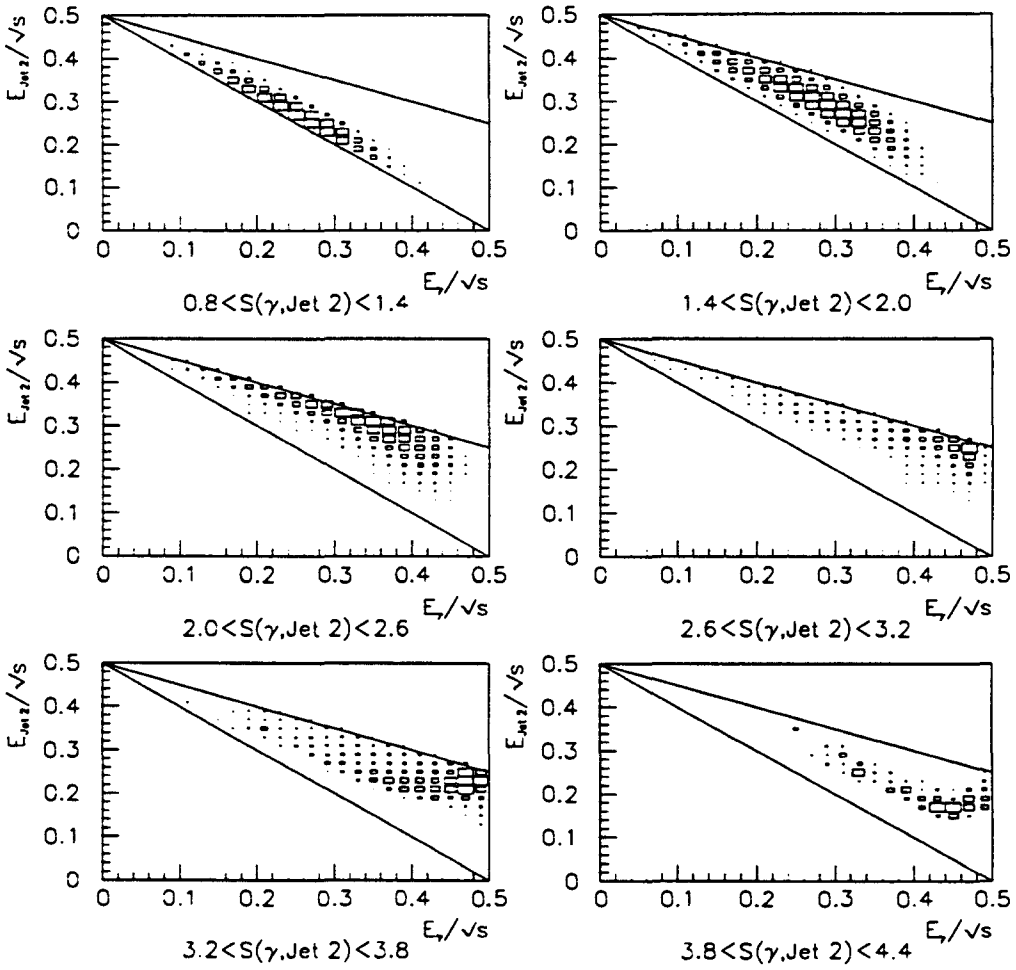

Figure 5.14: The phase space as defined in the text for each bin in separation (S) for the photon and the second jet.

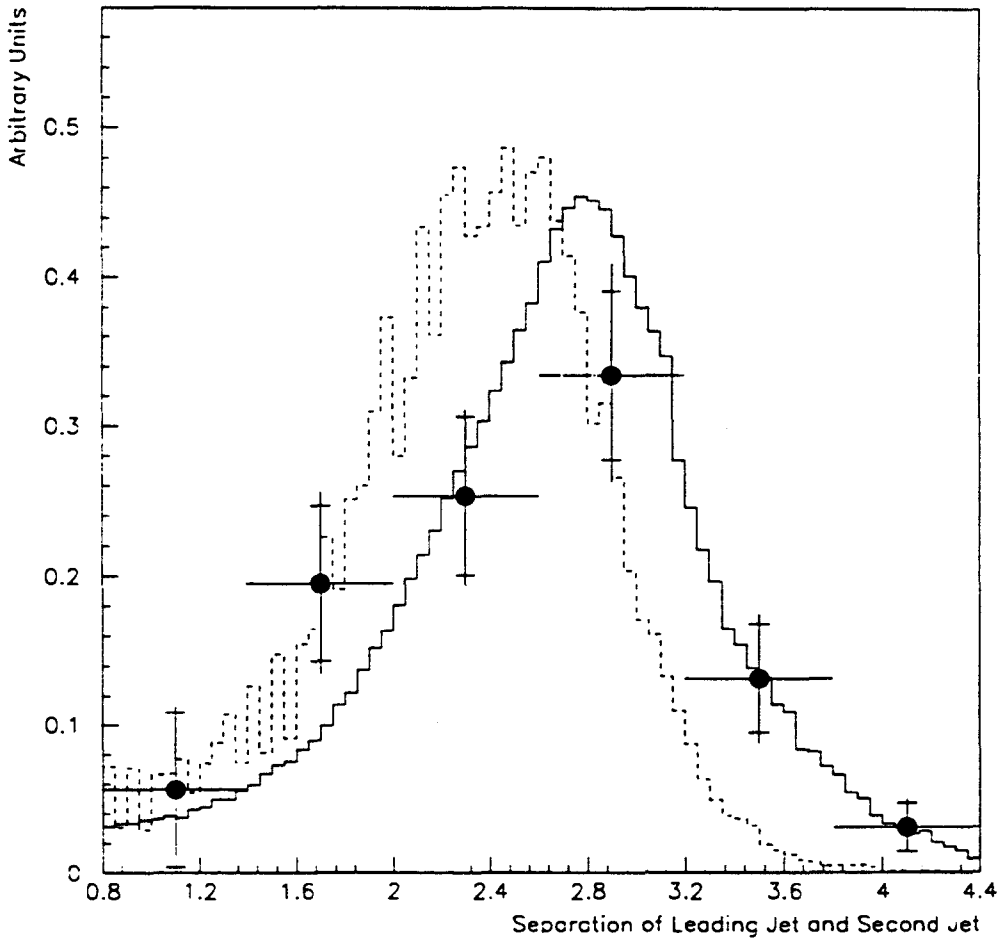

Figure 5.15: Measured separation of the leading jet and the second jet compared to the QCD calculation (solid line) and the phase space calculation (dashed line).

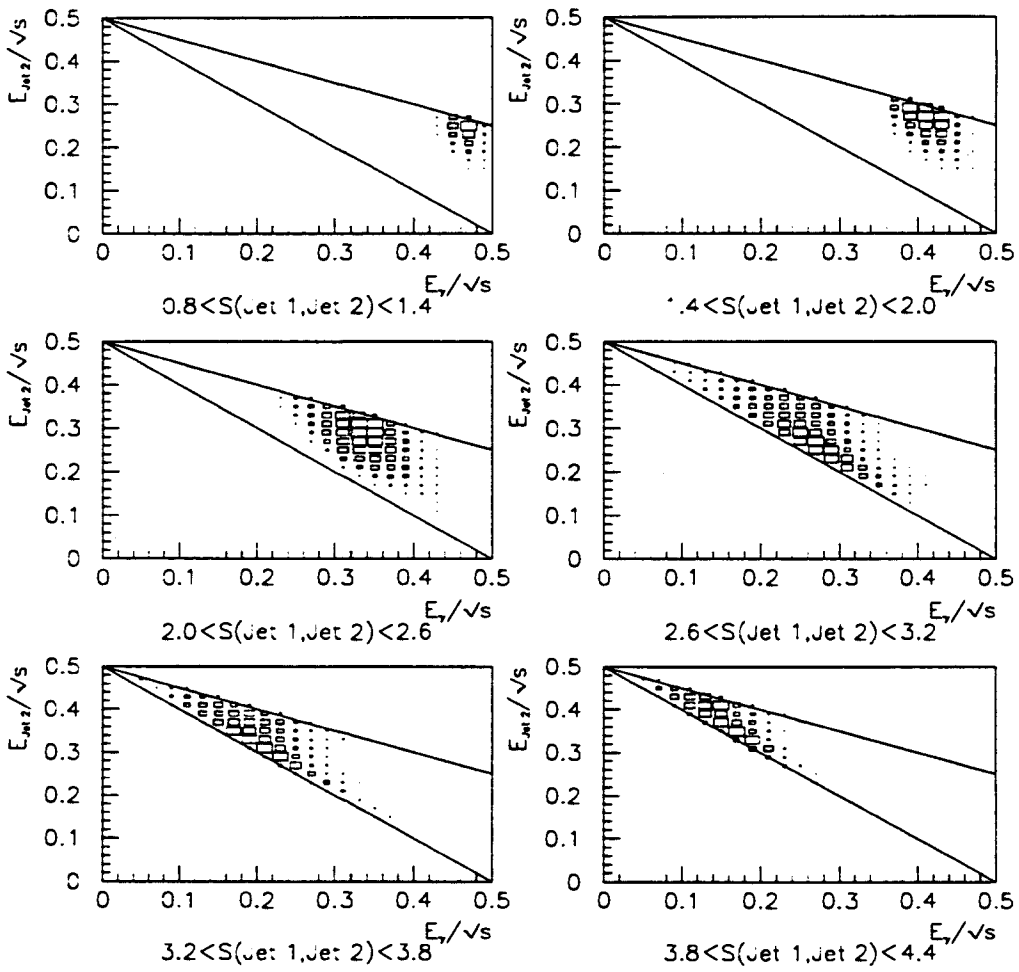

Figure 5.16: The phase space as defined in the text for each bin in separation (S) for the two jets.

available energy carried by the photon. At small separation the photon carries half the available energy. At large separation the photon carries 10% of the available energy. To illustrate this, figure 5.17 shows the distribution for each bin of separation of the fraction of the available energy carried by the photon. The contents of each bin are shown. Most of the events fall into the region where the photon carries a third of the available energy. This is also the region where it is easiest to confuse which is the leading jet in the event.

Figure 5.15 shows that the data favors the QCD calculation. The photon E_T spectrum (figure 5.7) and the separation of the photon and the second jet (figure 5.13) also show that the data favors the QCD calculation. The other distributions are determined more by the effective parton luminosity and the kinematics than the matrix elements and hence are less efficient at distinguishing between the QCD calculation and the phase space calculation.

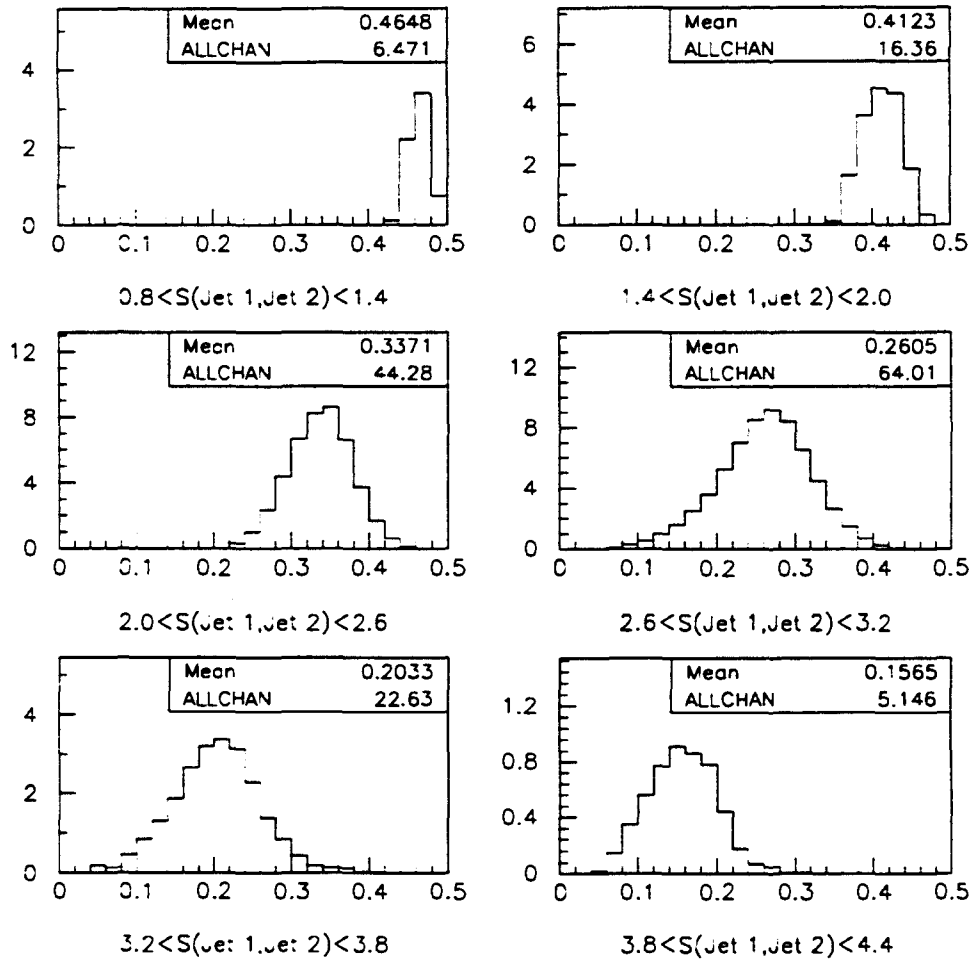

Figure 5.17: Distribution of the fraction of the available energy carried by the photon for different bins of the Jet 1 – Jet 2 separation.

Chapter 6

Systematic Uncertainties

The measurement of the cross section is sensitive to several systematic uncertainties. The dominant contributions are due to the jet energy scale and the photon background subtraction.

6.1 Uncertainties in the Jet Energy Scale

The jet energy scale is determined from a model for parton fragmentation into jets, a simulation of the detector which uses the measured single particle response, and the correction map from dijet balancing. To determine the uncertainty in the model, the distribution of the E_T contained in the region $0.4 < \Delta R < 1.0$ as a function of the E_T of the jet measured in the data as compared to the expectation of the model. Figure 6.1 shows the mean E_T in this region as a function of the measured E_T of the jet. The fragmentation model predicts the

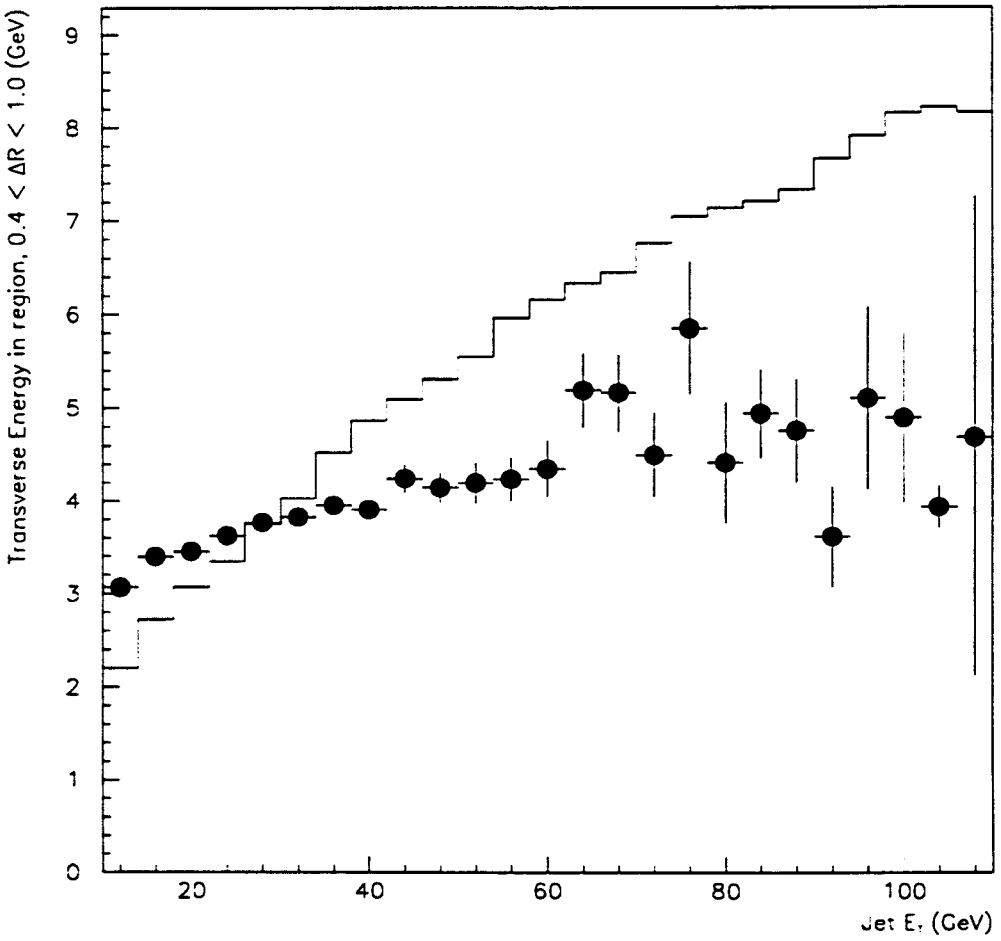

Figure 6.1: Distribution of energy in the annulus of outer radius 1.0 surrounding a jet. The points are the data, and the histogram is the model.

amount of E_T outside the clustering cone to rise linearly with the E_T of the jet. The data could allow for a slight rise with E_T. However the shape of the two distributions are clearly inconsistent. The comparison demonstrates that the phenomenology of fragmentation outside the core of the jet is poorly understood. However since the model is used to calculate the correction for energy lost outside the clustering cone, this difference introduces a systematic error. To account for it, the difference of 1 GeV at a measured E_T of 10 GeV is multiplied by a factor 2 to account for the correction factor (see figure 4.21) and an additional 0.5 GeV is added to account for uncertainties in the energy lost beyond a clustering radius of 1.0. Table 6.1 gives the number of photons for events with two jets above 22.5 GeV and for events with two jets above 17.5 GeV.

Jet E_T Cut	Number of Events	Number of Photons	Uncertainty (%)
20.0	799	515	
17.5	1109	689	+34
22.5	600	407	-21

Table 6.1: Systematic Uncertainty due to Differences Between the Data and the model for parton fragmentation into jets.

The uncertainty due to the calorimeter response to jets is obtained by varying the single particle response function by $\pm 1\sigma$ and recalculating the correction function. The error is propagated by correcting the data with the $\pm 1\sigma$ correction

functions. These correction functions are shown in figure 4.21. The uncertainty on the cross section is determined by correcting the data with each of these correction functions in turn and recalculating the cross section. The uncertainty is 12%.

The uncertainty on the energy scale due to the dijet correction map is 3%. The uncertainty on the cross-section is determined in exactly the same manner as the model dependent uncertainty.

6.2 Uncertainties in the Method of Counting Photons

The method of counting isolated single photons is described in section 4.2. The efficiencies for both background and signal are derived from testbeam electron data. The measured profiles from the testbeam are used to simulate photon showers, adjusted for the fact that photons shower later than electrons. From the simulation the ratio of photons with $\tilde{\chi}^2 < 4$ to photons with $\tilde{\chi}^2 < 20$ is extracted. The same exercise is performed for the expected background. η^0s and π^0s of a given E_T are generated and simulated. Again the $\tilde{\chi}^2$ efficiency is determined as a function of E_T. The common uncertainties are due to the understanding of difference in electron and photon showers, differences in the fluctuations of photon and electron showers, and the understanding of gas saturation effects in the detector. In addition, the background efficiency depends on the understanding of the relative

population of various types of neutral mesons. Figure 6.2 shows the uncertainty on the number of photons as a function of photon E_T. The uncertainty on the cross-section due to the method of counting photons is 30%.

6.3 Other Uncertainties on the Normalization

The determination of the luminosity has a quoted uncertainty on the result of 10%. The photon energy scale is uncertain to 1%. Fitting the distribution of the photon E_T to the form

$$\frac{d\sigma}{dE_T} = \frac{A}{E_T^B}$$

results in

$$B = 4.3$$

Thus a 1% error in the energy scale translates to a 4% error on the cross-section. Corrections for the acceptance and the trigger efficiency introduce uncertainties of less than 2% and at that level are insignificant. An additional factor of 5% is introduced to account for these effects.

6.4 Effects of these uncertainties on the angular correlations

The effects described above would not affect the separation if the separation and E_T of the photon and the jets were independent variables. Because the separation

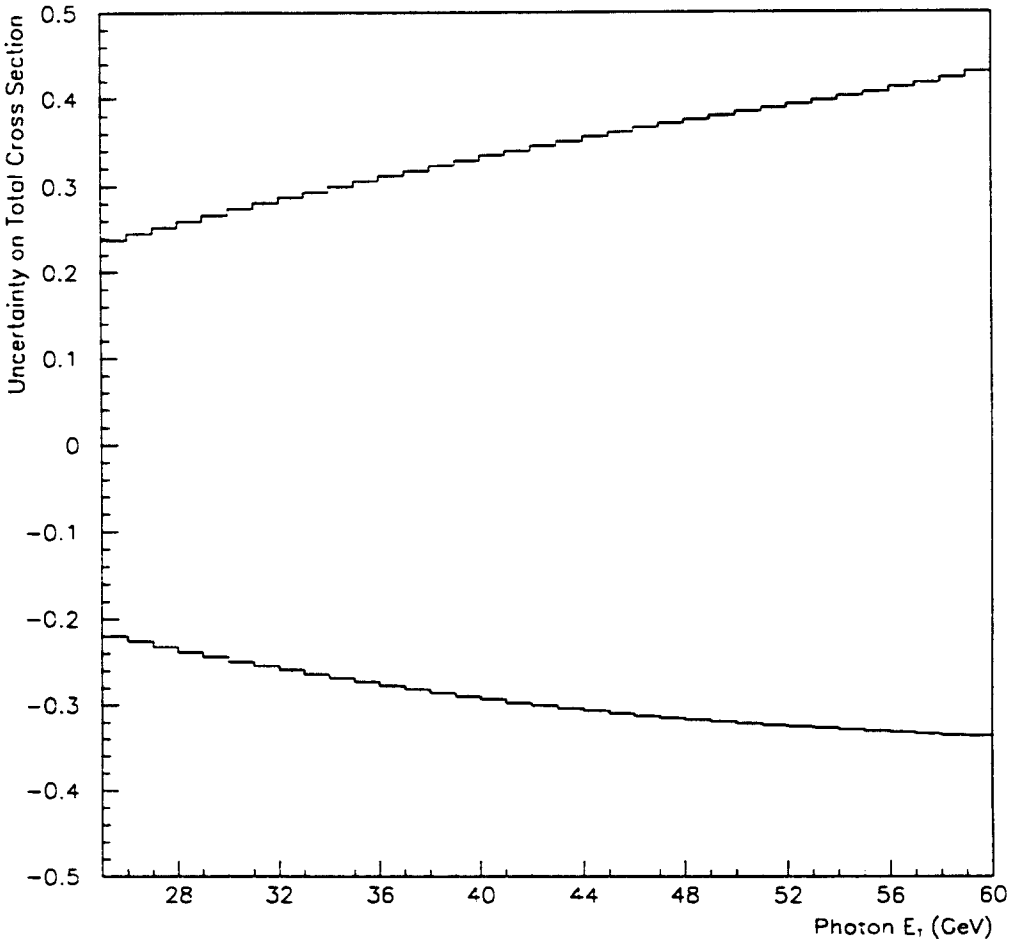

Figure 6.2: Uncertainty on the total cross section due the uncertainties introduced by the method of estimating the neutral meson background.

is correlated to the E_T of the photon and the jets (see figures 5.11,5.14, and 5.16), a systematic error on the E_T can affect the shape of the separation distribution.

6.4.1 Effect of the Jet Energy Scale on the Separation

To extract the uncertainty, the distribution of separation is made for the sample of events where the jet cut is lowered to 17.5 GeV and for the sample of events where the jet cut is raised to 22.5 GeV. Each distribution is then normalized to have the same area as the distributions with an E_T cut of 20 GeV. Figure 6.3 shows the comparison between the data sample used in the analysis, and the samples with the jet thresholds adjusted by 2.5 GeV. The variation is typically 10% though some bins show larger variations due to small populations.

To determine the effect due to understanding of the calorimeter, the distributions are calculated using the jet correction functions corresponding to a $\pm 1\sigma$ variation. Again the distributions are normalized to the area of those given in the preceding chapter and the difference is taken as the uncertainty (shown in figure 6.4. Here the effect is typically less than 10%.

The calculation of the uncertainty due to photon counting is somewhat more complicated. The uncertainty depends on both the photon E_T and the fraction of events with $\tilde{\chi}^2 < 4$. In figure 6.5 are shown the mean photon E_T and the fraction of events with $\tilde{\chi}^2 < 4$. As these are consistent with being constant for the separation of the photon and the leading jet, the uncertainty on this distribution is 0. As discussed in the previous chapter, the mean photon E_T increases with the

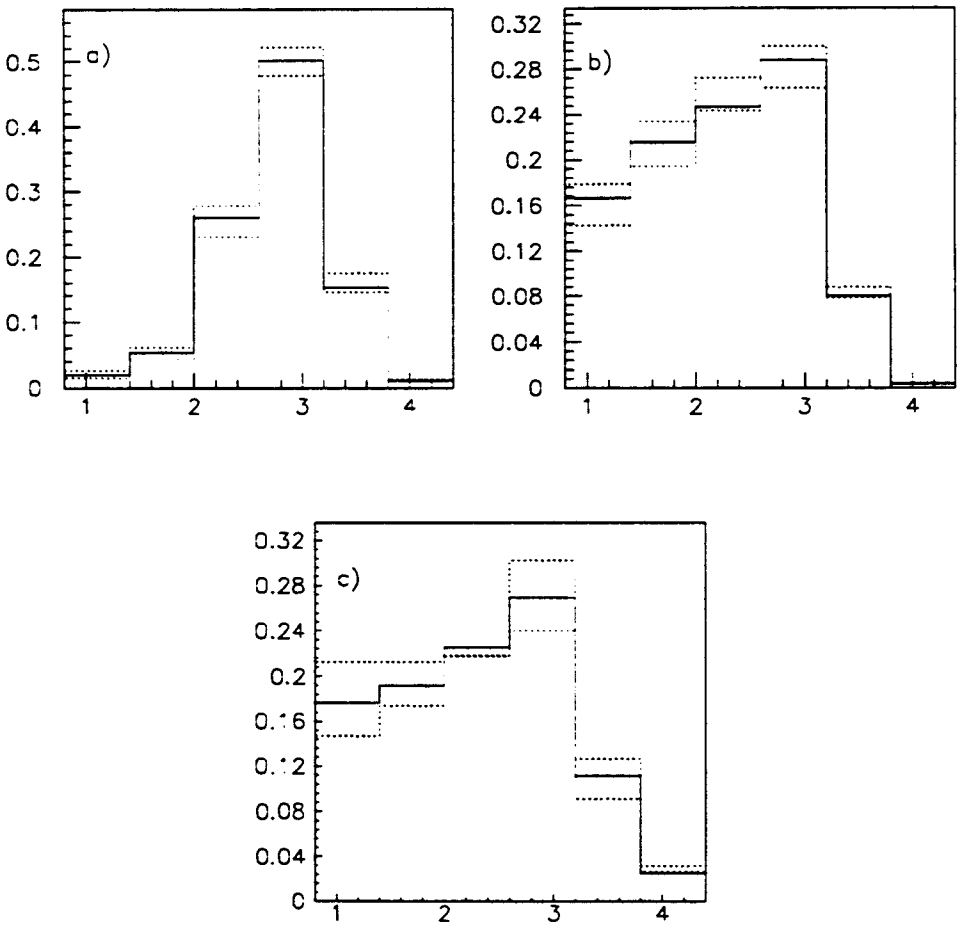

Figure 6.3: Uncertainty on the separation due to the model dependence of the jet energy scale. The separation of the photon and the leading jet is given in a), the separation of the photon and the second jet in b), and the separation of the two jets in c).

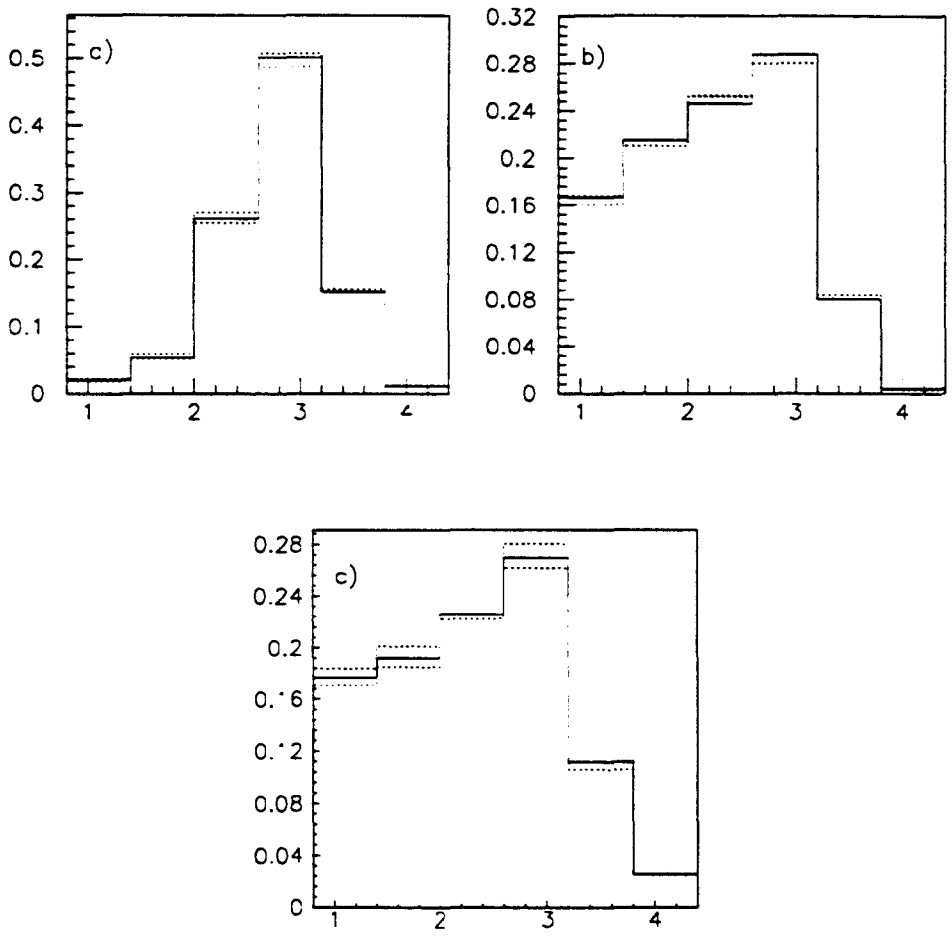

Figure 6.4: Uncertainty on the separation due to the uncertainty on the single particle response function. The separation of the photon and the leading jet is given in a), the separation of the photon and the second jet in b), and the separation of the two jets in c).

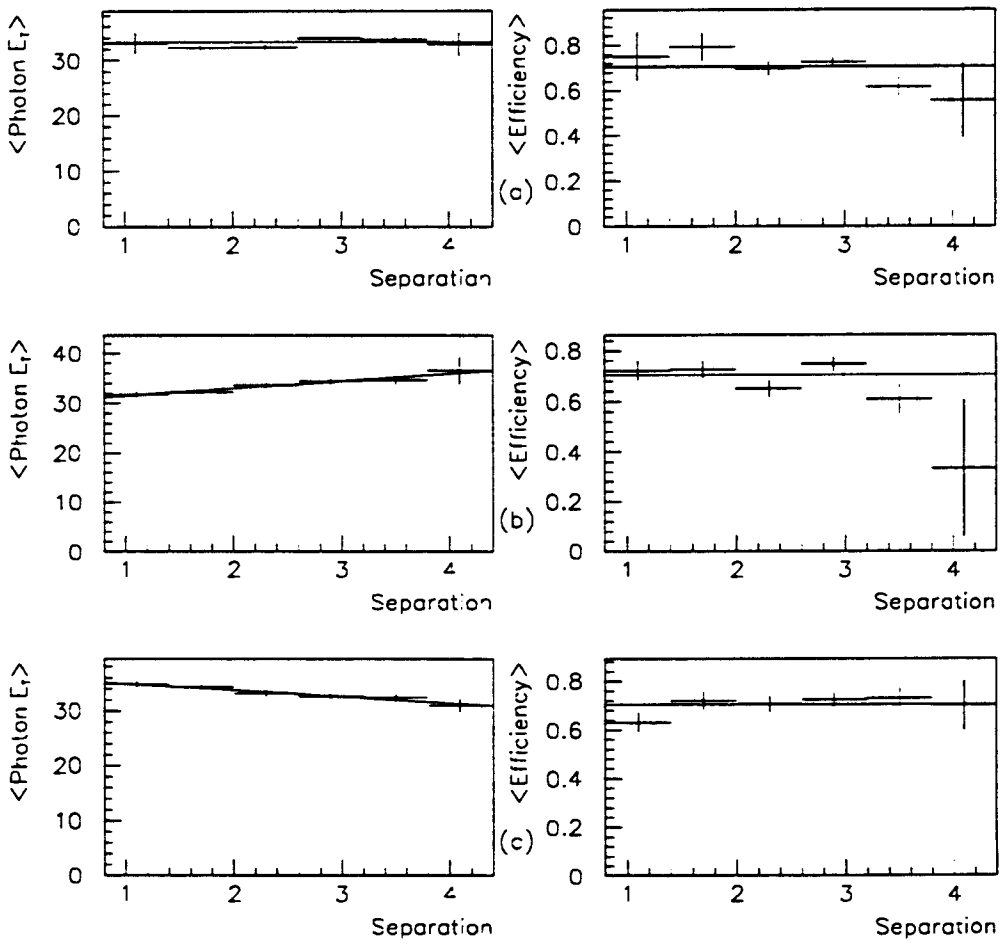

Figure 6.5: Mean photon E_T and the fraction of events with $\tilde{\chi}^2 < 4$ plotted for each bin of the separation (a) of the photon and the leading jet, (b) of the photon and second jet, and (c) of the two jets.

separation of the photon and the second jet; and decreases with the separation of the two jets. In all case the fraction with $\tilde{\chi}^2 < 4$ is consistent with being constant over all bins. To estimate the uncertainty, the change in photon content is calculated from the $\pm 1\sigma$ variations in the $\tilde{\chi}^2$ efficiency. The distributions are again renormalized and the difference taken as the uncertainty. The systematic uncertainties for these two distributions are given in table 6.2.

Bin of Separation	Photon-Jet 2	Jet 1-Jet 2
0.8-1.4	5.0	4.5
1.4-2.0	2.5	2.5
2.0-2.6	0.0	0.0
2.6-3.2	3.0	2.0
3.2-3.8	5.5	4.5
3.8-4.4	8.5	6.0

Table 6.2: Systematic error on the separation of the photon and the second jet and on the separation of the two jets (in %) for each bin of separation.

6.4.2 Angular resolution effects

The cross-section is not sensitive to angular resolution. However the separation might depend on bin-to-bin smearing due to events flowing from well populated bins to neighboring bins with smaller populations. To estimate the effect, the data

are convoluted with a gaussian resolution function of mean, 0, and width, 0.1. The width is estimated from the determination of the jet resolution function. Figures 6.6 and 6.7 show a gaussian fit to the difference between the parton direction and the measured jet direction in both η and ϕ view. The data are used to calculate the uncertainty. The η and ϕ of each jet are smeared using the fits to the resolution of determining the parton direction from the jet direction. Then the separation is recalculated for each event, and binned. This procedure is repeated 10000 times for the entire event sample. The difference between the mean bin contents of the smeared distributions and the bin contents of the unsmeared distribution is an estimate of the uncertainty due to the angular resolution. Again for bins with large statistics the uncertainty is less than 10% as summarized in table 6.3.

6.4.3 Uncertainty in the identification of the lead jet

As mentioned in section 4.3, the theoretical calculation is convoluted with the jet response function and the difference between the smeared and unsmeared theory are used to correct the data. However because it is impossible to gauge the accuracy of the correction, 50% of the correction is taken as the uncertainty on the correction. Table 6.4 lists the bin contents after the correction and the uncertainty due to the correction.

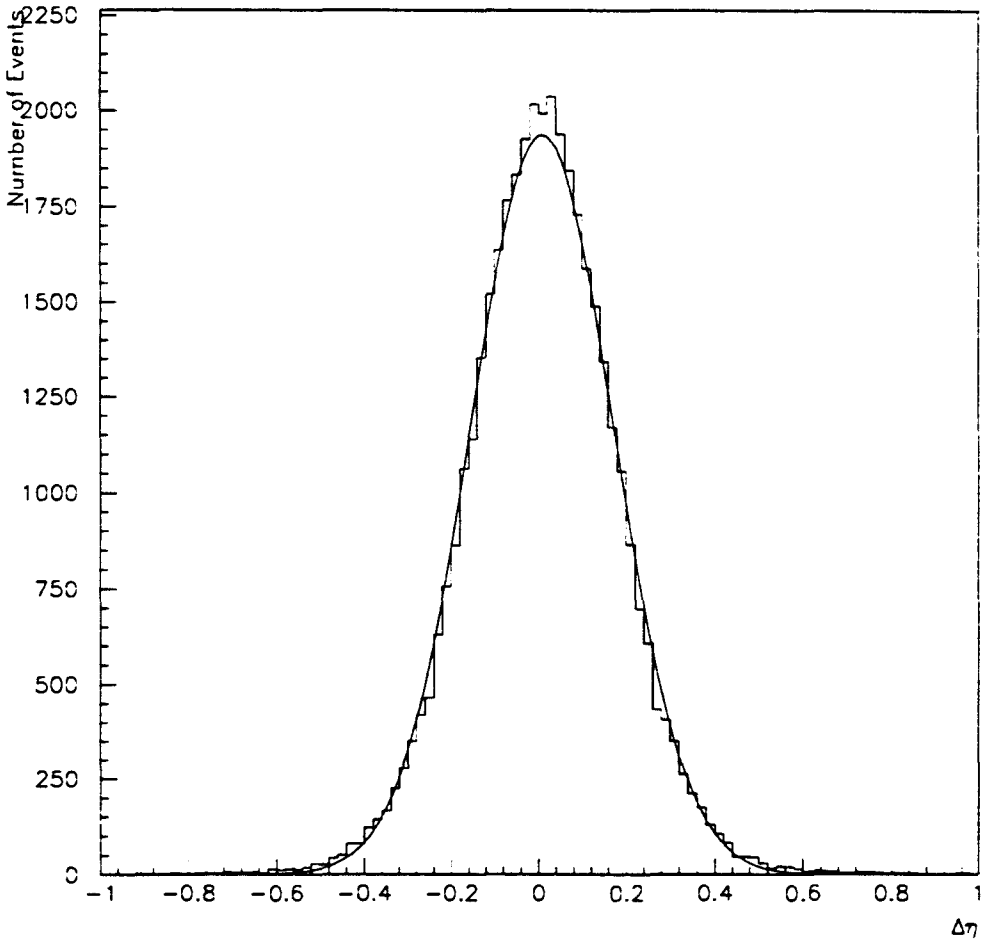

Figure 6.6: Gaussian fit to the difference between the generated parton η and the measured jet η

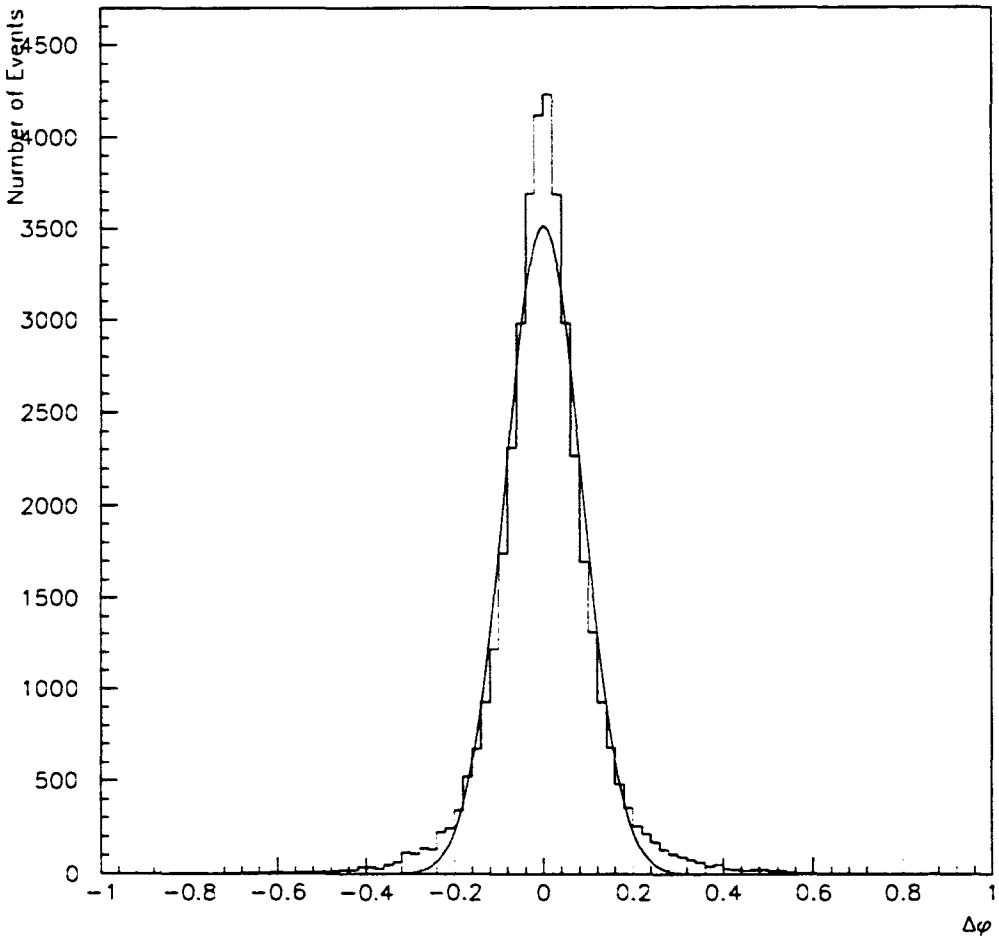

Figure 6.7: Gaussian fit to the difference between the generated parton ϕ and the measured jet ϕ

bin	Photon - Jet 1 uncertainty	Photon - Jet 2 uncertainty	Jet 1 - Jet 2 uncertainty
0.8 - 1.4	0.001	0.006	0.018
1.4 - 2.0	0.001	0.013	0.025
2.0 - 2.6	0.011	0.008	0.026
2.6 - 3.2	0.032	0.010	0.019
3.2 - 3.8	0.021	0.011	0.004
3.8 - 4.4	0.003	0.002	0.003

Table 6.3: Summary of the uncertainty on the separation due to the jet angular resolution.

	Photon - Jet 1		Photon - Jet 2		Jet 1 - Jet 2	
bin	contents	uncertainty	contents	uncertainty	contents	uncertainty
0.8-1.4	0.000	0.016	0.217	0.007	0.056	0.010
1.4-2.0	0.022	0.036	0.319	0.023	0.195	0.008
2.0-2.6	0.322	0.029	0.166	0.001	0.253	0.004
2.6-3.2	0.608	0.000	0.283	0.058	0.334	0.006
3.2-3.8	0.044	0.001	0.019	0.006	0.131	0.003
3.8-4.4	0.004	0.000	-.003	0.002	0.031	0.000

Table 6.4: Bin contents and uncertainty associated with the correction for misassignment of which jet is jet 1 and which jet is jet 2.

Chapter 7

Conclusions

The final measurement of the cross section for $\bar{p}p$ giving a photon and two jets with

- 25.0 GeV < Photon E_T < 54.0 GeV
- | Photon η| < 0.9
- 20.0 GeV < Jet E_T
- | Jet η| < 2.0
- all objects separated by greater than 0.8 in $\eta - \phi$ space

including all uncertainties is

$$\sigma = 369 \pm 42(\text{stat})^{+181}_{-151}(\text{syst.})\text{pb} \tag{7.1}$$

where the systematic error is the sum in quadrature of all the uncertainties described in Chapter 6. Summing the theoretical and experimental errors in quadrature, and comparing the two suggests that the theoretical value is low by 1.24 σ. The probability that the cross section is given by the theoretical value, and the data is randomly high by 1.24 σ is 10%.

To compare the shapes, a χ^2 is computed for each E_T spectrum comparing the data to both the QCD calculation and the phase space calculation. Table 7.1 gives the results of the χ^2 comparison for the E_T distributions. The photon spectrum

		Data - Theory		Data - Phase	
Spectrum	# d.o.f.	χ^2	χ^2/d.o.f.	χ^2	χ^2/d.o.f.
Photon E_T	6	2.50	0.42	8.46	1.41
Leading Jet E_T	5	2.17	0.43	2.00	0.40
Second Jet E_T	4	7.21	1.80	6.36	1.59

Table 7.1: χ^2 comparison of the data to the theoretical calculation. The results are consistent with the hypothesis that the data events result from QCD processes.

is more consistent with the QCD calculation than the phase space calculation. The χ^2 values for the jet E_T spectra suggest that the data agree with both the QCD calculation and the phase space calculation. In part this agreement is due to limitations of the detector in measuring jet energies. While the resolution for

measuring photon E_T is typically 3%, the jet resolution at 20 GeV is $> 30\%$. This has been a major limitation in this analysis.

The χ^2 comparison of the data to the QCD calculation and the data to the phase space calculation for the separation distributions are given in table 7.2. Here the data clearly favors the interpretation that the measured separation dis-

	Data - Theory		Data - Phase	
Separation of	χ^2	χ^2/d.o.f.	χ^2	χ^2/d.o.f.
Photon - Leading Jet	2.13	0.43	7.03	1.41
Photon - Second Jet	7.63	1.53	19.84	3.97
Leading Jet - Second Jet	3.43	0.69	20.69	4.14

Table 7.2: χ^2 comparison of the data to the theoretical calculation for the separation distributions. The results are consistent with the hypothesis that the data events result from QCD processes.

tributions are consistent with the QCD calculation. The separation is a useful variable because it links properties of the matrix elements to a quantity which is well measured despite statistical limitations. Chapter 5 showed that the separation is sensitive to the rise in cross section in the regions of collinearity including collinearity with the beam. An improvement would be to extend the analysis to include photons in the plug calorimeter and jets in the forward calorimeter.

The above results lead one to conclude that the topology of the events is consistent with QCD. However the cross section is high by a factor of 2. CDF has also measured the cross section for W and Z production[34]. To leading order, these processes are due entirely to quark-quark initial states. Next-to-leading order QCD calculations [35] of W and Z production give a K factor (see Chapter 1) of 1.33. The measured cross sections agree with next-to-leading order theoretical calculations. A process which depends primarily on gluon-gluon initial states is b quark production. The cross section for this process is larger than the next-to-leading logarithm calculation[36] by a factor 2. Taken together, these measurements suggest that the gluon distribution is perhaps too small by a factor 1.4. However it is unlikely to be the normalization which is incorrect. Previous measurements of the gluon distribution at CERN find that the measured gluon distribution agrees with expectations. Photon production at the Tevatron probes a smaller range of x than was accessible at the ISR and the S$\bar{p}p$S. Thus the gluon distribution at low x has to be increased. This implies a 25% change in the value of B (see Appendix A) to increase the number of low x gluons by a factor 1.4, and a corresponding change in C to keep the gluon distribution at higher values of x unchanged.

Appendix A

CTEQ Leading Order Parton Distribution Functions

This appendix details the functional form of the CTEQ leading order parton distribution functions used in this analysis. The form given corresponds to the number density of a particular type of parton as a function of the momentum fraction carried by the parton. The distributions given include the density of valence u and d quarks in the proton, the density of the u, d, s and c sea in the proton and the density of gluons. Each function is parameterized as

$$f(x) = Ax^B(1-x)^C(1+Dx^E)[\log(1+\frac{1}{x})]^F \tag{A.1}$$

The parameters, A, B, C, D, E, and F are determined from deep inelastic scattering experiments and various sum rules. Each parameter is given as a cubic

polynomial in y where

$$y = \log[\log(Q/\Lambda)/\log(Q_{\min}/\Lambda)] \tag{A.2}$$

Tables A.1, A.2, and A.3 give the coefficients of each term for the various distributions.

		1	y	y^2	y^3
	A	1.791	-0.804	-0.797	0.718
	B	1.572	0.069	0.005	-0.037
d_v	C	3.470	-0.375	2.267	-1.261
	D	-0.685	-0.828	2.042	-1.208
	E	1.007	-0.732	1.490	-0.966
	F	0.000	0.741	0.563	-0.525
	A	0.513	0.016	-0.062	0.007
	B	0.276	0.052	0.000	-0.006
u_v	C	3.579	0.763	-0.135	0.083
	D	16.993	-13.045	4.336	-0.360
	E	1.120	-0.357	0.008	0.028
	F	0.000	0.311	0.029	-0.010
	A	2.710	-4.804	2.629	-0.404
	B	-0.010	-1.636	2.087	-0.637
g	C	7.174	2.102	-2.209	-0.420
	D	28.904	-22.607	-15.131	18.092
	E	2.572	-0.437	-0.968	0.243
	F	0.000	-1.776	4.266	-0.335

Table A.1: CTEQ leading order parameterization of the valence quark momentum density and the gluon momentum density. The method of determining the density is given in the text.

		1	y	y^2	y^3
	A	0.278	-0.284	0.180	-0.051
	B	0.000	0.086	-0.866	0.419
u_{sea}	C	11.000	-1.281	1.252	0.061
	D	36.338	-35.113	9.398	5.093
	E	1.960	-0.339	-0.342	0.365
	F	0.000	1.424	-2.750	1.223
	A	0.154	-0.102	0.001	0.009
	B	0.128	0.279	-0.786	0.363
d_{sea}	C	8.649	0.071	0.351	-0.051
	D	42.685	-26.342	1.616	5.854
	E	2.238	-0.338	-0.199	0.157
	F	0.000	1.681	-2.068	0.975
	A	0.372	-0.721	0.560	-0.164
	B	0.009	0.610	-1.387	0.579
s_{sea}	C	10.273	-4.833	6.583	-2.633
	D	-0.840	1.652	-0.324	-0.251
	E	0.819	-1.660	1.845	-0.829
	F	0.000	3.558	-3.940	1.302

Table A.2: CTEQ leading order parameterization of the u,d, and s sea quark momentum density. The method of determining the density is given in the text.

		1	y	y^2	y^3
	A	1.000	-22.091	7.121	-8.303
For the charm sea, $A = A\sqrt{\log \frac{Q}{Q_{\min}}} \times 10^{-5}$					
	B	0.125	-0.303	0.156	-0.091
c_{sea}	C	2.039	1.216	11.530	-8.066
	D	13.849	-37.954	52.370	-24.283
	E	0.306	-0.090	0.953	-0.487
	F	2.735	0.181	-0.517	0.054
	A	1.000	-21.599	3.138	-18.833
For the bottom sea, $A = A \times 3.751 \times 10^{-4}$					
	B	-0.026	-0.772	1.150	-0.504
b_{sea}	C	4.924	4.011	-4.701	0.110
	D	1.842	-6.304	5.766	-1.964
	E	-0.135	0.875	-1.263	0.667
	F	1.563	-0.492	1.593	-0.351

Table A.3: CTEQ leading order parameterization of the c and b sea quark momentum density. The method of determining the density is given in the text.

Appendix B

Testbeam Measurements of the Calorimeter Response

The calorimeter energy measurements depend directly on the energy scale measured using testbeam electrons and pions. The scale is determined by independently measuring the momentum of each particle observed in the calorimeter. This appendix describes the measurement of the momentum of the testbeam particles.

The CDF testbeam originates at target MT2 (figure B.1). A beam of 900 GeV/c protons is steered into target MT2CON. The MT2W, MT3V, MT3W, and MT3U dipoles are used to steer the secondary beam onto the MT5E aperture. The MT3Q and MT4Q quadrupoles are used to focus the beam properly at the MT5E aperture and at the detector. The secondary beam is assumed to be pions

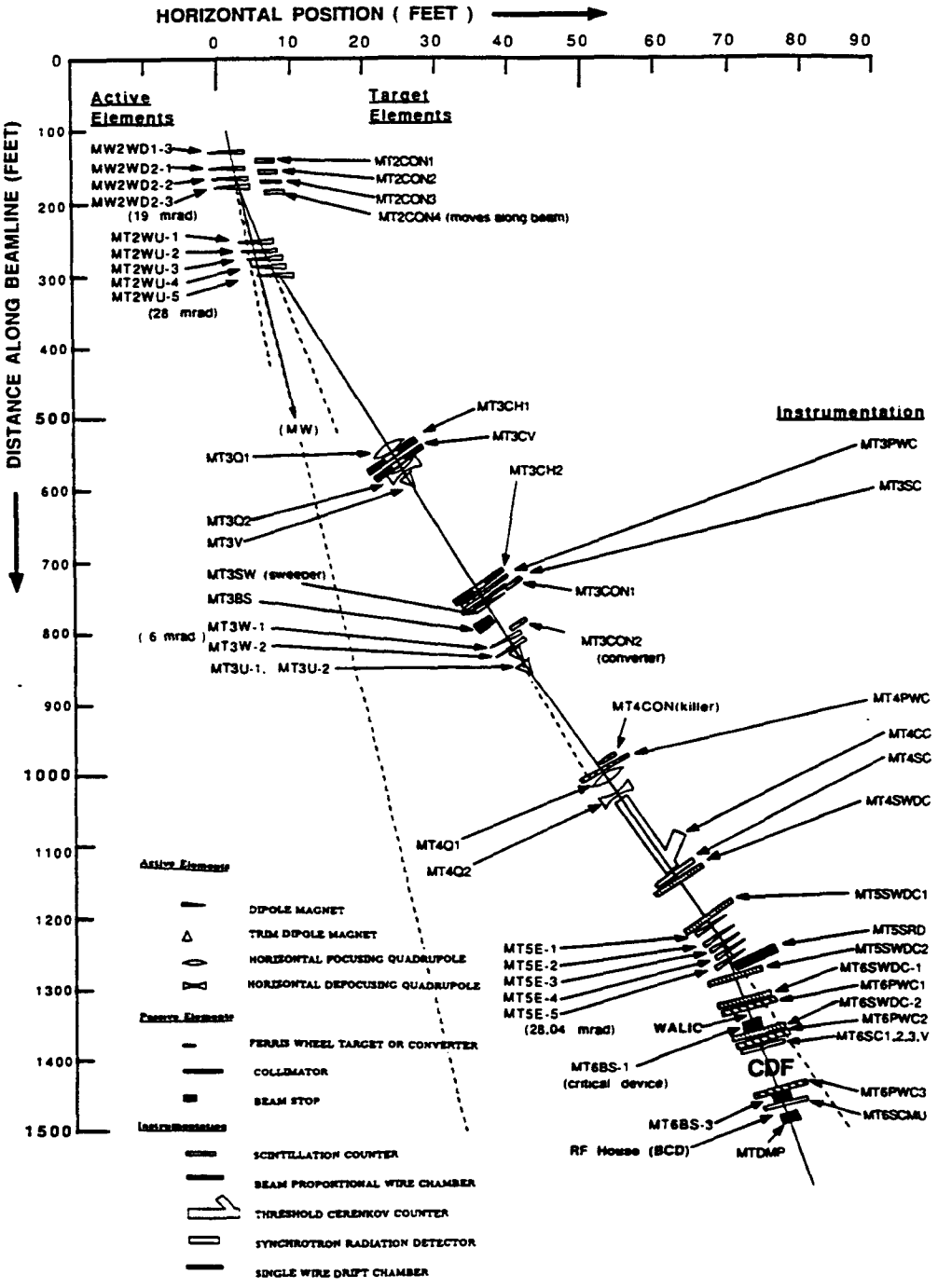

Figure B.1: Schematic of the MT beam line used by CDF to calibrate the calorimeters.

(this is a good assumption for negative pions - for high energy positive pions the proton fraction of the beam was measured and corrected for). Electron beams were created by inserting the MT3CON1 target.

The MT5E bend string selects a particular momentum byte as the CDF detector is at an angle of 28 milliradians with respect to the beam direction before the MT5E bend string. Particles of momentum, p, will be bent by an angle, θ, where

$$p = 0.3\frac{\int Bdl}{\theta} \tag{B.1}$$

Adjusting the current in the MT5E bend string changes the value of the magnetic field integral and hence the momentum of particles arriving at the calorimeter. However the angular acceptance is such that the beam has a typical momentum spread

$$\frac{\Delta p}{p} = 1.6\% \tag{B.2}$$

To accurately calibrate the calorimeters requires the removal of this factor from the measured calorimeter response.

Two pairs of single wire drift chambers (SWDC)[37] are placed before and after the MT5E magnet. These chambers measure the position of particles in the plane transverse to the beam direction. Each chamber consists of 4 sense wire planes: two which measure the horizontal coordinate, two which measure the vertical coordinate. Each pair is separated by 22.4 mm. This permits an *in*

situ calibration of the drift velocity (v_d)and the time it takes the signal to travel from the chamber to the counting room (t_0).

Knowing v_d and t_0 enables one to calculate the allowed $x(y)$ for each vertical (horizontal) wire. There are four possible combinations of each pair, but only one which will agree. The path of the particles in the $x-z$ plane is reconstructed from knowledge of the location of the chambers. Before and after the bend magnet, the trajectories are assumed to be straight lines. The difference in the two slopes gives the bend angle, hence the momentum (through relation B.1). Figure B.2 shows the measured beam positions at each of the four chambers for 227 GeV/c pions and 100 GeV/c electrons.

To demonstrate that the momentum measurement is well understood, a gaussian fit is made to the distribution of energy and momentum for 100 GeV electrons. A gaussian fit is also made to the ratio of the energy to the momentum. If the two measurements were uncorrelated, then the ratio would have a width given by

$$\sqrt{\frac{\sigma_E{}^2}{E} + \frac{\sigma_P{}^2}{P}} \tag{B.3}$$

If the two measurements are correlated, then the width would be

$$\sqrt{\frac{\sigma_E{}^2}{E} - \frac{\sigma_P{}^2}{P}} \tag{B.4}$$

Table B.1 gives the parameters of the gaussian fits to the three distributions. From these numbers it is clear that the momentum and energy are correlated. This ensures that the geometry of the system is well understood.

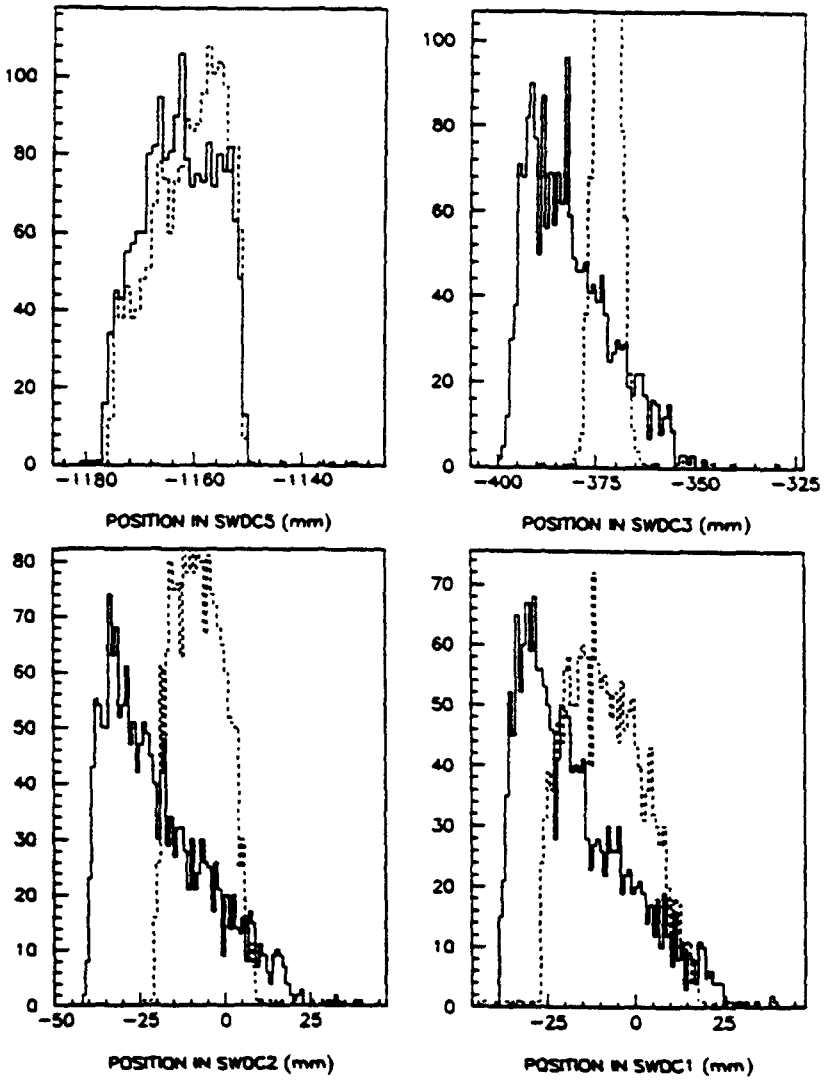

Figure B.2: Profiles of the beams used to calibrate the calorimeters. SWDC 5 is closest to the calorimeter, and SWDC 1 is furthest from the calorimeter. The solid line is 100 GeV/c electrons and the dashed line is 227 GeV/c pions.

Energy (GeV)	Momentum (GeV/c)	E/p	σ_E/E	σ_p/p	$\sigma_{E/p}/E/p$
149.764	151.626	0.987	0.024	0.017	0.015
99.158	100.067	0.991	0.024	0.016	0.018
50.184	50.588	0.993	0.027	0.015	0.023
25.191	25.378	0.994	0.035	0.016	0.031

Table B.1: Table of parameters of gaussian fits to the distribution of measured energy of testbeam electrons demonstrating that the energy and momentum measurements are 100% correlated.

The uncertainty in the scale is due to uncertainties in the location of the chambers and uncertainties in the value of $\int Bdl$. The chamber position is known to 10 μm which gives an uncertainty of 0.1% on the measured momentum. The field integral is known to 1%. This sets an overall uncertainty on the calorimeter energy scale of 1%.

Appendix C

Parameterization of the jet response function

The jet response function is assumed to have a functional form of a gaussian smeared by two exponentials. The reason for this choice is that the exponentials contribute long tails to the distribution without changing the behavior near the mean. The following derivation gives the functional form of the jet response function.

The derivation starts by convoluting two exponential distributions of opposite slope. The exponentials are considered to have mean 0. Thus their parameterization is given by:

$$f_{-}(x) = \frac{1}{a}\exp\frac{-(x+a)}{a}, x > -a \quad \text{(C.1)}$$

$$f_{+}(x) = \frac{1}{b}\exp\frac{((x-b)}{b}, x < b \quad \text{(C.2)}$$

where a describes an exponential with negative slope (high tail) and b describes an exponential with positive slope (low tail). Performing the convolution results in the function:

$$f(x) = \begin{cases} \frac{1}{a+b} \exp \frac{(x-a+b)}{b}, & x < b-a \\ \frac{1}{a+b} \exp \frac{-(x-a+b)}{a}, & x > b-a \end{cases} \tag{C.3}$$

This function has mean, 0, and is valid over the range $-\infty < x < \infty$. This distribution is now convoluted with a gaussian of mean, μ, and width, σ. The first step is to write down the integral:

$$\begin{aligned} f(x) = & \frac{1}{(a+b)\sigma\sqrt{2\pi}} \\ & \left[\int_{-\infty}^{b-a} \exp\left(\frac{(z-a+b)}{b}\right) \exp\left(-\frac{(x-z-\mu)^2}{2\sigma^2}\right) dz + \right. \\ & \left. \int_{b-a}^{+\infty} \exp\left(\frac{-(z-a+b)}{a}\right) \exp\left(-\frac{(x-z-\mu)^2}{2\sigma^2}\right) dz \right] \end{aligned} \tag{C.4}$$

Combining the exponential arguments, rationalizing the square, and factoring out the terms in x gives

$$\begin{aligned} f(x) = & \frac{1}{(a+b)\sqrt{2\pi}} \\ & \left[\exp\left(\frac{(x-a+b)}{b} + \frac{\sigma^2}{2b^2}\right) \int_{-(x-\mu-a+b)/\sigma-\sigma/b}^{\infty} \exp\left(-\frac{y^2}{2}\right) dy + \right. \\ & \left. \exp\left(-\frac{(x-a+b)}{a} + \frac{\sigma^2}{2a^2}\right) \int_{-\infty}^{(x-\mu-a+b)/\sigma+\sigma/a} \exp\left(-\frac{y^2}{2}\right) dy \right] \end{aligned} \tag{C.5}$$

Each term is the product of the integral of the gaussian frequency and an exponential. A simple description is that in the vicinity of the mean, the function describes a gaussian. Far from the mean, the shape is determined by the exponentials.

Appendix D

Fitting methods

Two methods of fitting data to a given functional form were used in this work. In this appendix, we discuss and compare the two methods. A more theoretical description of the use of probability and statistics is given in [38].

First, here are some useful definitions. The data are a set of N points $\{y_i\}$ where each value, y_i depends on a coordinate x_i. The functional form is given as $f(x, \vec{\alpha})$. Here the vector of parameters, $\vec{\alpha}$ are to be determined by the fitting procedure.

D.1 χ^2 method

The χ^2 method minimizes the quantity

$$\chi^2 = \sum_{i=1}^{N} \frac{(y_i - f(x_i, \vec{\alpha}))^2}{\sigma_i^2} \tag{D.1}$$

where σ_i is the uncertainty on the value y_i. Taking the derivative with respect to $\vec{\alpha}$ gives

$$\frac{d\chi^2}{d\vec{\alpha}} = 0 = -2\sum_{i=1}^{N} \frac{(y_i - f(x_i, \vec{\alpha}))}{\sigma_i^2} \frac{df}{d\vec{\alpha}}(x_i, \vec{\alpha}) \tag{D.2}$$

The solution of this equation proceeds in one of two directions.

D.1.1 Solution if f is linear in the parameters

If f is linear in α, f can be written:

$$f(x, \vec{\alpha}) = g_1(x)\alpha_1 + g_2(x)\alpha_2 + ... \tag{D.3}$$

The equation then becomes a matrix equation:

$$0 = \widetilde{M}\vec{\alpha} - \vec{V} \tag{D.4}$$

where

$$M_{jk} = \sum_{i=1}^{N} \frac{g_j(x_i)g_k(x_i)}{\sigma_i^2} \tag{D.5}$$

$$V_j = \sum_{i=1}^{N} \frac{g_j(x_i)y_i}{\sigma_i^2} \tag{D.6}$$

The solution for the parameters, $\vec{\alpha}$ is

$$\vec{\alpha} = \widetilde{M}^{-1}\vec{V} \tag{D.7}$$

This form is known as linear least squares.

D.1.2 Solution if f is non-linear in the parameters

In the case where f is non-linear in the parameters, $\vec{\alpha}$, the procedure begins with expanding the χ^2 as a function of the parameters about some chosen value for the $\vec{\alpha}$ called $\vec{\alpha}_j$.

$$\chi^2(\vec{\alpha}) = \chi^2(\vec{\alpha}_j) + \frac{d\chi^2}{d\vec{\alpha}}(\vec{\alpha}_j)\,(\vec{\alpha} - \vec{\alpha}_j) + \frac{1}{2}(\vec{\alpha} - \vec{\alpha}_j)\,\frac{d^2\chi^2}{d\vec{\alpha}^2}(\vec{\alpha}_j)\,(\vec{\alpha} - \vec{\alpha}_j) \tag{D.8}$$

Taking the derivative with respect to $\vec{\alpha}$ gives

$$0 = \frac{d\chi^2}{d\vec{\alpha}}(\vec{\alpha}_j) + \frac{d^2\chi^2}{d\vec{\alpha}^2}(\vec{\alpha}_j)\,(\vec{\alpha} - \vec{\alpha}_j) \tag{D.9}$$

This defines an iterative procedure to determine $\vec{\alpha}$ from $\vec{\alpha}_j$. Writing this as a matrix equation,

$$0 = \vec{V} - \widetilde{M}(\vec{\alpha} - \vec{\alpha}_j) \tag{D.10}$$

with

$$\vec{V} = \frac{d\chi^2}{d\vec{\alpha}}(\alpha_j) \text{ and } \widetilde{M} = \frac{d^2\chi^2}{d\vec{\alpha}^2}(\vec{\alpha}_j) \tag{D.11}$$

Solving this equation gives

$$\vec{\alpha} = \widetilde{M}^{-1}\vec{V} + \vec{\alpha}_j \tag{D.12}$$

This value can now be substituted in the above equation for $\vec{\alpha}_j$ and the procedure repeated anew. The most common practice is stop when the change in the χ^2 is on the same order as the accuracy of the machine.

In practice, this procedure converges in a limited number of iterations, provided that the initial parameters are chosen close to their true value, and that the χ^2 is well-defined, and possesses no local minima. This is the iterative method. It is used in all track fitting routines, the definition of the CES χ^2, and in the CERN routine minuit.

D.2 The Log Likelihood definition

The other general functional form is defined by describing the quality of a fit as the product of the probabilities that a given set of parameters result in a set of measured points. The form is

$$L = \prod_i f(x_i, y_i; \vec{\alpha}) \tag{D.13}$$

Taking the negative log gives

$$-\log L = -\sum_i \log(f(x_i, y_i; \alpha) \tag{D.14}$$

Because the probability is always < 1, $-\log L > 0$.

The general method is to assume that the function, $\mu(x; \vec{\alpha})$, gives the mean of a poisson distribution. Then the probability of observing a point, y_i, for a coordinate, x_i is given by

$$f_i(x_i, y_i; \vec{\alpha}) = e^{-\mu}\frac{\mu^{y_i}}{y_i!} \tag{D.15}$$

giving

$$\log f = y_i \log(\mu) - \mu - \log(y_i!) \tag{D.16}$$

Using Stirling's approximation,

$$\log f = y_i \log(\frac{\mu}{y_i}) + (y_i - \mu) + \text{Constant} \tag{D.17}$$

Taking the derivative with respect to μ gives

$$\frac{d \log f}{d\mu} = (\frac{y_i}{\mu} - 1) \tag{D.18}$$

To solve for the parameters, $\vec{\alpha}$ one proceeds in exactly the same manner as in the case of a non-linear χ^2. The iteration proceeds until the likelihood function fails to improve.

D.3 Comparison of the Likelihood and χ^2 methods

In the case of infinite statistics, both methods are identical. In the case of fitting a histogram where some bins have small populations, the χ^2 method will be biased by regions with poor statistics. This is important when fitting for the jet response function because the exponential tails are determined in regions of poor statistics. Figure D.1 shows each bin's contribution to the likelihood (left)or χ^2 (right) for a parton E_T of 50 GeV. On the tails, the likelihood is finite, while the χ^2 is 0 indicating that undue weight is being given to the tails in the χ^2 method.

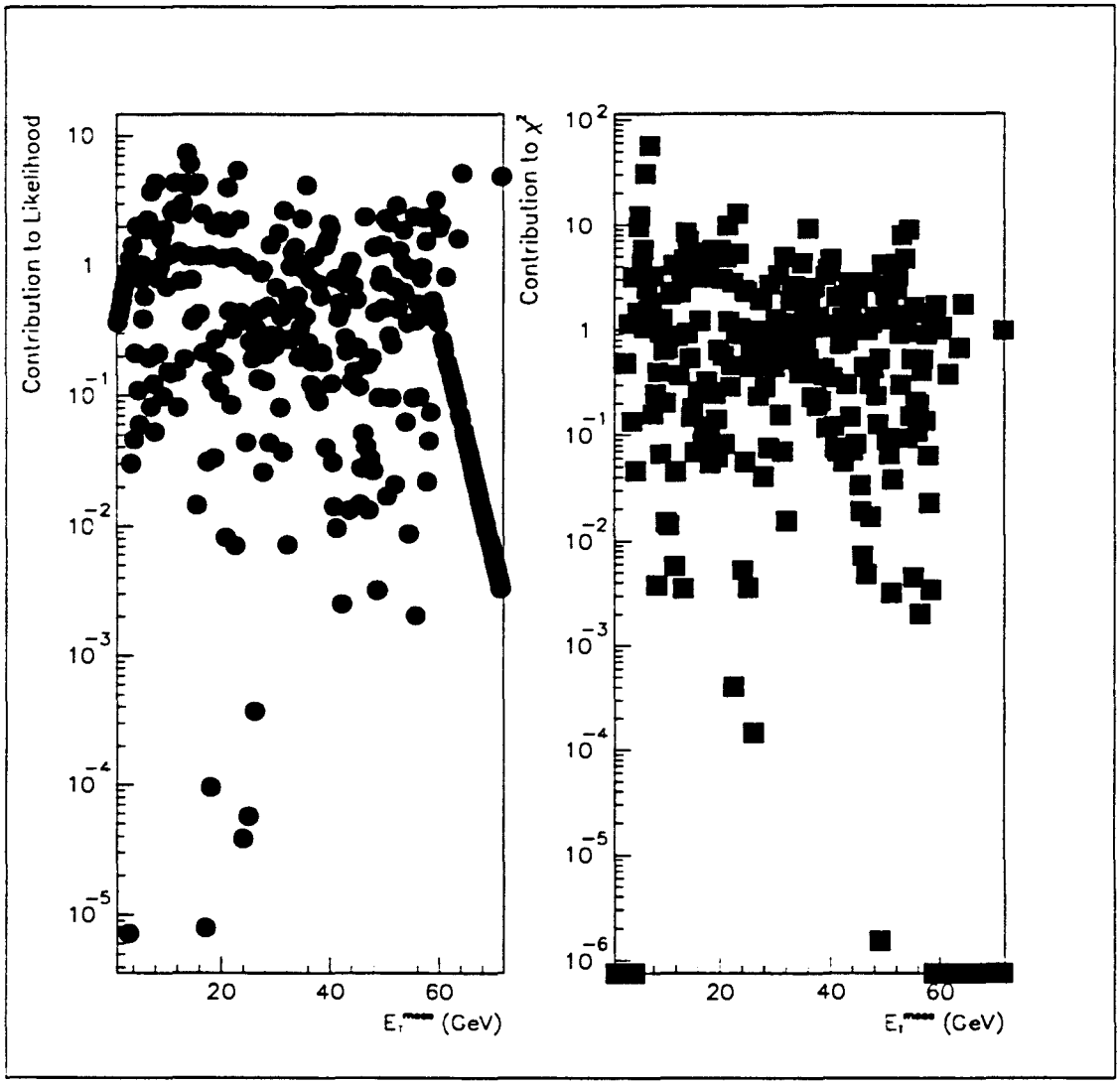

Figure D.1: Comparison of each bin's contribution to the Likelihood (left) or χ^2 (right) for a parton E_T of 50 GeV.

Bibliography

[1] I. J. R. Aitchison and A. J. G. Hey. *Gauge Theories in Particle Physics.* Graduate Student Series in Physics. Adam Hilger, second edition, 1989.

[2] D. Gross and F. Wilczek. Ultraviolet Behavior & Non-Abelian Gauge Theories. *Physical Review Letters*, 30:1343, 1973.

[3] D. Politzer. Reliable Perturbative Results for Strong Interactions. *Physical Review Letters*, 30:1346, 1973.

[4] T. Akesson et al. High p_t γ and π^0 Production, Inclusive, and with a Recoil Hadronic Jet, in pp collisions at $\sqrt{s}$ = 63 gev. *Soviet Journal of Nuclear Physics*, 51:836–845, 1990.

[5] J. Alitti et al. Measurement of the Gluon Structure Function from Direct Photon Data at the CERN $\bar{p}p$ Collider. *Physics Letters*, B299:174–182, 1993.

[6] F. Abe et al. A Prompt Photon Cross Section Measurement in $\bar{p}p$ Collisions at $\sqrt{s}$ = 1.8 TeV. 1992. Submitted to Physical Review D.

[7] J. Alitti et al. A Measurement of the Direct Photon Production Cross-section at the CERN $\bar{p}p$ Collider. *Physics Letters*, B263:544–550, 1991.

[8] CTEQ Collaboration. CTEQ Parton Distributions and Flavor Dependence of Sea Quarks. *Physics Letters B*, B304:159–166, 1993.

[9] J. P. Mansour. Private communication.

[10] P. Aurenche et al. Scheme Invariant Higher Order QCD Predictions for Large p_t Photoproduction Reactions. *Nuclear Physics B*, pages 553–, 1987.

[11] J. Ohnemus H. Baer and J.F. Owens. A Next-to-leading Logarithm Calculation of Direct Photon Production. *Physical Review*, D42:61–71, 1990.

[12] G. Dugan. Tevatron Status. In *Proceedings of the 1989 IEEE Particle Accelerator Conference*, pages 426–430, 1989.

[13] J. Gannon et al. Flying Wires at Fermilab. In *Proceedings of the 1989 IEEE Particle Accelerator Conference*, pages 68–70, 1989.

[14] Rolland Johnson. Initial Operation of the Tevatron Collider. In *Proceedings of the 1987 IEEE Particle Accelerator Conference*, pages 8–12, 1987.

[15] P. Martin et al. Anti-proton Acceleration in the Fermilab Main Ring and Tevatron. In *Proceedings of the 1987 IEEE Particle Accelerator Conference*, pages 47–49, 1987.

[16] F. Snider et al. The CDF Vertex TPC System. *Nuclear Instruments and Methods*, A268:75–91, 1988.

[17] F. Bedeschi et al. The CDF Central Tracking Chamber. *Nuclear Instruments and Methods*, A268:50–74, 1988.

[18] D. Nordstrom L. Brown and S. Brown. Review of particle properties. *Physical Review*, D45:II.20–II.21, 1992.

[19] The CDF Collaboration. A Measurment of the W Mass in $p\bar{p}$ Collisions at 1.8 TeV. *Physical Review*, D42, 1990.

[20] K. Yasuoka et al. Response Maps of the CDF Central Electromagnetic Calorimeter with Electrons. *Nuclear Instruments and Methods*, A267:315–329, 1988.

[21] W. Trischuk. *A Measurement of the W Boson Mass in 1.8 TeV Proton–Antiproton Collisions.* PhD thesis, Harvard University, 1990.

[22] Y. Fukui et al. CDF End Plug Electromagnetic Calorimeter Using Conductive Plastic Proportional Tubes. *Nuclear Instruments and Methods*, A267:280–300, 1988.

[23] G. Brandenburg et al. An Electromagnetic Calorimeter for the Small Angle Regions of the Collider Detector at fermilab. *Nuclear Instruments and Methods*, A267:257–271, 1988.

[24] S. Cihangir et al. The CDF Forward / Backward Hadron Calorimeter. *Nuclear Instruments and Methods*, A267:249–256, 1988.

[25] H. Frisch et al. Beam-Beam Counters for CDF. CDF Note # 250, June 1987.

[26] D. Amidei et al. A Two Level Fastbus Based Trigger System for CDF. *Nuclear Instruments and Methods*, A269:51–62, 1988.

[27] T. Carrol et al. The CDF Level 3 Trigger. *Nuclear Instruments and Methods*, A300, 1991.

[28] L. Nakae. *Direct Photon Center-of-Mass Angular Distributions in Proton–Anti-Proton Collisions at* $\sqrt{s} = 1.8$ *TeV.* PhD thesis, Brandeis University, 1992.

[29] L. Keeble. *A Study of Four Jet Events and Search for Double Parton Scattering with the Collider Detector at Fermilab.* PhD thesis, Texas A& M University, December 1992.

[30] F. Paige and S. Protopopescu. Isajet Monte Carlo Version 6.21. Technical Report BNL 38034, Brookhaven National Laboratory, 1986.

[31] D. Brown. *A Search for Double Parton Scattering in Proton-Antiproton Collisions at 1.8 TeV.* PhD thesis, Harvard University, 1989. A description of the tuning of the ISAJET fragmentation is given in Appendix B.

[32] W. Cheney and D. Kincaid. *Numerical Methods and Computing.* Brooks / Cole Publishing Co., second edition, 1985.

[33] The CDF Collaboration. Measurement of the Antiproton-Proton Total Cross Section at $\sqrt{s} = 546$ GeV and 1800 GeV. Submitted to Physical Review D, July 1993.

[34] F. Abe et al. A Measurement of the Production and Muonic Decay Rate of W and Z Bosons in $p\bar{p}$ Collisions at $\sqrt{s} = 1.8$ TeV. *Physical Review Letters*, 69:28–32.

[35] P. Arnold and M. Reno. The Complete Calculation of High p_t W and Z Production in Second Order QCD. *Nuclear Physics*, B319:37–72, 1989.

[36] The Bottom Quark Cross Section in $p\bar{p}$ Collisions from Inclusive Decays to Muons. In *Proceedings of Particles And Fields 92*, 1992.

[37] J. Krider. Single Wire Drift Chamber Design. Technical Report FNAL TM-1455, Fermi National Accelerator Laboratory, 1987.

[38] W.T. Eadie et al. *Statistical Methods in Experimental Physics.* North-Holland/American Elsevier, 1971.